Universität Stuttgart

Institut für Straßen- und Verkehrswesen
Lehrstuhl für Straßenplanung und Straßenbau
Univ.-Prof. Dr.-Ing. W. Ressel

Simulation of Pavement Surface Runoff using the Depth-Averaged Shallow Water Equations

Anne Wolff

ISSN 0932 - 402X
ISBN 978 - 3 - 9810573 - 4 - 8
D 93 (Dissertation der Universität Stuttgart)

Veröffentlichungen aus dem
Institut für Straßen- und Verkehrswesen

Heft 45 (März 2013)

Universität Stuttgart

Institut für Straßen- und Verkehrswesen
Lehrstuhl für Straßenplanung und Straßenbau
Univ.-Prof. Dr.-Ing. W. Ressel

Simulation of Pavement Surface Runoff using the Depth-Averaged Shallow Water Equations

Anne Wolff

Veröffentlichungen aus dem
Institut für Straßen- und Verkehrswesen

Heft 45 (März 2013)

Herausgeber : Institut für Straßen- und Verkehrswesen
Universität Stuttgart

Eigenverlag und Vertrieb : Institut für Straßen- und Verkehrswesen
Universität Stuttgart

Lehrstuhl für Straßenplanung und Straßenbau
Pfaffenwaldring 7
70569 Stuttgart

Simulation of Pavement Surface Runoff using the Depth-Averaged Shallow Water Equations

Von der Fakultät Bau- und Umweltingenieurwissenschaften der Universität Stuttgart
zur Erlangung der Würde eines Doktors der
Ingenieurwissenschaften (Dr.-Ing.) genehmigte Abhandlung

Vorgelegt von

Anne Wolff

aus Ludwigsburg

Hauptberichter:	Univ.-Prof. Dr.-Ing. Wolfram Ressel
Mitberichter:	Univ.-Prof. Dr.-Ing. Rainer Helmig
Tag der mündlichen Prüfung:	10.08.2012

Institut für Straßen- und Verkehrswesen der Universität Stuttgart

2012

Vorwort

Die vorliegende Arbeit entstand während meiner Tätigkeit als wissenschaftliche Mitarbeiterin am Lehrstuhl für Straßenplanung und Straßenbau der Universität Stuttgart.

Die Anregung dazu verdanke ich meinem Doktorvater Prof. Wolfram Ressel, der mir ermöglicht hat das Thema in freier Forschung zu bearbeiten. Mein Dank gilt auch Prof. Rainer Helmig für die Übernahme des Mitberichts, die fruchtbaren Gespräche in der Anfangsphase und die Möglichkeit, die vorhandene Softwarestruktur am Lehrstuhl für Hydromechanik und Hydrosystemmodellierung zu nutzen.

Meine Zeit am Lehrstuhl war von einer positiven Arbeitsatmosphäre geprägt. Zahlreiche Diskussionen, Anregungen und das freundschaftliche Miteinander haben mich immer wieder beflügelt. Dafür danke ich allen Kolleginnen und Kollegen.

Abschließend möchte ich mich bei meiner Familie und ganz besonders bei meinem Mann Markus für die vielfältige Unterstützung bedanken.

Stuttgart, im August 2012 Anne Wolff

Contents

List of Figures III

List of Tables VII

Notation IX

Zusammenfassung 1

Abstract 9

1. Introduction 1

2. Characterisation of Pavement Surface Runoff 7
2.1. Factors of Influence 7
2.1.1. Precipitation 7
2.1.2. Wind 10
2.1.3. Roadway Geometry 10
2.1.4. Surface Texture 14
2.2. Hydraulic Characterisation 17
2.2.1. Fluid Properties 17
2.2.2. Flow Properties 18
2.3. Summary and Conclusions for Model Development 21

3. The Shallow Water Equations 23
3.1. Derivation 23
3.1.1. Reynolds Transport Theorem 24
3.1.2. Navier-Stokes-Equations 26
3.1.3. Incompressible Euler Equations 28
3.1.4. Shallow Water Equations 28
3.2. Source Terms 33
3.2.1. Rainfall 33
3.2.2. Topography 34
3.2.3. Flow Resistance 34
3.3. Mathematical Characterisation 40
3.3.1. Hyperbolic Partial Differential Equations 40

3.3.2. Riemann Problem 42

4. Discretisation **47**
4.1. Finite Volume Discretisation 47
4.2. Flux Approximation 49
4.2.1. Approximate Riemann Solvers 51
4.2.2. Test Example 56
4.3. Source Term Discretisation 59
4.3.1. Topography 59
4.3.2. Flow Resistance 62

5. Pavement Surface Runoff Model **67**
5.1. Import of Topographic Data 67
5.1.1. Boundary Tracing 68
5.1.2. Interpolation 73
5.2. Flow Resistance 75
5.2.1. Experimental Setup 76
5.2.2. Estimation of the Resistance Coefficient 78
5.2.3. Data Analysis and Results 85
5.2.4. Extended Model Equations 90
5.3. Drainage Model 90

6. Model Application **97**
6.1. Comparison with Planus 97
6.2. Drainage 105
6.3. Analysis of an Existing Road Section 110
6.4. Analysis of a Designed Road Section 114

7. Final Remarks **117**
7.1. Summary 117
7.2. Topics of Future Research 120

Bibliography **123**

A. Appendix **133**
A.1. Jacobian Matrix of the Two Parameter Resistance Model 133
A.2. Histograms 135

List of Figures

1.1. Stages of model development. 5

2.1. Time-dependent profile of pavement surface runoff. 8
2.2. Superelevation transition sketched in three dimensions. 12
2.3. Clothoide linking two curves with constant radius. 12
2.4. Flow paths in a road section with constant cross slope (left) and in a superelevation transition (right), both with constant longitudinal slope. 13
2.5. Courses of the left and right shoulder within a superelevation transition between cross slopes $q_{\mathrm{p},1}$ and $q_{\mathrm{p},2}$. 13
2.6. Mean texture depth k determined with the sand patch method. . . . 16
2.7. Determination of mean profile depth from profile analysis. 16
2.8. Information propagation in subcritical, critical and supercritical flow. 19
2.9. Flow over an airfoil [32]. 20

3.1. Position of a control volume V_{CV} and system V_{sys} at times t and $t + \Delta t$. 25
3.2. Variables used in the Shallow Water Equations. 29
3.3. Velocity profile for turbulent flow. 36
3.4. Position of the discontinuity of a Riemann Problem for a linear, scalar equation at times t_0 and t_1. 42
3.5. Wave structure of the Riemann Problem for linear PDEs. 43
3.6. Characteristics of a concave and convex flux. 44
3.7. Initial value problem and characteristic curves of a rarefaction wave for convex flux. 44
3.8. Initial value problem and characteristic curves of a shock wave for convex flux. 45

4.1. Cell-centred finite volume discretisation on a cartesian grid. 48
4.2. Discontinuities at the cell interfaces due to volume averaging. 49
4.3. Riemann Problems forming at the cell interfaces. 50
4.4. Wave Structure assumed for the HLL solver within a control volume $[x_L, x_R]$. 52
4.5. Wave Structure assumed in the HLLC solver. 55
4.6. Time dependent water level calculated with the HLL solver. 57
4.7. Time dependent water level calculated with the HLLC solver. 58

4.8. Determination of water depth at the interface when using the divergence term formulation. 60
4.9. Determination of water depth at the interface when using the divergence term formulation in combination with very small water depths. 61
4.10. Water level profiles for various boundary conditions at the steady state: comparison of analytical and numerical solution. 62
4.11. Discharge at the outflow boundary of an inclined slab over time using the Manning's resistance equation: comparison of analytical and numerical solution. 64

5.1. Main and sub domain of a grid defined by a point cloud. 68
5.2. Convex hull and true boundary of a point cloud. 69
5.3. Concept of the graham scan algorithm to determine the convex hull of a point cloud. 69
5.4. Preliminary and final result of a segmented graham scan. 71
5.5. Boundary points determined by a segmented graham scan with variable segment widths Δx [m]. 72
5.6. Schematic view of the test station used in [95]. 77
5.7. Definition of averaged and referenced water depth and model concept for flow resistance. 78
5.8. Comparison of real and logarithmic velocity profile for a flow over large scale roughness according to [34] (not to scale). 80
5.9. Flow regions defined in [72] depending on inundation ratio λ. 81
5.10. Darcy-Weisbach resistance coefficient f plotted against inundation ratio λ for the five investigated surface covers. 83
5.11. Darcy-Weisbach resistance coefficient f plotted against the texture related Froude Number Fr_k for the five investigated surface covers. . . 85
5.12. Darcy-Weisbach resistance coefficient f plotted against the texture related Froude Number Fr_k for the five investigated surface covers and variable bottom slopes. 86
5.13. Logarithmus of the Darcy-Weisbach resistance coefficient $ln(f)$ plotted against $ln(Fr_k)$ for the investigated surface covers. 87
5.14. Comparison of the non-logarithmic and logarithmic fit for the Darcy-Weisbach resistance coefficient. 88
5.15. Water depth at a brink depending on upstream flow conditions. 91
5.16. Relation of water depth, discharge and energy. 93
5.17. Comparison of water depths near a brink for sub and supercritical flow conditions calculated with the Pavement Surface Runoff Model. 94

6.1. Superelevation transition used for the comparison of the Pavement Surface Runoff Model and Planus. 99
6.2. Comparison of water depth distribution for surface cover CJ. 100

6.3. Comparison of water depth distribution for surface cover CAT 100
6.4. Comparison of water depth distribution for surface cover SMA08 . . 100
6.5. Comparison of water depth distribution for surface cover SMA011. . . 101
6.6. Comparison of water depth distribution for surface cover DGA. 101
6.7. Water depth distribution for surface cover DGA including qualitatively determined flow paths and flow directions. 101
6.8. Water depth distribution of a basic superelevation transition with s = 0 %. 102
6.9. Histogram of water depths in the example superelevation transition for SMA011 and s = 0 %). 103
6.10. Histogram of water depths in the example superelevation transition for SMA011 and s = 2 %). 104
6.11. Histogram of water depths in the example superelevation transition for SMA011 and s = 4 %). 104
6.12. Sketch of the modelled road section. 106
6.13. Channel geometries near the curb. 107
6.14. Two dimensional water depth distribution for the modelled road section with a_d = 39 m calculated with the Pavement Surface Runoff Model. 107
6.15. Width of water level for a drainage spacing of 135 m and variable channel widths. 109
6.16. Aerial picture of the example road section [71]. 111
6.17. Vertical alignment (top) and superelevation design (bottom) of the example road section. 112
6.18. Comparison of the water depth distribution of the example road section for the parametrised and real topography calculated with the Pavement Surface Runoff Model. 113
6.19. Water depth distribution in the transition zone for the real topography calculated with the Pavement Surface Runoff Model. 114
6.20. Elevation contour lines determined in CAD and with the Pavement Surface Runoff Model for the example intersection. 115
6.21. Drainage paths and water depth distribution for the example intersection. 116

A.1. Histogram of water depths in the example superelevation transition for CJ and s = 0 %) 135
A.2. Histogram of water depths in the example superelevation transition for CJ and s = 2 %) 135
A.3. Histogram of water depths in the example superelevation transition for CJ and s = 4 %) 136
A.4. Histogram of water depths in the example superelevation transition for CAT and s = 0 %) 136

A.5. Histogram of water depths in the example superelevation transition for CAT and s = 2 %) 137
A.6. Histogram of water depths in the example superelevation transition for CAT and s = 4 %) 137
A.7. Histogram of water depths in the example superelevation transition for SMA08 and s = 0 %) 138
A.8. Histogram of water depths in the example superelevation transition for SMA08 and s = 2 %) 138
A.9. Histogram of water depths in the example superelevation transition for SMA08 and s = 4 %) 139
A.10. Histogram of water depths in the example superelevation transition for DGA and s = 0 %) 139
A.11. Histogram of water depths in the example superelevation transition for DGA and s = 2 %) 140
A.12. Histogram of water depths in the example superelevation transition for DGA and s = 4 %) 140

List of Tables

2.1. Classification of rain events depending on rainfall intensity according to [5, 69] and [79]. 10
2.2. Design categories for motorways in Germany [41]. 11
2.3. Surface covers on German Federal Highways in percent (BASt). . . . 15

5.1. Coefficients of determination for the one and two parameter models. 89
5.2. Coefficients of determination for the one and two parameter models calculated with the logarithmic transformation. 89

6.1. Maximum averaged water depths h and referenced water depths h_{ref} for the basic superelevation transition with s = -2 % and variable surface covers. 99
6.2. Water level widths calculated according to [40] and with the Pavement Surface Runoff Model for a simple channel. 108
6.3. Water level widths calculated according to [40] and with Pavement Surface Runoff Model for an inclined channel with $b_c = b_w$. 108

Notation

The following table shows the symbols used in this work. Local notations are explained in the text.

Symbol	Definition	Dimension
Greek Letters:		
ε	drainage efficiency of an inlet	[-]
η	water level	[m]
$\varphi_{\text{boundary}}$	angle of two sections of a boundary polygon	[°]
κ	curvature	[-]
λ	inundation ratio	[-]
λ_{t}	wave length of the surface texture	[mm]
λ_{w}	characteristic wave speed	[m/s]
μ	dynamic fluid viscosity	[kg/(m s)]
ν	fluid viscosity	[m^2/s]
ρ	fluid density	[kg/m^3]
τ	shear stress	[kg /(m s^2)]
Latin Letters:		
a	distance of the highway shoulder to the axis of rotation	[m]
b	pavement width	[m]
b_{w}	water level width	[m]
b_{c}	channel width	[m]
C	Chézy resistance coefficient	[-]
E	energy head	[m]
f	Darcy Weisbach resistance coefficient	[-]
Fr	Froude Number	[-]
Fr_k	roughness related Froude Number	[-]

g	gravity constant	[m/s^2]
$\mathcal{G}$	dimensionless gravity	[-]
h	water depth	[m]
h_c	critical water depth	[m]
h_ref	referenced water depth	[m]
$\mathcal{H}$	dimensionless water depth	[-]
i	rainfall intensity	[mm/min]
$\mathbf{J}$	Jacobian Matrix	
k	mean texture depth of the pavement surface	[mm]
k_char	characteristic length scale of surface roughness	[mm]
k_s	equivalent sand grain roughness	[-]
L_V	length of superelevation transition	[m]
L_V	length of the central part of a superelevation transition	[m]
n	Manning resistance coefficient	[-]
q_p	cross slope of the pavement	[%]
q_r	source term representing rainfall in the continuity equation	[%]
q, r	discharges in x and y direction	[m^3/s]
r_h	hydraulic radius	[m]
R	curve radius	[m]
Re	Reynolds Number	[-]
Re^*	grain Reynolds Number	[-]
s	longitudinal slope	[%]
Δs	relative gradient	[%]
S_0	bottom slope in the SWE	[-]
S_f	friction slope in the SWE	[-]
$S_\mathrm{L}, S_\mathrm{R}$	signal velocities in the HLL solver	[m/s]
u, v, w	velocities in x, y and z direction	[m/s]
$\mathcal{V}$	dimensionless velocity	[-]
$\mathcal{X}$	dimensionless distance	[-]
z_b	bottom elevation	[m]
$\mathcal{Z}_\mathrm{b}$	dimensionless bottom elevation	[-]

Abbreviations:

CJ	Concrete with jute fibre texture
CAT	Concrete with artificial turf texture
CV	Control Volume
DGA	Dense graded asphalt

DUMU^x	DUNE for Multi-{Phase, Component, Scale,Physics, ...} Flow and Transport in Porous Media
DUNE	Distributed and Unified Numerics Environment
EKA	Design class for freeways according to the German highway design guidelines
EKL	Design class for rural highways according to the German highway design guidelines
FD	Finite Differences
FE	Finite Elements
FV	Finite Volumes
HLL	Approximate Riemann Solver developed from Harten, Lax and van Leer
HLLC	HLL solver which considers contact waves
PSRM	Pavement Surface Runoff Model
RAA	German guidelines for the design of motorways
RAL	German guidelines for rural highway design
SMA08	Stone matrix asphalt with 8 mm max. grain size
SMA11	Stone matrix asphalt with 11 mm max. grain size
SWE	Shallow Water Equations

Zusammenfassung

Zielsetzung

Große Wassermengen auf der Fahrbahn, verursacht durch abflussschwache Zonen, sind ein hohes Sicherheitsrisiko für den Straßenverkehr. Weiterhin beeinflussen sie die Dauerhaftigkeit des Straßenoberbaus, der durch eindringendes Wasser in Verbindung mit Frost-Tau-Wechseln strukturell stark geschädigt werden kann. Um bestehende und geplante Straßenabschnitte hinsichtlich ihrer Entwässerungseigenschaften zu überprüfen und planerische Verbesserungsmöglichkeiten aufzuzeigen, wird in dieser Arbeit ein Modell entwickelt, das den Wasserabfluss auf Fahrbahnoberflächen ganzheitlich beschreibt. Dies beinhaltet die zeitabhängige Simulation des Abflusses auf realen Fahrbahnoberflächen mit irregulärer Topographie (Unebenheiten) unter Betrachtung unterschiedlicher Fahrbahnbeläge sowie offener und geschlossener Fahrbahnränder, einschließlich der Entwässerungseinrichtungen. Die Implementierung des Modells erfolgt in den Open Source Umgebungen DuMu^x [43] bzw. DUNE [104] in der Programmiersprache C++.

Modellansätze

Existierende Modelle zur Beschreibung des Fahrbahnoberflächenwasserabflusses sind meist empirisch und bilden lediglich den stationären Gleichgewichtszustand ab [46, 56, 59, 64, 90, 91, 97]. Das Fließverhalten wird eindimensional entlang der Falllinien beschrieben, die sich aus der Geometrie der Fahrbahn (Lage im Raum) und der Topographie der Fahrbahnoberfläche ergeben. Die Fließgleichung ist eine mathematische Funktion, in der für den Abfluss relevante Variablen multiplikativ verknüpft und mit experimentell gewonnenen Regressionskoeffizienten kalibriert werden. Der Vorteil solcher Modelle ist, dass die Anzahl der Variablen im Modell frei wählbar ist, sofern sie aus den Experimenten erhoben werden können. Nachteilig ist, dass empirische Modelle ein sehr begrenztes Anwendungsspektrum bieten und nachträglich nicht erweiterbar sind, da sie direkt an die Versuchsbedingungen und -ergebnisse gekoppelt sind. Desweiteren werden zweidimensionale und zeitabhängige Effekte vernachlässigt.

Um die oben gestellten Anforderungen an ein ganzheitliches Modell zu erfüllen, empfiehlt sich der Einsatz eines hydrodynamischen Modells. Hydrodynamische

Modelle basieren auf den kontinuumsmechanischen Erhaltungsgleichungen für Masse und Impuls. Gravitationsdominierte Strömungen mit freier Oberfläche werden von den zweidimensionalen, tiefengemittelten Flachwassergleichungen, auch bekannt als Saint Venant Gleichungen, beschrieben. Diese lassen sich direkt aus den inkompressiblen Navier-Stokes-Gleichungen ableiten unter folgenden Annahmen:

- vernachlässigbar kleine Viskosität,
- hydrostatische Druckverhältnisse und
- vernachlässigbare Geschwindigkeit und Geschwindigkeitsvariationen in vertikaler Richtung (tiefengemittelte Geschwindigkeiten).

Bisher existiert kein Modell zur Simulation des Fahrbahnoberflächenwasserabflusses auf Basis der tiefengemittelten Flachwassergleichungen. Bestehende hydrodynamische Ansätze gehen von einer vereinfachten Impulsgleichung aus (kinematische und diffusive Welle-Gleichungen) [25, 68]. Ein Grund dafür ist, dass die Effekte, die mit der vollständigen Impulsgleichung beschrieben werden, als nicht relevant erachtet werden. Weitere Gründe, die einen solchen Ansatz bisher verhindert haben, sind neben der aufwändigeren Implementierung der hohe Rechenaufwand und das Auftreten numerischer Instabilitäten in Verbindung mit sehr kleinen Wassertiefen. Die Entwicklung neuer Diskretisierungsmethoden für die Flachwassergleichungen, besonders im Bereich der Quelltermdiskretisierung ist immer noch Gegenstand vieler Forschungsarbeiten. Zudem steigt die Rechnerkapazität weiter an. Darum wird in dieser Arbeit ein Modell entwickelt, das auf der vollständigen Impulsgleichung beruht.

Fahrbahnoberflächenabfluss und mathematisches Modell

Beeinflusst wird das Abflussverhalten maßgeblich durch die Regenintensität, die Fahrbahngeometrie und -topographie sowie die Textur der Fahrbahnoberfläche. Diese Faktoren sind im Modell zu berücksichtigen. Weitere Einflussfaktoren wie Wind und Regentropfenaufschlag besitzen zwar einen gewissen Einfluss, werden aber in dieser Arbeit vernachlässigt. Diese Variablen werden für eine grundsätzliche Beschreibung des Abflussverhaltens nicht benötigt.

Hydraulisch ist das Abflussverhalten als schwach ungleichförmig einzustufen. Versuchsergebnisse aus anderen Arbeiten zeigen, dass der Fahrbahnoberflächenabfluss prinzipiell laminare bis voll turbulente Strömungsverhältnisse annehmen kann [95, 25]. Letztere treten aber nur bei unüblich starken Regenintensitäten auf, so dass Strömungszustände im laminaren Bereich und im Übergangsbereich vorherrschend sind. Aus diesem Grund wird auf die Implementierung eines Turbulenzmodells verzichtet.

Der Fahrbahnoberflächenabfluss ist ein zeitabhängiger Prozess, wobei im stationären Zustand die größten Wasserfilmdicken auftreten. Bei der Simulation irregulärer Topographien kann im stationären Zustand eine Überschätzung der Wasserfilmdicken eintreten, da die vollständige Füllung von Unebenheiten bei Regenereignissen kürzerer Dauer nicht zwingend eintreten muss. Aus diesem Grund ist eine zeitabhäangige Simulation sinnvoll.

Fahrbahnen sind sowohl längs als auch quer geneigt. In Bereichen, in denen die Sohlneigungen variabel sind, zum Beispiel in Verwindungsbereichen oder auf unebenen Fahrbahnoberflächen, ist das Abflussverhalten eindeutig zweidimensional. Zudem wird der Abfluss einzig durch die Sohlneigungen angetrieben. Er ist somit gravitationsdominiert. Ein weiteres Merkmal sind die sehr kleinen Wassertiefen des Fahrbahnoberflächenabflusses im Verhältnis zu den horizontalen Ausdehnungen der Fahrbahn. Vor allem im Bereich der Autobahnen sind die Sohlneigungen relativ gering. In Verbindung mit den sehr kleinen Wassertiefen ist somit die Annahme hydrostatischer Verhältnisse und folglich die Verwendung der tiefengemittelten Flachwassergleichungen gerechtfertigt.

Das mathematische Modell zur Simulation des Fahrbahnoberflächenabflusses setzt sich schließlich zusammen aus den tiefengemittelten Flachwassergleichungen, bestehend aus der Kontinuitätsgleichung und zwei Impulsgleichungen, ergänzt um Quellterme zur Beschreibung des Regeneintrages in der Kontinuitätsgleichung und des Fließwiderstands in der Impulsgleichung.

Diskretisierung

Die Lösung der Modellgleichung erfolgt mit einem zell-zentrierten Finite-Volumen-Verfahren auf einem kartesischen Gitter. Zwei Aspekte sind bei der Diskretisierung von besonderer Bedeutung: die Flussapproximierung und die Zeitdiskretisierung des Quellterms zur Beschreibung des Fließwiderstands.

Die tiefengemittelten Flachwassergleichungen bilden ein System nicht-linearer, hyperbolischer Differentialgleichungen, die auch diskontinuierliche Lösungen zulassen. Physikalisch entspricht dies der Beschreibung von Wellenbewegungen, die sich im diskontinuierlichen Fall als Schockwellen darstellen. Wichtig ist, dass diese Eigenschaften bei der Lösung der diskreten Gleichungen erhalten bleiben. Verfahren, die diese Eigenschaften bei der Flussapproximation berücksichtigen, basieren auf der Lösung des Riemann-Problems an der Zellkante. Da die genaue Lösung des Riemann-Problems sehr aufwändig und für nicht-lineare Systeme nur iterativ möglich ist, kommen meist approximative Riemann-Löser in Verbindung mit den Flachwassergleichungen zum Einsatz. Die approximativen Riemann-Löser unterscheiden sich in ihrem Detailgrad, wobei komplexere Löser wie der Löser von Roe Schockfronten sehr gut erhalten und daher genau abbilden. Bei einfacheren

Lösern, wie dem HLLC- oder HLL-Löser werden die Schockfronten dagegen etwas verschmiert. Bei der Simulation des Fahrbahnoberflächenabflusses ist die detailgenaue Abbildung von Schockfronten von untergeordneter Bedeutung, im Gegensatz zu Simulationen, die sich mit Dammbruch- oder Tsunamiwellen beschäftigen. Da die Gegenüberstellung der beiden einfachsten Löser in einem Testbeispiel keine signifikanten Unterschiede zeigt, wird der HLL Löser als Standardlöser implementiert.

Der Quellterm zur Beschreibung des Fließwiderstandes kann bei sehr kleinen Wassertiefen numerische Instabilitäten provozieren. Zur Vermeidung dieser Instabilitäten wird der Term oft semi-implizit oder sogar vollständig implizit diskretisiert. In dieser Arbeit wird ein vollständig impliziter Ansatz verfolgt. Mit Hilfe eines Operator-Splitting-Verfahrens werden die Flachwassergleichungen in einen explizit und einen implizit zu lösenden Teil getrennt. Der implizite Teil besteht lediglich aus dem Quellterm zur Beschreibung des Fließwiderstandes. Je Zeitschritt wird zuerst der explizite Teil gelöst und dann der dort bestimmte Zeitschritt für die Lösung des impliziten Teils verwendet. Als Anfangsbedingung geht die Lösung des expliziten Teils mit ein. Mit diesem Verfahren bleibt das Modell auch bei sehr kleinen Wassertiefen numerisch stabil.

Modellanpassung

Das bisher beschriebene Modell bildet das Grundgerüst zur Simulation des Fahrbahnoberflächenabflusses. Um jedoch reale Fallbeispiele rechnen zu können, müssen einige Anpassungen und Erweiterungen vorgenommen werden. Diese beinhalten die Entwicklung einer Routine für den Import und die Verarbeitung topographischer Daten, die Entwicklung eines Fließwiderstandsmodells in Abhängigkeit unterschiedlicher Fahrbahntexturen sowie die Entwicklung einer Methode zur Modellierung von Entwässerungseinrichtungen.

Topographie Die Geometrie von Fahrbahnoberflächen ist im Entwurf durch mathematische Funktionen beschreibbar. Diese können in das Modell integriert werden, um die Sohlhöhen im Modellbereich zu berechnen. Komplexe Geometrien, wie zum Beispiel Knotenpunkte oder bestehende Fahrbahnoberflächen, die zusätzlich zur Geometrie auch eine Fahrbahntopographie besitzen, sind nicht analytisch exakt zu beschreiben. Um für diese Fälle Höhendaten zu generieren, müssen topographische Daten, entweder aus einem Entwurfsprogramm oder einer Laserscanmessung in das Modell importiert und auf das Simulationsgitter interpoliert werden.

Die hier entwickelte Routine zum Import und zur Verarbeitung topographischer Daten besteht aus zwei Teilen: der Bestimmung des Randpolygons der Punktwolke und der Interpolation der Höhendaten auf das Simulationsgitter.

Für die Bestimmung des Randpolygons einer Punktwolke existieren in der algorithmischen Geometrie zahlreiche Methoden. Sie basieren auf der Theorie der konvexen Hülle. Problematisch ist jedoch, dass Punktwolken, die eine Fahrbahngeometrie abbilden, nicht rein konvex sind, sondern sowohl konvexe als auch konkave Anteile besitzen. Um auch für diesen Fall ein Randpolygon automatisch bestimmen zu können, wird ein bestehendes Verfahren zur Bestimmung der konvexen Hülle angepasst [50]. Dabei wird die Punktwolke in eine definierte Anzahl von Teilpunktwolken zerlegt und die konvexe Hülle für jede Teilpunktwolke bestimmt. Anschließend werden die Teilpunktwolken zusammengeführt und die nun innen liegenden Randpunkte eliminiert. Je kleiner die Teilgebiete gewählt werden, desto besser können konvexe Bereiche erkannt werden. Nachteil des Verfahrens ist, dass es nur relativ schwach konvexe Ränder auflösen kann. Der minimale konkave Winkel zwischen zwei Polygonabschnitten beträgt 120°. Für Straßen außerorts, die mit großen Radien trassiert sind, wird diese Grenze nicht erreicht. Bei stark konvexen Geometrien, wie zum Beispiel Knotenpunkten oder Straßen innerorts, muss das Randpolygon vorher bestimmt und in das Modell importiert werden.

Die Interpolation der topographischen Daten erfolgt mit dem Inverse-Distance-Weighting-Verfahren. Die Höhe des gesuchten Punktes wird aus den Höhen der Nachbarpunkte ermittelt. Die Höhen der Nachbarpunkte werden dabei invers mit deren Distanz zum gesuchten Punkt gewichtet. Im Gegensatz zu Verfahren, die auf einer Triangulierung der Punkte und einer nachfolgenden Interpolation beruhen, müssen die Daten für eine zuverlässige Anwendung dieses Verfahrens gleichmäßig verteilt und relativ dicht sein. Für Punktwolken aus Laserscanmessungen und Entwurfsprogrammen ist diese Voraussetzung erfüllt. Eine Interpolation aus Höhenlinien ist dagegen nicht möglich.

Fließwiderstand Der Fließwiderstand wird maßgeblich von der Textur der Fahrbahnoberfläche beeinflusst. Um das Abflussverhalten auf unterschiedlichen Fahrbahnoberflächen simulieren zu können, wird in dieser Arbeit ein Fließwiderstandsmodell in Abhängigkeit der mittleren Texturtiefe eines Fahrbahnbelags entwickelt. Der Fahrbahnoberflächenabfluss ist eine Strömung über eine sehr raue Oberfläche, da die Wassertiefen und Texturtiefen die gleiche Skala besitzen. Zur möglichst genauen Abschätzung des Fließwiderstands müsste der dreidimensionale Strömungszustand um die Textur auf der Mikroskala aufgelöst werden. Für Anwendungen der Flachwassergleichung, bei denen die horizontalen Ausdehnungen des Modellgebietes jedoch um ein vielfaches größer sind als die vertikalen, ist ein derartiger Ansatz zu rechenintensiv. Aus diesem Grund wird auf empirische Widerstandsgesetze zurückgegriffen.

Der Fließwiderstand in den Flachwassergleichungen wird üblicherweise mit einem der beiden empirischen Widerstandsgesetze nach Manning oder Darcy-Weisbach

beschrieben. Letzteres wird in dieser Arbeit verwendet. Aufgabe ist es, den Fließwiderstandsbeiwert in Abhängigkeit der mittleren Texturtiefe zu bestimmen. Grundlage dafür bilden Versuchsergebnisse aus [95]. Darin wurden eindimensionale Abflussversuche auf fünf verschiedenen Fahrbahnbelägen durchgeführt. Mit Hilfe einer Dimensionsanalyse, die die mittlere Texturtiefe als charakteristische Länge enthält, kann eine Variable abgeleitet werden, die den Widerstandsbeiwert signifikant beeinflusst: die texturbezogene Froude-Zahl. Weiterhin wird die Sohlneigung als Regressionsvariable verwendet. Es kann gezeigt werden, dass die multiplikative Verknüpfung beider Variablen mit entsprechenden Regressionskoeffizienten die beste Anpassung an die Versuchergebnisse liefert. Das Bestimmtheitsmaß liegt für die verschiedenen Beläge zwischen 0,88 und 0,99. Mit der Aufstellung einer Gleichung für den Widerstandsbeiwert, die die mittlere Texturtiefe als Variable enthält, ist es zukünftig möglich, auch Beläge mit anderen Texturtiefen zu simulieren.

Entwässerungseinrichtungen Entwässerungseinrichtungen an Straßen können linienförmig (Rinnen) oder punktförmig (Einläufe) sein. Vereinfacht wird die Kante der Entwässerungseinrichtungen als hydraulisch vollkommener Überfall beschrieben. Diese Annahme impliziert, dass keinerlei Interaktionen zwischen den Bereichen oberstrom und unterstrom der Abflusskante stattfinden. Daher können mit diesem Ansatz keine Rückstaueffekte simuliert werden. Weiterhin wird angenommen, dass der gesamte Zufluss von den Entwässerungseinrichtungen aufgenommen werden kann und kein Wasser über die Schachtabdeckung hinweg schießt.

Bei einem vollkommenen Überfall bilden sich an der Abflusskante unterschiedliche Wassertiefen aus und zwar je nachdem, ob die Kante unter- oder überkritisch angeströmt wird. An der Kante selbst werden kritische Strömungsbedingungen angenommen. Diese Bedingung ermöglicht die Berechnung der Wassertiefe an der Kante und die Berechnung des Abflusses über die Kante. Der Abfluss wird als Neumannsche Randbedingung im Modell implementiert. Da die Abflusskanten im Modell stets mit Zellkanten übereinstimmen, wird im zweidimensionalen Modell nur der Abfluss orthogonal zur Zellkante berücksichtigt.

Modellanwendungen

Die Anwendung auf realitätsnahe Beispiele gibt abschließend einen Überblick über das Anwendungsspektrum des Modells und grenzt es gleichzeitig von bestehenden Modellen ab. Ferner kann auch die Plausibilität der Ergebnisse überprüft werden. Eine Validierung des Modells an realen Bedingungen ist bisher nicht möglich, da Wasserfilmdicken in situ nicht zu messen sind. Folgende Anwendungen werden in der Arbeit vorgestellt:

- Fahrbahn mit Hochbord und seitlich angeordneten Einläufen: dieses Beispiel demonstriert die Simulation des Abflusses in einer Rinne entlang geschlossener Ränder und die Implementierung der Neumannschen Randbedingung für die Entwässerungseinrichtungen. Zwei Rinnentypen werden untersucht, eine Bordrinne und eine Spitzrinne. Zur Bemessung der Entwässerungseinrichtungen entlang solcher Rinnen werden in den gültigen Richtlinien die gängigen eindimensionalen Ansätze zur Berechnung von Gerinneströmungen verwendet. Hier wird der seitliche Zufluss von der Fahrbahn in das Gerinne als volumetrischer Quellterm integriert. Der Vergleich beider Ansätze zeigt, dass vor allem bei Bordrinnen die zweidimensionalen Effekte, die der seitliche Zufluss von der Fahrbahn in das Gerinne auslöst, relevant sind. Ein weiterer Vorteil des zweidimensionalen Ansatzes ist die Möglichkeit, eine überlaufende Rinne zu simulieren.
- Fahrbahn mit irregulärer Topographie: dieses Beispiel demonstriert den Import und die Verarbeitung topographischer Daten, die aus einer Laserscanmessung gewonnen wurden. Es zeigt, dass das Modell in der Lage ist, das Randpolygon der Punktwolke problemlos zu erkennen und die Höhendaten auf das Simulationsgitter zu interpolieren. Der dargestellte Fahrbahnabschnitt weist außerdem in der Realität verschiedene Fahrbahnbeläge auf. Deren Einfluss auf die Wasserfilmdicke wird ebenfalls abgebildet.
- Knotenpunkt mit stark konvexen Rändern: dieses Beispiel demonstriert den Import und die Verarbeitung topographischer Daten aus einem Entwurfsprogramm. Hierbei wird das Randpolygon in das Modell importiert. Der Import topographischer Daten und die Möglichkeit komplexe Geometrien und Topographien darzustellen, bieten einen großen Vorteil. Im Gegensatz zu gängigen Entwurfsprogrammen, die eine Abflussanalyse gegenwärtig nur mit Hilfe von Falllinien erlauben, kann mit dem entwickelten Modell das zweidimensionale, zeitabhängige Abflussverhalten wiedergeben werden.

Neben den geschilderten Anwendungsbeispielen wird das Modell mit einem bestehenden, empirischen Modell [95] verglichen. Der Vergleich ist möglich, da beide Modelle mit der gleichen Datenbasis kalibriert wurden. Auf Grundlage der Wasserfilmdickenverteilung in einem Verwindungsbereich wird gezeigt, dass die örtliche Verteilung der Wasserfilmdicken und die jeweils maximale Wasserfilmdicke beider Modelle vergleichbar sind. Bei kleinen Sohlneigungen liefert das zweidimensionale Modell unter Berücksichtigung der vollständigen Impulsgleichung allerdings andere Ergebnisse. Die Vermutung, dass diese Effekte vernachlässigbar sind, kann dadurch nicht bestätigt werden.

Mit dem in dieser Arbeit entwickelten Modell steht erstmals ein Werkzeug zur Verfügung, das auf Basis der tiefengemittelten Flachwassergleichungen den Abfluss auf Fahrbahnoberflächen unter Berücksichtigung zahlreicher Randbedingungen

(Geometrie, Topographie, Textur, Ränder, Entwässerungseinrichtungen) beschreibt. Die Implementierung in einer Open-Source-Umgebung und der hydrodynamische Charakter ermöglichen es weiterhin, das Modell zu verfeinern und zu erweitern.

Ausblick

Eine Modellentwicklung ist stets mit dem Treffen von Annahmen und Vereinfachungen verbunden. Zukünftige Modellverfeinerungen und -erweiterungen sind unter anderem in folgenden Themenfeldern denkbar:

- Topographie: Die Interpolation topographischer Daten auf das Simulationsgitter mit dem Inverse-Distance-Weighting-Verfahren ist ausschließlich bei dicht und gleichmäßig verteilten Datensätzen möglich. Um auch ungleichmäßig verteilte Datensätze verarbeiten zu können, wäre ein Interpolationsverfahren hilfreich, das auf einer Delaunay-Triangulierung beruht. Wird eine Delaunay-Triangulierung implementiert, könnte auch der Algorithmus zur Bestimmung des Randpolygons verbessert werden. Ein Verfahren, das in der Lage ist, auch ausgeprägte konkave Strukturen zu erkennen und auf der Delaunay-Triangulierung beruht, ist das Alpha-Shape-Verfahren.

- Entwässerungseinrichtungen: im vorliegenden Modell wird angenommen, dass der gesamte Zufluss, der auf einen Einlauf zuströmt aufgenommen werden kann. Versuche, die verschiedene Schachtabdeckungen und Anströmungsbedingungen untersuchen, könnten hierzu verbesserte Aussagen liefern.

- Fließwiderstandsmodell: Nachteile des entwickelten Modells ergeben sich aus der relativ kleinen Datenbasis, die für die Kalibrierung verwendet wurde. Weitergehende Versuche sollten Geschwindigkeitsmessungen, sowie Zu- und Abflussmessungen beinhalten, um die Bedingung des gleichförmigen Abflusses überprüfen zu können. Daher wird die Durchführung weiterer Versuche empfohlen. Auf lange Sicht könnte der Fließwiderstand auch numerisch untersucht werden, in dem die Prozesse auf der Mikroskala aufgelöst werden.

- Offenporige Fahrbahnbeläge: Die Simulation der Wirkungsweise offenporiger Asphaltdeckschichten ist eine wichtige Erweiterung des Modells, da offenporige Beläge durch ihre lärm- und wasserabsorbierende Wirkung immer mehr an Bedeutung gewinnen. Die Implementierung könnte entweder durch einen Senkterm in der Kontinuitätsgleichung erfolgen oder durch die Kopplung des Oberflächenabflussmodells mit einem Modell zur Simulation der Durchströmung poröser Medien. In diesem Fall müsste die Annahme der hydrostatischen Druckbedingung aufgegeben und ein nicht-hydrostatisches Modell implementiert werden.

Abstract

Water on the pavement significantly affects traffic safety. Climate change will lead to a higher number of heavy rainstorms in Germany and the risk to have large amounts of water on the pavement will even increase. Therefore, it is important to have a tool which enables highway engineers to analyse existing and designed road sections concerning their drainage capability. In this work, a model is developed, which allows an integral simulation of pavement surface runoff. This includes features like the simulation on real pavement surfaces with an irregular topography, the possibility to treat different surface textures and the treatment of drainage facilities. As mathematical model, the depth-averaged Shallow Water Equations are chosen. The equations are extended with source terms to describe the influence of rainfall, bottom topography and flow resistance. A cell-centred finite volume method is used for spatial discretisation. The approximation of the intercell fluxes is done with the HLL approximate Riemann solver. For time discretisation, the momentum equations are splitted into an explicit and implicit part, where the implicit part solely consists of the flow resistance source term. By the implicit treatment, numerical instabilities in the case of small water depths can be avoided. For the simulation on pavement surfaces with irregular topography or complex boundary shapes, e.g. intersections, the model is extended by a routine to import and process topographic point data. It consists of an Inverse Distance Weighting Algorithm for the interpolation of point data and a modified Graham Scan algorithm for the detection of convex boundaries. To model the effect of the surface texture on flow resistance, an empirical equation for the Darcy-Weisbach resistance coefficient is developed on the basis of a texture related dimensionless parameter. Drainage facilities are modelled as free overfalls based on the theory of critical flow. So far, the use of the Shallow Water Equations was often rejected due to the high computational effort and the occurrence of numerical instabilities in the case of small water depths. Further, effects described by the full momentum equation were considered nonrelevant. However, this work shows that the Shallow Water Equations can provide a stable and flexible model for the simulation of pavement surface runoff. Based on the water depth distribution in a superelevation transition, it can also be demonstrated that especially in the presence of small bottom slopes, the consideration of momentum and horizontal pressure gradient influences the results.

1. Introduction

The road network is a lifeline of civilisation. Primarily, it is designed to provide maximum capacity. However, growing demands and the need for economic efficiency bring up additional requirements, which have to be considered in the design and construction process as well as in service. The most important are: durability, riding quality and especially traffic safety. Water on the pavement significantly influences these road characteristics. Therefore, a sufficient road drainage is indispensable to provide durable, comfortable and safe roads.

The durability of a pavement structure can be defined as the property to withstand the forces from traffic loading and to ensure sufficient bearing capacity and performance characteristics over the desired life cycle. A pavement structure within this context is defined as the sum of all unbound and bound pavement layers. A loss of bearing capacity typically results in the formation of cracks in the bound layers. Over time, they develop up to the pavement surface. Although the bound layers are designed impervious, unless a porous asphalt structure is assumed, water enters the structure. In combination with freeze and thaw cycles this can cause severe damages. The process is even enforced if the pavement surface is not even and water accumulates in pits instead of being drained off. Then, the impact time of the water on the structure increases. Unevenness of the pavement results from the thermo-viscoelastic behaviour of asphalt. High wheel loads in combination with shear forces induced by braking and accelerating generate deformations in longitudinal and transverse direction. Besides a decrease of drainage capability, unevenness also reduces the riding quality of the pavement surface.

Ponded water on uneven pavement surfaces is not only relevant in terms of durability. It also is a major concern with respect to traffic safety. In the presence of high water depths, splash and spray drastically decreases visibility. In combination with high vehicle speeds, hydroplaning additionally constitutes a serious safety risk. Hydroplaning occurs when the tire is not able to suppress the water from the contact area. As a result, a layer of water forms between tire and pavement what results in a loss of traction. Therefore, it prevents the vehicle from responding to any action like steering, braking or accelerating. Dangerous accumulations of water do, however, not only occur on uneven pavements. They are also generated when drainage facilities are overloaded and backwater effects occur. In some cases they are even generated systematically by special alignment configurations where bottom slopes

are small and water is drained off slowly. Such configurations are for example transition curves. In [95], an accident study for a six lane motorway with a dual carriageway revealed that the risk of a wetness-related accident in transition curves is about two times higher than in other road sections. If the pavement is dry, the accident risk is roughly the same.

In summary, it can be stated that water on the pavement significantly affects traffic safety. In addition, the road design as well as the pavement's topography influence the amount of water on the pavement. The climate change will lead to an increasing number of heavy rainstorms in Germany [80]. Consequently, the risk to have large amounts of water on the pavement will even increase. Highway engineers have to face this development by analysing existing road sections concerning their drainage capacity as well as by developing new design standards. This explains the need for a tool, which allows an integral simulation of pavement surface runoff. An integral simulation includes the possibility to simulate any type of boundaries, namely, open and closed curbs, the consideration of drainage facilities and various pavement surface textures as well as the simulation of water depth distributions on uneven pavement surfaces. The latter are further on referred to as pavements with irregular topography. Various models exist to simulate pavement surface runoff, which will be reviewed shortly in the following paragraphs. None of them, though, is able to cope with all of the mentioned aspects. Therefore, the clear objective of this work is to set up an integral model for the simulation of pavement surface runoff.

Research on pavement surface runoff roughly dates back to 1930 [91]. At that time, it was primarily motivated by the desire to improve the design of drainage facilities. Not until the 1960ies, the effect of road drainage on traffic safety was detected (e.g. [97]). This was due to growing road networks, wider roads and higher vehicle speeds. Studies were limited to one dimensional experiments. The aim was to investigate the correlation of slope and drainage path length on water depth. In the 1970ies, research on pavement surface runoff was firstly linked to the real roadway geometry to investigate the effect of the design parameters on water depth [59].

In general, pavement surface runoff models can be classified in two groups: empirical and hydrodynamic models. An extensive overview of various models is given in [90, 25, 95]. Hydrodynamically, pavement surface runoff is a free surface flow. The background for research on pavement surface runoff are therefore open-channel flow theory, sheet flow mechanics and overland flow modelling.

Empirical models assume a one-dimensional flow behaviour. They try to link significant flow parameters by empirical coefficients within a mathematical function, which mostly is of potential type. The coefficients are determined by fitting the equations to experimental data [56, 91, 97]. Most significant parameters with respect to pavement surface runoff are bottom slope, friction slope and discharge. An advantage of empirical models is that the set of considered parameters is arbitrary

as long as it is considered in the conception of the experiments. This allows to investigate additional influences, which for pavement surface runoff, can be raindrop impact or wind [59, 46, 64, 90]. In contrast, empirical models are very limited because they are restricted to the parameter set once defined and to the underlying experiments. Therefore, a later extension of an existing empirical model is hardly possible without performing a complete new set of experiments. This also explains the big variety of models which are difficult to compare to each other.

Hydrodynamic models describe the flow behaviour by equations developed from the basic laws of conservation, namely continuity as well as momentum equations. The equations to model free surface flow are derived from the Navier Stokes Equations and are often referred to as Saint Venant or Shallow Water Equations. They are commonly used in overland, river and ocean flow modelling [10, 12, 16, 37, 48, 109]. Several types of the Shallow Water Equations exist depending on the degree of simplification of the momentum equations. Besides the time dependent change of momentum, the full momentum equations consider the convective momentum flux, the pressure gradient and the source terms for bottom slope and friction slope. The equation considering the full momentum equation without further simplification is referred to as dynamic wave equation. If the convective part is neglected, one speaks of the diffusive wave equation. Finally, the kinematic wave equation exclusively considers bottom slope and friction slope. In the one dimensional case this equals the open-channel flow equation.

The one dimensional kinematic wave equation has been a common choice to model various topics in overland flow and sheet flow mechanics as described in [25]. In [68], the kinematic wave equation was applied to pavement surface runoff. Three reasons are commonly mentioned for the use of the simplest of the three equations. First, the equation is easy to implement. Second, effects described by the full momentum equation can be neglected. Third, a one dimensional steady state simulation seems sufficient to simulate pavement surface runoff. When looking at the roadway geometry, pavement surface runoff is at least a two dimensional process. To account for this, one dimensional models either empirical or hydrodynamic describe the flow on one dimensional drainage paths [59, 68, 95]. They are determined from the two dimensional geometry as paths along the maximum gradient. Especially when bottom topography is irregular, though, flow paths are very difficult to determine because they possibly end or start within the model domain. In addition, effects like ponding, flow over adverse slopes or backwater effects at curbs can not be represented by the kinematic wave equation. Furthermore, two dimensional effects become significant in areas with strongly varying topography where lateral pressure gradients can not be neglected [25]. Thus, a kinematic wave model does not seem appropriate to model pavement surface runoff in combination with irregular topography and drainage facilities.

Contrary to one dimensional, steady state models, two dimensional models can not

be solved analytically. Instead, numerical methods have to be applied to solve these equations. For pavement surface runoff, a two dimensional model on the basis of the diffusion wave equation was recently developed in [25].

Although the full two dimensional dynamic wave equation would be the most accurate, attempts to implement such a model for pavement surface runoff were rare. Problems are reported in [56]. One reason is the high computational intensity, which made these kind of models slow and not practical. A second and even more important reason was lacking convergence and the occurrence of numerical instabilities due to the highly non-linear nature of the equation. Instabilities can occur in the presence of small water depths in combination with high friction slopes and strongly varying topography. They are mainly a problem of source term discretisation. Nowadays, computational power is steadily increasing and techniques like parallelisation of the simulation code allow to perform intensive simulations in acceptable time periods. Furthermore, research and development of numerical methods focuses on the aforementioned problems. Researches have recognised that an increased accuracy of the flux approximation is worthless as long as the source terms for bottom slope and friction slope are not treated correctly. There is extensive literature about an improved treatment of source terms in the Shallow Water Equations. This includes methods with an upwind-discretisation of the source terms [11, 15] and methods with an implicit [78, 113] or semi-implicit treatment of the source terms [10, 15, 70, 109].

Summarising, only a two dimensional hydrodynamic model based on either the diffusive or dynamic wave equation will cope with the requirements specified for an integral simulation of pavement surface runoff. Based on the development of computational resources and available numerical techniques, the full dynamic wave equation, thus, the Shallow Water Equations are chosen in this work. To the author's knowledge it will be the first attempt to simulate pavement surface runoff on the basis of the Shallow Water Equations.

Implementation of the model is done in the open-source frameworks DUNE [104] and DuMu^x [43]. DUNE (Distributed and Unified Numerics Environment) is a modular toolbox written in C++ for solving partial differential equations with grid-based methods. It supports the implementation of methods like Finite Elements (FE), Finite Volumes (FV), and also Finite Differences (FD). DuMu^x (DUNE for Multi-{Phase, Component, Scale,Physics, ...} Flow and Transport in Porous Media) is a simulator for flow and transport processes in porous media based on DUNE. It is developed at the Department of Hydromechanics and Modelling of Hydrosystems at the University of Stuttgart. DuMu^x provides the framework for a consistent implementation of CFD models with the Finite Volume Method. The implementation within DUNE/DuMu^x is advantageous in several ways. The framework specifies the software architecture of the model. It defines the basic model components, their function and their interaction. Therefore, structuring of the model can be omitted.

Since all models in the framework have the same architecture, their comprehensibility is increased. This also enables a fairly easy extension and modification of existing models. Finally, the framework also provides basic routines like grid generation, time discretisation etc., which can be readily used.

Due to the complexity of real world processes, a model is always an approximation of it including assumptions and simplifications. Figure 1.1 presents the typical stages in the model development process. They also roughly coincide with the outline to this work.

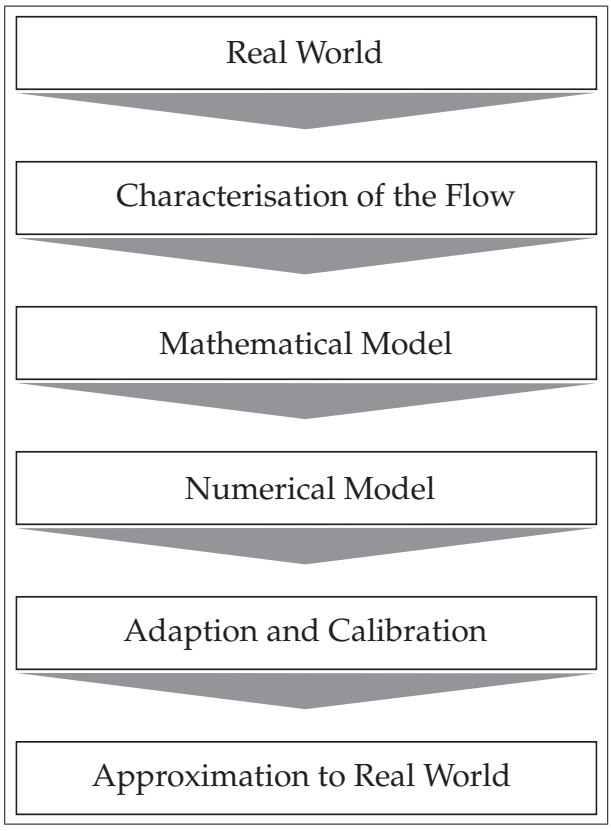

Figure 1.1.: Stages of model development.

Chapter 2 develops the basic model concepts by characterising pavement surface runoff. This includes the identification of the relevant influencing factors as well as the hydraulic characterisation of the underlying flow. Finally, the type and level of detail of the mathematical model to describe the flow are defined.

Chapter 3 deals with the mathematical model. It presents the derivation of the Shallow Water Equations from the Navier Stokes Equations starting from the most general formulation of fluid motion on the continuum scale. Afterwards, the mathematical behaviour of the Shallow Water Equations is discussed with respect to its influence on discretisation.

Chapter 4 presents the development of the numerical model, namely, the discretisation of the Shallow Water Equations with a cell-centred finite volume method. Two aspects are emphasised in the discretisation process: the approximation of the inter-cell fluxes and the discretisation of the source terms.

Chapter 5 covers the adaption and calibration of the numerical model to describe real flow problems. Besides a routine for the import and reconstruction of topographic data and the modelling of drainage facilities, the resistance model is a central part herein. Data to calibrate the resistance model originate from [56] and [95].

Chapter 6 finally presents some simulation results to demonstrate possible applications of the model. In addition, the model is compared to the one dimensional model developed in [56] and [95] and differences are discussed.

Chapter 7 summarises the work and provides an outlook on further topics of research.

2. Characterisation of Pavement Surface Runoff

A prerequisite for model development is the characterisation of the modelled flow. This includes the definition of the relevant influencing factors, which have to be considered, as well as the characterisation of the hydraulic nature of the flow. Depending on that the type of the mathematical model and its level of detail are chosen.

Pavement surface runoff is influenced by environmental and roadway related factors. Environmental factors are precipitation and wind. Roadway related factors are the geometry of the roadway, the topography of the pavement as well as the texture of the pavement surface. In the following sections, the factors of influence are described and their relevance to the model is discussed.

The hydraulic characterisation of pavement surface runoff includes the determination of the corresponding fluid and flow properties. From the hydraulic point of view pavement surface runoff is a gravity driven free surface flow. Therfore, characterisation is done on the basis of free surface flow classification as it can be found in open-channel flow related as well as fluid mechanics literature like [3, 26, 27, 55, 62, 111] and many more.

2.1. Factors of Influence

2.1.1. Precipitation

Any type of precipitation affects the pavement and riding characteristics, either in the form of liquid water drops like drizzle and rain or solid particles like snow and hail. With respect to drainage, the liquid form of precipitation is the one of interest. Therefore, the only precipitation type considered further is rainfall. It is the primary source for pavement surface runoff. First of all, rainfall determines the volume of water on the pavement. Second, it can increase resistance to flow by the kinetic energy released at the impact of the rain drops [102]. According to [63] the effect of rain drop impact decreases with increasing turbulence and is almost negligible in a turbulent flow regime. In [25] and [95] rain drop impact had no significant

effect at all on the flow variables. It was thus neglected in these models. Due to the complexity involved when modelling the raindrop impact and due to the lack of reliable data this effect is also not considered herein.

Runoff refers to the flow which is occurring during and immediately after a rainfall event. It is an unsteady, time-dependent process. Figure 2.1 shows a runoff profile where the water volume on the pavement is plotted over time. In general, three stages occur during a rainfall event: the wetting of the pavement, the steady flow condition and the drying process. If the surface is not perfectly smooth, the wetting and drying process are again divided in two stages and consequently the runoff process consists of five stages: At the beginning (t_0 - t_1), water starts occupying the available retention volume V_1 provided by the surface texture (Section 2.1.4). It is assumed that no considerable flow is taking place during this stage. As soon as the retention volume is exceeded, a continuous water film starts to develop on the pavement ($t_1 < t < t_2$) until the steady state is reached. The volume of the continuous water film is defined as moving volume ($V_2 - V_1$). During the steady state ($t_2 < t < t_3$), the water volume is constant. As soon as rainfall stops (t_3), the water film decreases. When the continuous water film has vanished, ($t \geq t_4$), the remaining water within the texture evaporates.

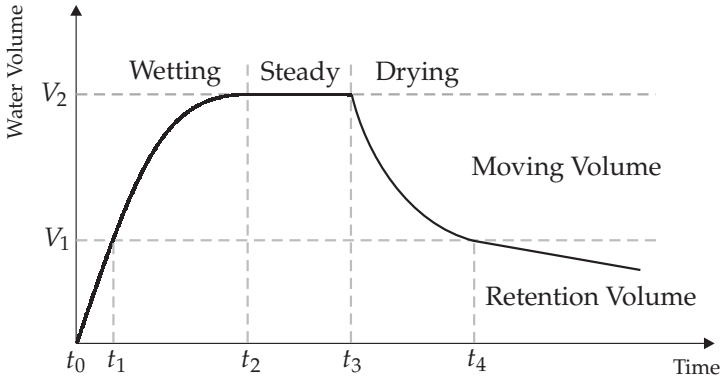

Figure 2.1.: Time-dependent profile of pavement surface runoff.

For drainage and hydroplaning considerations the steady state constitutes the worst case since the water depths reach their maximum. For this reason, most models only consider the steady state. However, if the pavement's topography is irregular with ruts and depressions, a steady model might overestimate the water depth because it does not consider the duration of a rainfall event and simply assumes that all depressions are completely filled. Furthermore, a steady model can not describe wetting and drying processes.

The water depth on the pavement at the steady state depends on the rainfall rate r [l/(s ha)], which in turn depends on the duration of the rainfall event t_r [min] and its

return rate $1/n$ [-] with n as the return period of the rain event in years. Generally, the rainfall rate decreases with increasing duration and decreasing return period. Therefore, rare and short rain events have high rainfall rates. For the design of highway drainage facilities, usually a return period of n = 1 is chosen [40]. Rainfall rates for a given duration and return period vary locally. There are two possibilities to determine these parameters, which are shortly described in the following paragraphs.

On the basis of statistical data, *Reinhold* [94] published basic rainfall rates $r_{15,1}$ for a rainfall event with $t_r = 15$ min and $n = 1$ for various locations in Germany [39]. Introducing a time factor $\varphi_{t_r,n}$, the basic rainfall rate $r_{15,1}$ can be transformed into a rainfall rate for an event with arbitrary duration and return period $r_{t_r,n}$ as follows:

$$r_{t_r,n} = \varphi_{t_r,n} \cdot r_{15,1}. \tag{2.1}$$

The determination of φ is also demonstrated in [39]. Although, rainfall rates and statistical data used to determine $\varphi_{t_r,n}$ originate from the first half of the twentieth century, the method is still suitable to roughly estimate the rainfall rate if no other data is available.

An up-to date and very extensive data base is provided by The German Meteorological Service, which published rainfall rates on the basis of statistical extreme value analyses within the KOSTRA-atlas (heavy rainfall totals in Germany) [31]. The data base in the current KOSTRA atlas is based on the time series from the years 1951 to 2000. Unlike the data of *Reinhold*, which is only available for a few distinct locations in Germany, KOSTRA values are available for the entire territory of Germany in a 71.5 km^2 raster. Another advantage is that the rainfall rates do not have to be converted by a time factor but origin from the statistical analysis. The data base in KOSTRA covers the range from a duration t_r = 5 min to 72 h and return rate from $1/n$ = 0.01 (n = 100 a) to 2 (n = 0.5 a). The KOSTRA atlas is the recommended data base also used in the new German guidelines for highway drainage design [40].

Besides the rainfall rate, often rainfall intensity i [mm/min] is used to characterise the magnitude of a rainfall event. The magnitude can reach from light, moderate and strong to very strong. Since rainfall intensity varies over time, commonly two values are used for the characterisation of a rainfall event: the maximum rainfall intensity which occurs within 6 or 10 minutes and the rainfall intensity averaged over one hour. Several classifications exist in the literature. The hourly values of [69], *Lucas* [79] and the *American Meteorological Society* [5] are presented in Table 2.1. Obviously, the values vary in a wide range. For example, *Koppe* defines a very strong rainfall event as $i \geq 0.8$ whereas *Lucas* gives $i \geq 1.7$. The classification of the *American Meteorological Society* does not even classify events as very strong. In this work, the classification of *Koppe* is used as a reference. It can be viewed as an average of the other classifications.

	Koppe	Lucas	American Meteorological Society
light	≤ 0.04	≤ 0.08	≤ 0.04
moderate	0.04 - 0.2	0.25 - 0.33	0.04 - 0.13
strong	0.2 - 0.8	0.4	≥ 0.13
very strong	≥ 0.8	≥ 1.7	-

Table 2.1.: Classification of rain events depending on rainfall intensity according to [5, 69] and [79].

2.1.2. Wind

The effect of wind on pavement surface runoff was experimentally investigated in [59] and [90] and also discussed in [95]. Wind can significantly influence the flow paths and depending on its direction increases or decreases resistance to flow. However, wind velocity and direction are highly variable and experimental data to include it into an empirical model is not sufficient. Further, the implementation of wind effects into a mathematical model is very complex due to turbulence effects at the boundary layer of water and air. Thus, no model has included wind effects so far, neither empirically nor mathematically. In addition, wind is not a mandatory parameter to model pavement surface runoff such as precipitation. Therefore, it is neglected in this study.

2.1.3. Roadway Geometry

The three dimensional roadway geometry is defined by the merging of the horizontal and vertical alignment as well as the cross sectional design of a roadway. The term alignment is used for the coupling of standardised highway design elements. Horizontal and vertical alignment and the cross section are designed in two space dimensions following specific design regulations. However, these parts are not totally independent. In fact, the interaction also decides whether the geometry meets the requirements set up for the alignment. These are: drainage capability, perceptibility, riding comfort and an appealing visual appearance. Before roadway geometry and its influence on pavement surface runoff are discussed, the two terms *geometry* and *topography* are demarcated because both are used within this work. Geometry refers to the three dimensional shape of a roadway determined by the joining of the design elements as already mentioned. Thus, roadway geometry is analytically

defined. The pavement surface is curved but assumed to be even. In contrast, topography refers to the pavement surface itself. A regular topography corresponds to a perfectly even surface as defined by the roadway geometry. An irregular topography corresponds to an uneven, real pavement surface with ruts and depressions. It can not be determined analytically but has to be determined via the reconstruction of point measurement data.

In Germany, there are two guidelines regulating the design of roads: the guidelines for motorway design (RAA, [41]) and the guidelines for rural highway design (RAL). The latter have not yet been introduced officially but can already be treated as state of the art. Unlike the former guidelines, which used design speed as the determining factor for the design regulations, the new guidelines introduce design categories (EKA for motorways and EKL for rural highways). The categorisation is based on the importance of a road with respect to its role within the overall network. Each category provides recommended cross sections and threshold values for the design parameters. The use of design categories ensures that roads with comparable importance are designed similarly. The design categories for motorways are presented in Table 2.2.

Design Category	EKA 1 A	EKA 1 B	EKA 2	EKA 3
Description	Interstate motorway	Interregional motorway	Motorway type road	Urban motorway

Table 2.2.: Design categories for motorways in Germany [41].

Recapitulating the requirements for the road alignment, the focus in this work clearly is on drainage capability. The geometry of the pavement defines the runoff direction, runoff velocity and the drainage path lengths. To guarantee quick runoff, the cross section is always inclined by a certain cross slope q_{p}. This results in a superelevation of the shoulders with respect to the axis of rotation. Usually, the axis of rotation lies in the centre of the carriageway. Minimum cross slope is $q_{\mathrm{p,min}} = 2.5\ \%$, which, to withstand centripetal forces, increases in curves depending on their radius. Nevertheless, there are sections within the alignment where drainage capability is not optimal, although design requirements are met, namely transition zones. In the subsequent paragraphs, the geometry of transition zones is described. Since hydroplaning risk increases in combination with high vehicle speeds and wide cross sections, design regulations for motorways and in particular those of EKA 1 A are exclusively considered.

Transition zones are a combination of elements in the horizontal alignment (transition curve) and the cross section design (superelevation transition). Figure 2.2

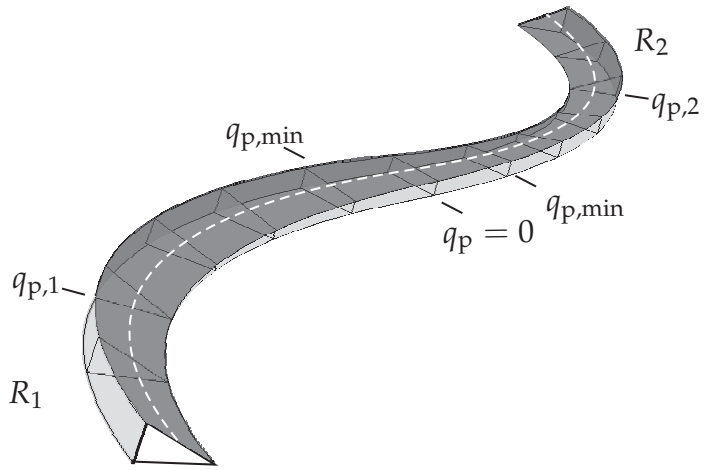

Figure 2.2.: Superelevation transition sketched in three dimensions.

shows the superposition of both transitions sketched in three dimensions. In the horizontal alignment transition zones link two opposite directed curves with constant radius (R_1 and R_2) and curvature (κ_1 and κ_2) by a clothoide as shown in Figure 2.3. Curvature and radius are correlated by

$$\kappa = \frac{1}{R}. \tag{2.2}$$

By the use of a clothoide, a linear change in curvature is guaranteed what results in a gentle and gradual change in path and lateral acceleration. This enhances the visual appearance of the alignment and, of course, the riding comfort. In Germany, transition curves are a mandatory design element. Details about different types of transition curves, their parameters and thresholds can be found in [41].

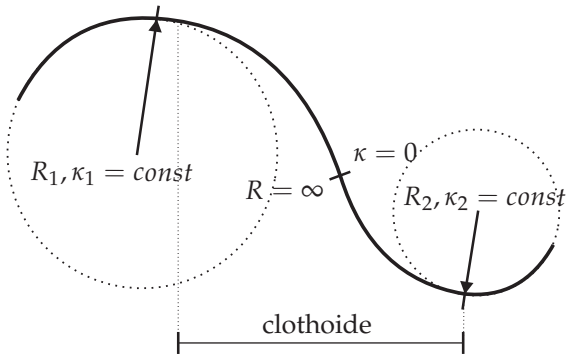

Figure 2.3.: Clothoide linking two curves with constant radius.

The transition of curvature does not affect the drainage capability of a transition zone. However, a change in curvature is always associated with a change in superel-

evation as already mentioned. Apart from distinct exceptions, the cross slope is usually directed to the inside of a curve what results in a positive superelevation of the shoulder along the outside. If curvature changes direction, superelevation also changes. In the centre of the transition, superelevation and cross slope are zero. Figure 2.4 shows the flow paths of a cross section with constant longitudinal and cross slope on the left and a superelevation transition with constant longitudinal slope on the right. Due to the change in superelevation flow paths in the transition are significantly longer. In addition, the gradient of the flow paths decreases within the transition since cross slope also decreases. Consequently, surface runoff is retarded what leads to an accumulation of water within the transition zone. The geometry of a superelevation transition is now described in more detail. It is used in Chapter 6 where the water depth distribution in a superelevation transition is used for the comparison of two pavement surface runoff models.

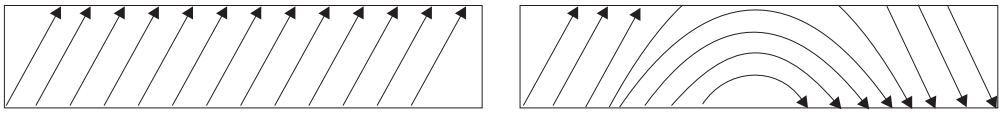

Figure 2.4.: Flow paths in a road section with constant cross slope (left) and in a superelevation transition (right), both with constant longitudinal slope.

Figure 2.5 shows the courses of the right and left shoulder within a superelevation transition between two curves with cross slopes $q_{p,1}$ and $q_{p,2}$. The superelevation of the shoulders can be determined by the cross slopes and the distance of the shoulders to the rotation axis a. The cross sections in front and behind the transition are sketched at the left and right side in the figure. The total length of the superelevation transition is L_V and the length of the central part of the transition is $L_{V,c}$. In case that $q_{p,1} = q_{p,2} = q_{p,min}$, the transition is referred to as 'basic' and it follows that $L_V = L_{V,c}$. Otherwise, the transition is referred to as 'divided' with $L_V > L_{V,c}$.

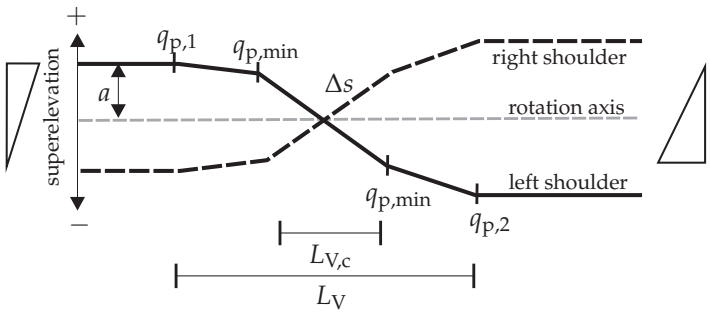

Figure 2.5.: Courses of the left and right shoulder within a superelevation transition between cross slopes $q_{p,1}$ and $q_{p,2}$.

For drainage capability the central part of a divided superelevation transition is crucial because cross slope drops below the minimum value $q_{\mathrm{p,min}}$. The design of the central part is thus strictly regulated by the guidelines. Since the central part corresponds to a basic transition, the geometry of a basic transition is considered exclusively herein.

Due to the change in superelevation, the shoulders are inclined with respect to the longitudinal slope by the relative gradient Δs defined by:

$$\Delta s = \frac{q_{\mathrm{p},1} - q_{\mathrm{p},2}}{L_{\mathrm{V,c}}}\, a. \tag{2.3}$$

To ensure sufficient drainage capability, Δs is limited to a minimum value of 0.1 a. If the axis of rotation is located in the centre of the cross section the maximum allowed central transition length $L_{\mathrm{V,c}}$ can therefore be determined from Equation (2.3) as

$$L_{\mathrm{V,c,max}} = \frac{q_{\mathrm{p,min}} - (-q_{\mathrm{p,min}})}{0.1\, a}\, a = \frac{2.5 - (-2.5)}{0.1\, a}\, a = 50 \tag{2.4}$$

If Δs falls below the minimum value and $L_{\mathrm{V,c}}$ exceeds 50 m, drainage capability decreases. For reasons of driving dynamics Δs is also limited to a maximum value, which is Δs = 0.9 %. Besides Δs, the guidelines also suggest a minimum longitudinal slope in superelevation transitions of s = 1 % to ensure sufficient drainage. Especially for three and four lane cross sections, the drainage capability in transition zones worsens even if the design regulations are met. Then, additional measures have to be applied, such as the installation of additional inlets, the use of porous asphalt or the construction of a diagonal superelevation transition [95].

2.1.4. Surface Texture

Pavement surface texture is a parameter which affects the road and riding characteristics in many ways. Some examples are noise generation, rolling resistance, skid resistance, splash and spray and surface runoff. The term texture is defined as the deviation of the real pavement texture from an even surface within a specified wavelength range. On the basis of wavelength λ_t, four ranges are distinguished [33]:

- microtexture: $\lambda_{\mathrm{t}} < 0.5$ mm,
- macrotexture: 0.5 mm $\leq \lambda_{\mathrm{t}} <$ 50 mm,
- megatexture: 50 mm $\leq \lambda_{\mathrm{t}} <$ 500 mm and
- unevenness: 500 mm $\leq \lambda_{\mathrm{t}}$.

Microtexture mainly affects skid resistance and is not considered further. The range of interest with respect to surface runoff is macrotexture, which affects the runoff in two ways. First, the texture provides a retention volume which depends on texture depth. If the present water volume totally occupies the retention volume, there is no continuous water film on the pavement. It is assumed that in this case, no considerable flow takes place. Second, the texture constitutes a rough surface which generates resistance to flow. This leads to retarded surface runoff and bigger water depths. Megatexture and unevenness also influence surface runoff. They can be described by varying bottom slopes and are treated as irregular bottom topography. They are not considered in this section.

The depth of the pavement texture is highly variable and differs with the surface cover used as wearing course. Table 2.3 displays the distribution of surface covers for the total network of German Federal Highways (freeways). Data originates from the Federal Highway Research Institute (BASt), effective 2006. Asphalt pavements form the majority with 57 %, these include stone matrix asphalt (SMA), dense graded asphalt (DGA) and open graded asphalt (OGA) surface covers. Concrete pavements make up 22 %.

SMA	DGA	OPA	Concrete	Others
32 %	23 %	2 %	22 %	21 %

Table 2.3.: Surface covers on German Federal Highways in percent (BASt).

Asphalt surface covers have a natural texture originating from the mixture of aggregates and bitumen. The texture mainly varies with the gradation of aggregates. In contrast, concrete covers have to be textured artificially after construction because aggregates are totally covered by cement. Texturing techniques are regulated in [42]. Some examples are the screeding of the surface with a jute fibre cloth or artificial turf. The most common technique, which has become standard for German freeways is to wash out the concrete surface to expose the aggregate structure.

The characterisation of the pavement surface texture is important for pavement management applications and quality control as well as for further research on the effects of texture on noise, skid resistance and runoff. Parameters used for the characterisation of the macrotexture can be of volumetric, geometric or hydraulic type. A well-known and widely used volumetric parameter is mean texture depth k. It is determined by the sand patch method [52]. A known volume V of glass beads or sand is distributed evenly over the pavement surface to form a circle, completely filling the surface voids as shown in Figure 2.6. The diameter D of the circle is measured and used to calculate the mean texture depth by:

$$k = \frac{4V}{\pi D^2}. \tag{2.5}$$

Thus, mean texture depth corresponds to the height of a cylinder with volume V. The advantage of this method is its easy application. Results may vary strongly though depending on the user.

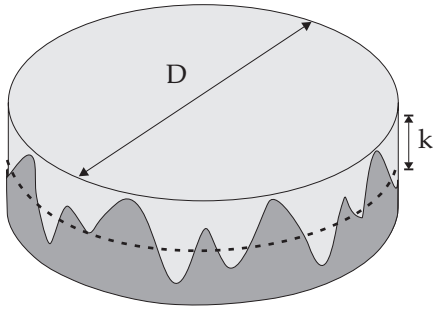

Figure 2.6.: Mean texture depth k determined with the sand patch method.

The fast development of digital profile measurement techniques enables the determination of geometric parameters on the basis of texture profile analysis. The analysis of pavement surface texture profiles is regulated by [33]. The two dimensional equivalent to mean texture depth is the estimated texture depth, which in turn is based on the geometric parameter mean profile depth (MPD). For the determination of mean profile depth the baseline of a sample, which is 100 mm in length, is divided in two equal halves as shown in Figure 2.7. The texture peaks of each half $z_{\text{max},1}$ and $z_{\text{max},2}$ are detected and mean profile depth is calculated as:

$$\text{MPD} = \frac{z_{\text{max},1} - z_{\text{max},2}}{2} - z_{\text{avg}} \;\; [\text{mm}] \tag{2.6}$$

where z_{avg} is the average profile depth. Finally, the estimated texture depth is determined via the empirical correlation:

$$\text{ETD} = 0.8\,\text{MPD} + 0.2 \;\; [\text{mm}]. \tag{2.7}$$

In general, results of profile analysis should be preferred to those of a volumetric approach due to higher accuracy and reproducibility. However, the volumetric method is still heavily used because there is no sound evaluation scheme for the estimated texture depth.

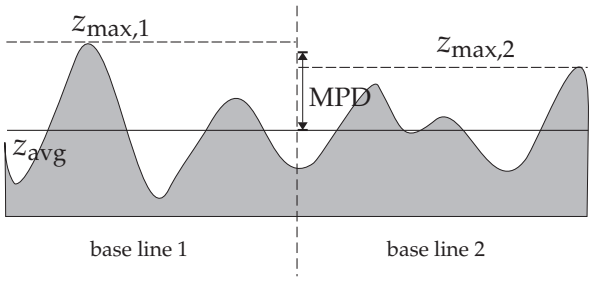

Figure 2.7.: Determination of mean profile depth from profile analysis.

Besides volumetric and geometric parameters such as the mean and estimated texture depth, textures can be characterised by the hydraulic parameter k_s (equivalent sand grain roughness). It represents an artificial roughness consisting of equally sized spheres with diameter k_s. It goes back to *Nikuradse* who did extensive experiments to discover the influence of roughness on pipe flow [89]. Roughness was generated by equally sized sand grains. Still, k_s is one of the most important parameters to classify fluid flow over rough surfaces. It can only be determined in hydraulic experiments. For various textures, k_s-values are listed in tables, e.g. in [26] or [62]. There are also approaches to estimate k_s via the grain size distribution obtained from sieving analysis [34].

2.2. Hydraulic Characterisation

Two types of parameters are important within a hydraulic characterisation: parameters which are related to the fluid itself (fluid properties) and parameters which describe the behaviour of the flow (flow properties). In the following, fluid and flow properties relevant for pavement surface runoff are shortly presented.

2.2.1. Fluid Properties

Density

Density ρ is defined as the mass per unit volume

$$\rho = \frac{m}{V} \ [\mathrm{kg/m^3}]. \tag{2.8}$$

If a change in pressure or temperature significantly affects density a fluid is said to be compressible. If density is constant and

$$\frac{d\rho}{dt} = 0 \tag{2.9}$$

a fluid is called incompressible. The density of water only slightly changes with temperature. In free surface flow applications, water is usually treated as an incompressible fluid with ρ = 1000 kg/m^3 = const.

Viscosity

Viscosity is a measure of internal friction. It describes the resistance of a fluid against shear stresses. A fluid is defined as Newtonian fluid if the shear stresses τ are pro-

portional to the velocity gradient perpendicular to the direction of shear

$$\tau = \mu \frac{du}{dx}. \tag{2.10}$$

In the equation, the proportionality factor is the dynamic viscosity μ. The kinematic viscosity is defined as

$$\nu = \frac{\mu}{\rho} \ [\mathrm{m}^2/\mathrm{s}]. \tag{2.11}$$

The viscosity of water decreases with increasing temperature. At 20° C $\mu = 10^{-3}$ kg/(m s). Since viscosity of water changes only slightly with temperature, it is usually set constant. In many applications it is even neglected and treated as a frictionless fluid because viscosity is very small. As an example, the dynamic viscosity of engine oil is $\mu = 10^{-1}$ kg/(m s) at 25° C. The viscosity of bitumen can even range from $10^4 < \mu < 10^{10}$ kg/(m s).

2.2.2. Flow Properties

Free surface flows can be classified according to the following criteria:

- temporal variation,
- spatial variation,
- internal flow conditions and
- direction of information propagation.

Temporal Variation

If the flow variables at a given location do not change with respect to time, a flow is called steady. In contrast, if flow variables at a given location do change with respect to time, the flow is unsteady. Pavement surface runoff can be clearly characterised as an unsteady flow, which, after a certain time reaches the steady state presumed that the rain event lasts long enough.

Spatial Variation

Considering a change of flow variables with respect to space, a flow can be uniform or varied. Uniform flow behaviour implies that the flow variables do not change along the flow path and that the cross section of the flow remains constant. If flow variables change along the flow path, one distinguishes between gradually

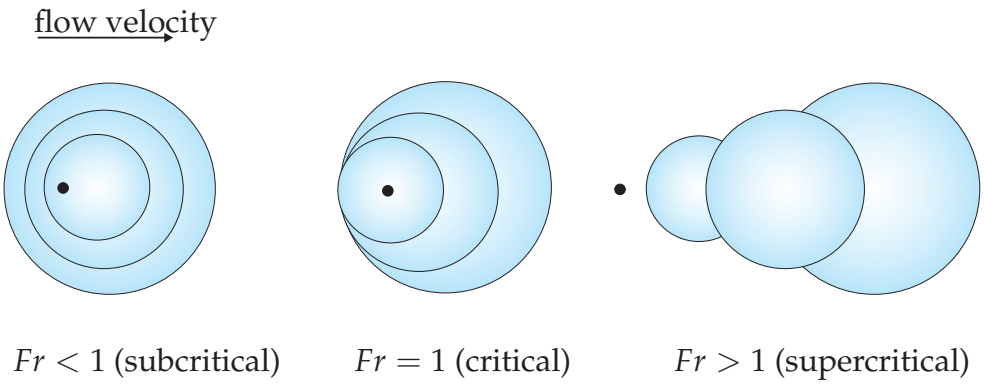

Figure 2.8.: Information propagation in subcritical, critical and supercritical flow.

varied and rapidly varied flow. In gradually varied flow, flow variables change slightly what may be caused by relatively smooth changes in bottom slope or texture. Rapidly varied flow is caused by abrupt changes for example in geometry (weirs, overfalls, change in cross section etc.). In those cases, the cross section of flow does not remain constant.

Due to rainfall, flow depth of pavement surface runoff is neither constant over time nor space. Furthermore, changes in bottom topography and texture influence the flow depth. Therefore, pavement surface runoff is a gradual varying flow.

Direction of Information Propagation

The ratio of inertial to gravitational forces is defined as the Froude Number

$$Fr = \frac{u}{\sqrt{gh}} \tag{2.12}$$

where u represents the mean flow velocity and $\sqrt{gh}$ the celerity of a gravity wave travelling on the surface of the flow. The Froude Number is the equivalent to the Mach Number in aerodynamics. It decides whether information is transported up and downstream or only in downstream direction. Figure 2.8 illustrates this issue. If the wave celerity is slower than the mean flow velocity, $Fr < 1$ and the flow is called subcritical. In this case, information is transported up and downstream what can give rise to backwater effects. If the wave celerity travels faster than the mean flow, $Fr > 1$ and information is only transported downstream. This is called the supercritical state. Typical phenomena of supercritical flow are discontinuous effects like shock waves. When, due to changes in channel geometry or bottom slope, flow changes from super to subcritical or vice versa, $Fr = 1$ at a certain location. This is called the critical flow state. Especially for free surface flows, the critical flow state is

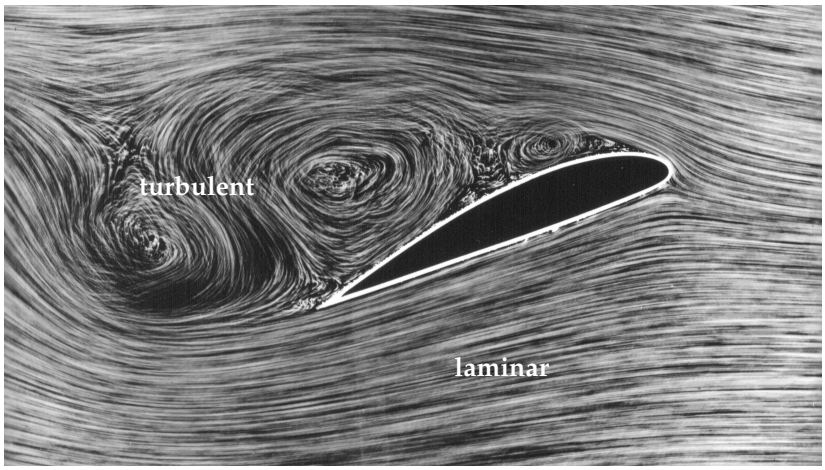

Figure 2.9.: Flow over an airfoil [32].

very important. It allows, for example, the determination of the discharge at weirs and overfalls. At the critical flow state, discharge becomes maximum.

The flow condition of pavement surface runoff is mainly subcritical. If water accumulates in ruts or is transported along the curb, flow can also become supercritical. The flow condition does not affect the mathematical model used. It rather affects the implementation of the boundary conditions because it defines the direction of information propagation at the boundary.

Internal Flow Condition

The internal flow condition can be either laminar or turbulent. Figure 2.9 shows the flow over an airfoil where both flow regimes are present. The direction of flow is from right to left. Beneath the airfoil, flow is laminar. Laminar flow appears as a movement of thin fluid layers which do not interfere and therefore streamlines do not intersect. The flow regime above and behind the airfoil is turbulent. Turbulent flow is characterised by a chaotic movement of the fluid particles and intersecting streamlines. Turbulence exerts two effects on the flow. First, the turbulent motion increases resistance to flow. Second it is responsible for dispersion processes and therefore plays an important role when transport processes are modelled. There are various approaches to model turbulence. A review of turbulence models can be found in [81].

The internal flow condition is defined by the ratio of inertial and viscous forces. It is known as the dimensionless Reynolds Number

$$Re = \frac{u r_{\mathrm{h}}}{\nu} \tag{2.13}$$

where u is the depth-averaged velocity, r_h the hydraulic radius and ν the kinematic viscosity. Pavement surface runoff is characterised by a small flow depth compared to the flow width. Therefore, the Reynolds Number can be formulated as:

$$Re = \frac{uh}{\nu} \tag{2.14}$$

with h as the flow depth.

If viscous forces dominate, Re becomes small and the flow is laminar. At higher Reynolds Numbers, inertial forces dominate and flow is characterised as turbulent. In between, there is a transitional zone where both forces influence the flow. This transitional zone can not be clearly defined and its extension strongly varies with the underlying flow. For simplification, a critical Reynolds Number is defined, which characterises the turnover of a flow regime from laminar to turbulent for practical purposes. In pipe flow, $Re_{crit} = 2300$ is used as turnover what roughly corresponds to $Re_{crit} = 600$ in free surface flows due to the changed hydraulic radius ($r_h = 4\ h$ for pipes). In overland flow $Re_{crit} = 1000$ is proposed for smooth surfaces. For vegetated surfaces the critical Reynolds Number goes even up to $Re_{crit} = 10^5$ [63].

The internal flow condition of pavement surface runoff can not be strictly identified as laminar or turbulent. Many publications have presumed laminar flow since water depth and velocity are fairly small [64, 68, 116]. In [25] and [61] though, measurements yielded Reynolds Numbers from $80 < Re < 17.000$. However, the rainfall intensity in these experiments varied from $i = 1.6$ - 4.2 mm/min, what can be classified as a very heavy rain storm referring to Table 2.1. Experiments in [95], in turn, lead to $Re < 6000$ for $i < 1.5$ mm/min. Recalling the definition of the critical Reynolds Number for free surface flows ($Re_{crit} = 600$) and fairly smooth overland flows ($Re_{crit} = 1000$) pavement surface runoff covers the whole range from laminar to turbulent. Keeping in mind the unknown extension of the transitional zone and the fact that even $i = 1.5$ mm/min already corresponds to a heavy rain storm event, pavement surface runoff will mainly be in the laminar and transitional flow regime.

2.3. Summary and Conclusions for Model Development

In the previous sections, parameters influencing pavement surface runoff and its hydraulic nature were discussed. For model development, the following conclusions can be drawn.

Pavement surface runoff is a time-dependent process. Although the steady state constitutes the worst case with respect to hydroplaning, the model should be time-dependent to include wetting and drying processes and to avoid an overestimation

of water depths when bottom topography is irregular. The main generator of surface runoff is rainfall. It can be considered as volumetric source which can vary in space and time.

Although many models use a one dimensional flow equation working along flow paths, pavement surface runoff is at least a two dimensional process. The direction of flow is determined by the surface geometry. Elements used for road alignment are mathematically defined. Therefore, they can be easily incorporated into the model via mathematical functions. For more complex roadway geometries, e.g. at intersections, and to account for the effect of megatexture and unevenness the model should also be able to process topographic point data originating from a design software or from lidar measurement data.

Besides roadway geometry, flow resistance significantly influences surface runoff. Among other factors like wind or raindrop impact, which are neglected, pavement surface texture is the most relevant parameter. Consequently, the pavement´s macrotexture is included as an explicit parameter to model flow resistance. Pavement surface textures strongly vary with time and of course with the material used. Therefore, the flow resistance model should be able to handle variable macrotextures.

The internal flow condition of pavement surface runoff covers the complete range from laminar to turbulent. However, the focus is not on modelling dispersion effects. Instead, the increased flow resistance due to turbulence is of interest. Therefore, turbulence is not explicitly modelled. Implicitly, it is included in the resistance model since turbulence effects were present in the experiments.

Unlike in open-channel flow, the flow depth of pavement surface runoff is fairly small compared to the horizontal scale. In addition, surface runoff is dominated by horizontal movements. Therefore, two simplifications can be made. First, the vertical velocity component is much smaller than the horizontal velocity components and consequently a hydrostatic pressure distribution can be assumed. Second, the horizontal velocity components are distributed equally over flow depth and the vertical velocity component can be omitted. This leads to depth-averaged equations. A set of equations describing depth-averaged gravity-driven free surface flows are the Shallow Water Equations (SWE). Due to the assumption of a hydrostatic pressure distribution the Shallow Water Equations are only applicable with gentle bottom slopes. According to [60], the maximum slope should not exceed 10 %. The guidelines for highway design propose a maximum longitudinal slope of 6 % for EKA 1 A [41] . In the majority of cases, except very steep urban or rural roads, the Shallow Water Equations are therefore applicable to describe pavement surface runoff. The derivation and characterisation of the Shallow Water Equations is done in the following chapter.

3. The Shallow Water Equations

In Chapter 2, the relevant parameters and characteristics of pavement surface runoff were discussed. Based on the findings, the two dimensional, depth-averaged Shallow Water Equations are chosen to describe the flow. Research on the Shallow Water Equations is still a subject of high interest to mathematicians, physicians and engineers. On the one hand, numerical methods are continuously developed and enhanced to improve the reproduction of the mathematical characteristics of the equations. On the other hand, the Shallow Water Equations are applied to practical flow problems. There is a wide range of applications in coastal and hydraulic engineering. A good overview is given in [110]. A few examples are: wave run up estimation and tsunami simulation, dam break and flood wave propagation, simulation of waves caused by landslides, flood plain inundation in combination with the simulation of the transport of dissolved substances or the design of urban sewer systems.

This chapter deals with the derivation of the Shallow Water Equations starting from the most general formulation of fluid motion on the continuum scale. Afterwards, the Shallow Water Equations are characterised mathematically. This strongly influences the choice of the numerical method used to solve the equations.

3.1. Derivation

Fluid motion is described using the fundamental concept of conservation of the extensive fluid properties. Extensive fluid properties are for example mass, momentum and energy. They depend on the system size. The opposite of extensive properties are intensive properties. They are independent of the system size e. g. velocity. The concept of conservation states that the extensive fluid and flow properties in a considered volume can not appear or dissappear without any reason. Such reasons may be flux across the volume´s boundary, source or sink terms or forces acting on the volume. Applying the concept of conservation allows to formulate a general conservation law for fluid motion, which constitutes a continuum approach for fluid dynamics. Since this issue is regarded essential, the derivation of the general conservation law is presented herein before dealing with the derivation of the Shallow Water Equations in particular.

3.1.1. Reynolds Transport Theorem

The mathematical description of fluid motion on the continuum scale is based on two approaches, namely the Lagrangian and Eulerian approach. Both approaches object to model the change in fluid properties over time as well as in space. If a single fluid particle is considered, the Lagrangian description tracks this particle on its way through the flow field. In contrast, the Eulerian description establishes a fixed point respectively frame in space and monitors how fluid particles are passing by. The extension to a volume filled with fluid particles yields the following definitions:

- System: a system is a volume which is always defined by the same particles. Therefore, no particles can cross the system's boundary. The shape of the system and its position do however change with time. If the system size is reduced to zero it equals a single particle (Lagrangian description).
- Control volume (CV): a control volume is a fixed frame. Particles cross the control volume's boundaries as they pass along. The volume and position of a control volume do not necessarily change with time. If a control volume is reduced to zero it equals a single fixed point or frame in space (Eulerian description).

Applying the Lagrangian description, the change of an extensive fluid property $\Phi(x, y, z, t)$ of a fluid particle can be described by:

$$\frac{d\Phi(x,y,z,t)}{dt} = \frac{\partial \Phi}{\partial t} + \frac{\partial \Phi}{\partial x}\frac{\partial x}{\partial t} + \frac{\partial \Phi}{\partial y}\frac{\partial y}{\partial t} + \frac{\partial \Phi}{\partial z}\frac{\partial z}{\partial t} \tag{3.1}$$

what can be rearranged to

$$\frac{d\Phi(x,y,z,t)}{dt} = \frac{\partial \Phi}{\partial t} + \Phi(\mathbf{v} \cdot \nabla) \tag{3.2}$$

where $\mathbf{v}$ is the three dimensional velocity vector. Equation (3.2) is called the material or total derivative of Φ, which is split into a temporal part and a convective part. The temporal part accounts for the change of Φ over time at a fixed position whereas the convective part accounts for the change in Φ due to the shift in space generated by the particle's velocity. Generally, the same considerations apply for a system. In fluid dynamics, the Eulerian approach is usually preferred to the Lagrangian. The transformation of Equation (3.2) to the Eulerian description is done using the Reynolds Transport Theorem, which will be derived subsequently.

A system of fluid particles V_{sys} is considered, which coincides with a control volume V_{CV} at time t as shown in Figure 3.1. The control volume is further assumed to be fixed. After a time Δt the system volume has partially moved out of the control

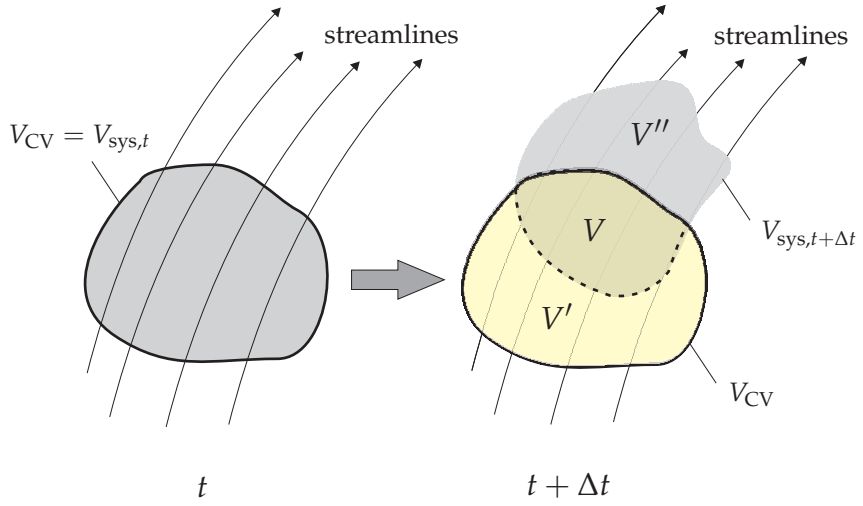

Figure 3.1.: Position of a control volume V_{CV} and system V_{sys} at times t and $t + \Delta t$.

volume along the streamlines and may have changed in shape. The change of Φ over time can be written as:

$$\frac{d\Phi}{dt} = \lim_{\Delta t \to 0} \frac{(\Phi_{V_{Sys,t+\Delta t}} - \Phi_{V_{Sys,t}})}{\Delta t}. \tag{3.3}$$

Equation (3.3) can be rearranged applying the following definitions: Let V be the volume which is occupied by both states t and $t + \Delta t$. Further, let V' be the part of the control volume which is not occupied by the system and V'' the part of the system which is not within the control volume. Then, the change of Φ over time reads:

$$\frac{d\Phi}{dt} = \lim_{\Delta t \to 0} \frac{(\Phi_{V,t+\Delta t} + \Phi_{V'',t+\Delta t}) - (\Phi_{V,t} + \Phi_{V',t})}{\Delta t}. \tag{3.4}$$

Setting $\Phi_{V,t+\Delta t} = \Phi_{V_{CV},t+\Delta t} - \Phi_{V',t+\Delta t}$ and rearranging the equation finally yields

$$\frac{d\Phi}{dt} = \lim_{\Delta t \to 0} \frac{\Phi_{V_{CV},t+\Delta t} - \Phi_{V_{CV},t}}{\Delta t} + \lim_{\Delta t \to 0} \frac{\Phi_{V'',t+\Delta t} - \Phi_{V',t}}{\Delta t}. \tag{3.5}$$

Equation (3.5) also consists of two parts. The first part accounts for the change of Φ within the control volume. The second part accounts for the change of Φ caused by the shift in space, which transports Φ across the control volume's surface. This shift is further on referred to as flux. The flux through the surface A_{CV} of the control volume can be formulated as

$$\int_{A_{CV}} \Phi \, \mathbf{v} \cdot \mathbf{n} \, dA_{CV} \tag{3.6}$$

where $\mathbf{v}$ is the velocity vector and $\mathbf{n}$ the normal vector of the surface. The change of Φ in the control volume can therefore be expressed as

$$\frac{d}{dt} \int_{V_{CV}} \Phi \, dV_{CV} = \int_{V_{CV}} \frac{\partial}{\partial t} \Phi \, dV_{CV} + \int_{A_{CV}} \Phi \, \mathbf{v} \cdot \mathbf{n} \, dA_{CV} \tag{3.7}$$

and applying the Gauss Theorem

$$\frac{d}{dt}\int\limits_{V_{\mathrm{CV}}} \Phi \, dV_{\mathrm{CV}} = \int\limits_{V_{\mathrm{CV}}} \frac{\partial}{\partial t}\Phi \, dV_{\mathrm{CV}} + \int\limits_{V_{\mathrm{CV}}} \nabla \cdot (\Phi \, \mathbf{v}) \, dV_{\mathrm{CV}}. \tag{3.8}$$

Since the control volume is assumed to be fixed (time-independent in shape and position), the partial time derivative on the right side of Equation (3.8) can be moved in front of the integral. This yields:

$$\frac{d}{dt}\int\limits_{V_{\mathrm{CV}}} \Phi \, dV_{\mathrm{CV}} = \frac{\partial}{\partial t}\int\limits_{V_{\mathrm{CV}}} \Phi \, dV_{\mathrm{CV}} + \int\limits_{V_{\mathrm{CV}}} \nabla \cdot (\Phi \, \mathbf{v}) \, dV_{\mathrm{CV}}. \tag{3.9}$$

Equations (3.8) and (3.9) are called the Reynolds Transport Theorem. It transforms the differential formulation of fluid motion to an integral formulation referenced to a control volume. Physically, it states that the rate of change of a fluid property depends on the change in the control volume and the net flux through the control volume´s surface. Besides the flux, source terms or forces acting on the control volume can influence the rate of change of a property. By adding source terms and relevant forces to the basic equation (Equation (3.8)), a variety of continuum scale conservation laws can be derived. In the subsequent section, the Navier-Stokes Equations are derived using the Reynolds Transport Theorem. Further reading about the Reynolds Transport Theorem can be found in [55] or [92].

3.1.2. Navier-Stokes-Equations

The Navier Stokes Equations are the basic equations in fluid dynamics to model Newtonian fluids on a continuum scale. They are subsequently derived using the Reynolds Transport Theorem (3.1.1). The derivation presented herein is done for an incompressible fluid and laminar flow conditions. The extensive properties of the flow are mass and momentum. Due to incompressibility also a temperature-independent flow is assumed. Consequently, energy as a third extensive property is neglected. The extensive properties are further on called conserved variables.

Conservation of Mass

The mass of a volume is defined by its density as $m = \rho V$. Following Equation (3.9) mass conservation can be formulated as:

$$\frac{\partial}{\partial t}\int\limits_{V} \rho \, dV + \int\limits_{\partial V} \rho \, \mathbf{v} \cdot \mathbf{n} \, dA = q, \tag{3.10}$$

where q is a source term. If the fluid is incompressible, change in density over time is zero and the equation reduces to:

$$\int_{\partial V} \mathbf{v} \cdot \mathbf{n} \, dA = q. \tag{3.11}$$

Conservation of Momentum

According to Newton's second law, momentum is defined as the product of mass and velocity $(m \cdot v)$. The change of momentum per unit time is a force

$$F = \frac{d(m \cdot v)}{dt} = m \cdot a$$

with a being the acceleration, assuming that mass does not change with time. Source terms influencing momentum can be any type of force acting on the control volume. These can be surface forces due to shear stresses $\boldsymbol{\tau}$ or pressure p:

$$F_{\text{surface}} = \boldsymbol{\tau} \cdot \mathbf{n} A - \nabla p V$$

and forces acting on the volume, like gravity forces:

$$F_{\text{volume}} = \rho g V.$$

If momentum and source terms are inserted in Equation (3.9), the conservation of momentum can be written as:

$$\frac{\partial}{\partial t} \int_V \rho \mathbf{v} \, dV + \int_{\partial V} (\rho \mathbf{v}) \, \mathbf{v} \cdot \mathbf{n} \, dA = \int_{\partial V} \boldsymbol{\tau} \cdot \mathbf{n} \, dA - \int_V \nabla p \, dV + \int_V \rho g \, dV. \tag{3.12}$$

Equation (3.12) in combination with (3.11) are called the Navier-Stokes Equations. In differential notation, the equations can be formulated as:

$$\begin{aligned} \nabla \cdot \mathbf{v} &= q \\ \rho \frac{d\mathbf{v}}{dt} &= -\nabla p + \nabla \boldsymbol{\tau} + \rho \mathbf{g}. \end{aligned} \tag{3.13}$$

To close the system of four partial differential equations and five unknowns an additional relation is needed. It is derived from the property of Newtonian fluids (see Section 2.2). Inserting Equation (2.10) yields:

$$\begin{aligned} \nabla \cdot \mathbf{v} &= q \\ \rho \frac{d\mathbf{v}}{dt} &= -\nabla p + \mu \nabla^2 \mathbf{v} + \rho \mathbf{g}. \end{aligned} \tag{3.14}$$

To this day, the Navier Stokes Equations are the standard in the mathematical description of fluid dynamics on the continuum scale and no one has yet obtained a general analytical solution to them. In many practical flow problems not necessarily all forces and fluid properties which were described above are relevant. This leads to simplified equations such as the Euler or the Shallow Water Equations (SWE), which are presented in the following sections.

3.1.3. Incompressible Euler Equations

Shear stresses in a fluid are conveyed by fluid viscosity. The Euler Equations hold for ideal frictionless fluids where no shear stresses due to viscosity appear. It follows that $\mu = 0$ and $\tau_{ij} = 0$. With this simplification and assuming that gravity acts in z-direction of a cartesian coordinate system, the Navier-Stokes Equations in differential form can be simplified to obtain the Incompressible Euler Equations as follows:

$$\begin{aligned}
\frac{\partial u}{\partial x} + \frac{\partial v}{\partial y} + \frac{\partial w}{\partial z} &= 0 \\
\frac{\partial u}{\partial t} + u\frac{\partial u}{\partial x} + v\frac{\partial u}{\partial y} + w\frac{\partial u}{\partial z} &= -\frac{1}{\rho}\frac{\partial}{\partial x}p \\
\frac{\partial v}{\partial t} + u\frac{\partial v}{\partial x} + v\frac{\partial v}{\partial y} + w\frac{\partial v}{\partial z} &= -\frac{1}{\rho}\frac{\partial}{\partial y}p \\
\frac{\partial w}{\partial t} + u\frac{\partial w}{\partial x} + v\frac{\partial w}{\partial y} + w\frac{\partial w}{\partial z} &= -\frac{1}{\rho}\frac{\partial}{\partial z}p - g.
\end{aligned} \tag{3.15}$$

3.1.4. Shallow Water Equations

If water is treated as an ideal frictionless fluid, the Shallow Water Equations can be derived from the Incompressible Euler Equations by integrating them over flow depth. Figure 3.2 shows the variables of the Shallow Water Equations. Flow variables are water depth h and the two horizontal velocity components u and v. Bottom elevation is denoted with z_b and water level with η. The water level is the sum of bottom elevation and water depth. In contrast to the Incompressible Euler Equations, the Shallow Water Equations represent flows with a free surface. Further on, a hydrostatic pressure distribution is assumed. Before the depth-averaged Shallow Water Equations are derived via integration over flow depth, the Incompressible Euler Equations are further simplified by application of the hydrostatic pressure condition and the condition for the free surface.

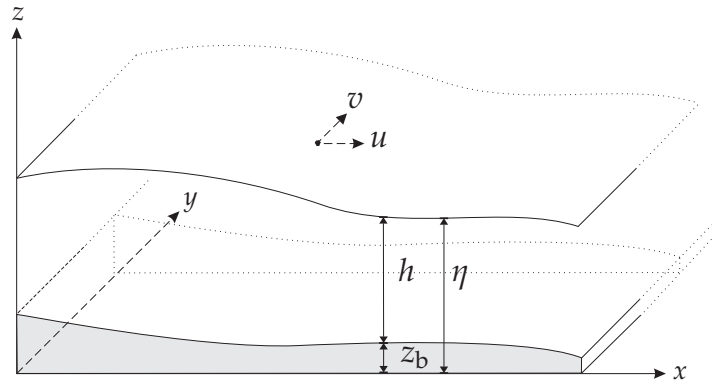

Figure 3.2.: Variables used in the Shallow Water Equations.

Hydrostatic Pressure Condition

The hydrostatic pressure condition implies that the vertical velocity component is much smaller than the horizontal components: $w << u$ and v. Therefore, the momentum equation in z-direction of Equation (3.15) reduces to

$$\frac{\partial}{\partial z}p + \rho g = 0. \tag{3.16}$$

Integrating this over flow depth and assuming constant density over depth yields

$$p(z) = p_{\text{ref}} + \rho g(z_b + h - z), \tag{3.17}$$

where p_{ref} stands for a spatially constant reference pressure, e.g. atmospheric pressure. In the following, Equation (3.17) is differentiated in x and y-direction to apply the hydrostatic pressure condition to the momentum equations. Differentiation in x-direction yields:

$$\frac{\partial}{\partial x}p(z) = \frac{\partial}{\partial x}p_{\text{ref}} + \rho g\frac{\partial}{\partial x}(z_b + h)$$

and with spatially constant p_{ref}:

$$\frac{\partial p}{\partial x} = g(\frac{\partial z_b}{\partial x} + \frac{\partial h}{\partial x}). \tag{3.18}$$

For the y-direction, the same holds:

$$\frac{\partial p}{\partial y} = g(\frac{\partial z_b}{\partial y} + \frac{\partial h}{\partial y}). \tag{3.19}$$

Inserting Equations (3.18) and (3.19) in the Incompressible Euler Equations yields the three dimensional Shallow Water Equations:

$$\begin{aligned} \frac{\partial u}{\partial x} + \frac{\partial y}{\partial y} + \frac{\partial w}{\partial z} &= 0 \\ \frac{\partial u}{\partial t} + u\frac{\partial u}{\partial x} + v\frac{\partial u}{\partial y} + w\frac{\partial u}{\partial z} &= -g(\frac{\partial z_b}{\partial x} + \frac{\partial h}{\partial x}) \\ \frac{\partial v}{\partial t} + u\frac{\partial v}{\partial x} + v\frac{\partial v}{\partial y} + w\frac{\partial v}{\partial z} &= -g(\frac{\partial z_b}{\partial y} + \frac{\partial h}{\partial y}) \end{aligned} \tag{3.20}$$

Boundary Conditions for Free Surface Flow

If the water depth is very small compared to the horizontal scale of the domain it can be supposed that the vertical changes of the horizontal velocity components are negligible and therefore depth-averaged values are justifiable. When integrating the Shallow Water Equations over depth, the boundary conditions for free-surface flow have to be considered. They are of kinematic and dynamic nature.

The kinematic boundary condition states that for a free surface flow over a non-infiltrating bottom, no water can penetrate into the air or ground (free-slip condition [57]). Therefore, the contribution of the velocity vector normal to the ground $\mathbf{n}_\mathrm{b}$ is zero unless there is a source or sink. At the water level the contribution of the velocity vector normal to the water level $\mathbf{n}_\eta$ has to equal the change in water level position $\partial\eta/\partial t$. The boundary conditions can be formulated as

$$\mathbf{n}_\mathrm{b} \cdot \mathbf{v} = \begin{pmatrix} -\partial z_\mathrm{b}/\partial x \\ -\partial z_\mathrm{b}/\partial y \\ 1 \end{pmatrix} \cdot \begin{pmatrix} u_\mathrm{b} \\ v_\mathrm{b} \\ w_\mathrm{b} \end{pmatrix} = -\frac{\partial z_\mathrm{b}}{\partial x}u_\mathrm{b} - \frac{\partial z_\mathrm{b}}{\partial y}v_\mathrm{b} + w_\mathrm{b}{=}0$$

$$\mathbf{n}_\eta \cdot \mathbf{v} = \begin{pmatrix} -\partial\eta/\partial x \\ -\partial\eta/\partial y \\ 1 \end{pmatrix} \cdot \begin{pmatrix} u_\mathrm{b} \\ v_\mathrm{b} \\ w_\mathrm{b} \end{pmatrix} = -\frac{\partial\eta}{\partial x}u_\eta - \frac{\partial\eta}{\partial y}v_\eta + w_\eta{=}\frac{\partial\eta}{\partial t}$$

where the subscript b refers to the bottom and η to the water level. Solving for the vertical velocity component at the bottom and at the water level yields:

$$w_\mathrm{b} = \frac{\partial z_\mathrm{b}}{\partial x}u_\mathrm{b} + \frac{\partial z_\mathrm{b}}{\partial y}v_\mathrm{b} \tag{3.21}$$

$$w_\eta = \frac{\partial\eta}{\partial t} + \frac{\partial\eta}{\partial x}u_\eta + \frac{\partial\eta}{\partial y}v_\eta. \tag{3.22}$$

The dynamic boundary condition also implies that the fluid does not move on the ground: $\mathbf{v}_\mathrm{b} = 0$.

Integration over Flow Depth

Using the boundary conditions for free surface flow the two dimensional, depth-averaged Shallow Water Equations can be obtained by integrating Equation (3.20) over flow depth. Exemplarily, the integration of the continuity equation and the momentum equation in x-direction is shown in detail.

The integration of the continuity equation can be written as:

$$\int_{z_\mathrm{b}}^{\eta} \frac{\partial u}{\partial x}\, dz + \int_{z_\mathrm{b}}^{\eta} \frac{\partial v}{\partial y}\, dz + \int_{z_\mathrm{b}}^{\eta} \frac{\partial w}{\partial z}\, dz = 0. \tag{3.23}$$

For all terms of the equation, the Leibniz Rule has to be applied, which states:

$$\frac{d}{\partial x} \int_{a}^{b} f(x)\, dz = \int_{a}^{b} \frac{\partial}{\partial x} f(x)\, dz + f(b) \cdot b'(x) - f(a) \cdot a'(x). \tag{3.24}$$

It follows for the first term of Equation (3.28):

$$\int_{z_\mathrm{b}}^{\eta} \frac{\partial u}{\partial x}\, dz = \frac{d}{\partial x} \int_{z_\mathrm{b}}^{\eta} u\, dz - u_\eta \frac{\partial \eta}{\partial x} + u_\mathrm{b} \frac{\partial z_\mathrm{b}}{\partial x} = \frac{\partial \tilde{u} h}{\partial x} - u_\eta \frac{\partial \eta}{\partial x} + u_\mathrm{b} \frac{\partial z_\mathrm{b}}{\partial x} \tag{3.25}$$

where $\tilde{u}$ is the depth-averaged velocity defined as

$$\tilde{u} = \frac{1}{h} \int_{z_\mathrm{b}}^{\eta} u\, dz. \tag{3.26}$$

Transformation of the entire continuity equation according to Equation 3.25 yields:

$$\begin{aligned} &\int_{z_\mathrm{b}}^{\eta} \left(\frac{\partial u}{\partial x}\, dz + \frac{\partial v}{\partial y}\, dz + \frac{\partial w}{\partial z}\, dz\right) = \\ &\qquad = \frac{\partial \tilde{u} h}{\partial x} + \frac{\partial \tilde{v} h}{\partial y} - \left(u_\eta \frac{\partial \eta}{\partial x} + v_\eta \frac{\partial \eta}{\partial x} - w_\eta\right) + \left(u_\mathrm{b} \frac{\partial z_\mathrm{b}}{\partial x} + v_\mathrm{b} \frac{\partial z_\mathrm{b}}{\partial y} - w_\mathrm{b}\right). \end{aligned} \tag{3.27}$$

Applying the conditions for free surface flow, which give expressions for w_b and w_H (Equations (3.21) and (3.22)) and assuming that the bottom z_b does not move

$$\frac{\partial z_\mathrm{b}}{\partial t} = 0,$$

Equation (3.27) can be simplified to yield the depth-averaged continuity equation:

$$\frac{\partial h}{\partial t} + \frac{\partial \tilde{u} h}{\partial x} + \frac{\partial \tilde{v} h}{\partial y} = 0. \tag{3.28}$$

The integration of the momentum equation is splitted in two parts: the integration of the conservative part and the integration of the pressure gradient:

$$\underbrace{\frac{\partial u}{\partial t} + u\frac{\partial u}{\partial x} + v\frac{\partial u}{\partial y} + w\frac{\partial u}{\partial z}}_{\text{Conservative Part}} = \underbrace{-\frac{1}{\rho}\frac{\partial p}{\partial x}}_{\text{Pressure Gradient}} \quad . \tag{3.29}$$

The steps of the integration are shown for the momentum equation in x-direction. The integration in y-direction is done analogically.

Conservative Part For the integration of the conservative part the momentum equation is transformed to:

$$\int_{z_\mathrm{b}}^{\eta} \left(\frac{\partial u}{\partial t} + u\frac{\partial u}{\partial x} + v\frac{\partial u}{\partial y} + w\frac{\partial u}{\partial z}\right) = \int_{z_\mathrm{b}}^{\eta} \left(\frac{\partial u}{\partial t} + \frac{\partial u^2}{\partial x} + \frac{\partial uv}{\partial y} + \frac{\partial uw}{\partial z}\right). \tag{3.30}$$

Applying the Leibniz rule (Equation (3.24)) to the right side of Equation (3.30) yields:

$$\begin{aligned}
&\int_{z_\mathrm{b}}^{\eta} \frac{\partial u}{\partial t}\,dz + \int_{z_\mathrm{b}}^{\eta} \frac{\partial u^2}{\partial x}\,dz + \int_{z_\mathrm{b}}^{\eta} \frac{\partial uv}{\partial y}\,dz + \int_{z_\mathrm{b}}^{\eta} \frac{\partial uw}{\partial z}\,dz = \\
&\qquad = \frac{\partial}{\partial t}\int_{z_\mathrm{b}}^{\eta} u\,dz + \frac{\partial}{\partial x}\int_{z_\mathrm{b}}^{\eta} u^2\,dz + \frac{\partial}{\partial y}\int_{z_\mathrm{b}}^{\eta} uv\,dz + u_\eta w_\eta - u_\mathrm{b} w_\mathrm{b} - \\
&\qquad\qquad - \left[u_\eta^2 \frac{\partial \eta}{\partial t} + u_\eta^2 \frac{\partial \eta}{\partial x} + u_\eta v_\eta \frac{\partial \eta}{\partial y}\right] + \left[u_\mathrm{b}^2 \frac{\partial z_\mathrm{b}}{\partial x} + u_\mathrm{b} v_\mathrm{b} \frac{\partial z_\mathrm{b}}{\partial y}\right].
\end{aligned} \tag{3.31}$$

Inserting the equations for w_η and w_b (Equation (3.21) and (3.22) and averaging the velocity according to Equation (3.26) yields:

$$\frac{\partial h\tilde{u}}{\partial t} + \frac{\partial \tilde{u^2} h}{\partial x} + \frac{\partial \tilde{u}\tilde{v} h}{\partial y} + \underbrace{\frac{\partial}{\partial x}\int_{z_\mathrm{b}}^{\eta} (\tilde{u} - u)^2\,dz + \frac{\partial}{\partial y}\int_{z_\mathrm{b}}^{\eta} (\tilde{u} - u)(\tilde{v} - v)\,dz}_{\text{Dispersion}}. \tag{3.32}$$

The remaining integral expressions describe dispersion effects. They are induced by a non uniform velocity distribution over depth due to the deviation of the real velocities from the averaged velocity. Most often, dispersion effects are neglected [88].

Pressure Gradient The pressure gradient defined in Equation (3.29) can be rearranged to:

$$\int_{z_b}^{\eta} -\frac{1}{\rho}\frac{\partial}{\partial x}p(z)\,dz = \int_{z_b}^{\eta} -\frac{\partial}{\partial x}g(\eta - z)\,dz \tag{3.33}$$

Applying the Leibniz Rule (Equation (3.24)) yields:

$$\begin{aligned}\int_{z_b}^{\eta} \frac{\partial}{\partial x}g(\eta - z)\,dz &= \frac{\partial}{\partial x}g\int_{z_b}^{\eta}(\eta - z)\,dz + g(\eta - z_b)\frac{\partial z_b}{\partial x} \\ &= \frac{\partial}{\partial x}(\frac{1}{2}gh^2) + gh\frac{\partial z_b}{\partial x}.\end{aligned} \tag{3.34}$$

The depth-averaged momentum equation in x-direction can finally be stated as:

$$\frac{\partial \tilde{u}h}{\partial t} + \frac{\partial \tilde{u}^2 h}{\partial x} + \frac{\partial \tilde{u}\tilde{v}h}{\partial y} + \frac{\partial}{\partial x}(\frac{1}{2}gh^2) + gh\frac{\partial z_b}{\partial x} = 0. \tag{3.35}$$

Joining the depth-integrated continuity equation (Equation (3.28)) and the momentum equations, denoting $\tilde{u}$ further with u and assuming a flat bottom finally yields the depth-averaged Shallow Water Equations:

$$\frac{\partial}{\partial t}\begin{pmatrix} h \\ uh \\ vh \end{pmatrix} + \frac{\partial}{\partial x}\begin{pmatrix} uh \\ u^2h + \frac{1}{2}gh^2 \\ uvh \end{pmatrix} + \frac{\partial}{\partial y}\begin{pmatrix} vh \\ uvh \\ v^2h + \frac{1}{2}gh^2 \end{pmatrix} = \begin{pmatrix} 0 \\ ghS_{0,x} \\ ghS_{0,y} \end{pmatrix} \tag{3.36}$$

Equation (3.60) describes shallow water dynamics for a frictionless fluid without any source terms besides bottom topography $\mathbf{S}_0$. However, rainfall and flow resistance are relevant parameters when modelling pavement surface runoff. In the subsequent sections, the corresponding source terms are presented.

3.2. Source Terms

3.2.1. Rainfall

Rainfall is considered as a positive source term $\mathbf{Q_r} = q_{r(t)}$ [m/s] in the continuity equation:

$$\frac{\partial h}{\partial t} + \frac{\partial (uh)}{\partial x} + \frac{\partial (vh)}{\partial y} = q_{r(t)}. \tag{3.37}$$

The source term can also be negative if infiltration or evaporation processes are described.

3.2.2. Topography

The topography source term $\mathbf{Q_0} = gh\mathbf{S_0}$ in the Shallow Water Equations evokes from the hydrostatic pressure condition and the integration over flow depth. It represents the influence of the gravitational forces on momentum, which are caused by bottom slope. Therefore, it is a source term in the momentum equations:

$$\begin{aligned} \frac{\partial(uh)}{\partial t} + \frac{\partial(u^2h + \frac{1}{2}gh^2)}{\partial x} + \frac{\partial(uvh)}{\partial y} &= ghS_{0,x} \\ \frac{\partial(vh)}{\partial t} + \frac{\partial(uvh)}{\partial x} + \frac{\partial(v^2h + \frac{1}{2}gh^2)}{\partial y} &= ghS_{0,y} \end{aligned} \tag{3.38}$$

Bottom slope can be determined by:

$$\mathbf{S_0} = \begin{pmatrix} \partial z_b/\partial x \\ \partial z_b/\partial y \end{pmatrix}. \tag{3.39}$$

3.2.3. Flow Resistance

Flow resistance in free surface flows can be interpreted as a shear stress which counteracts gravity and retards the flow. Therefore, it affects water depth and it is crucial to be represented adequately. Depending on the application, flow resistance is a combination of surface or bottom resistance, shape resistance, wave resistance, resistance associated with unsteadiness of flow, rain resistance or wind resistance [2, 34, 68, 112]. Bottom resistance shall be considered exclusively herein. Bottom and shape resistance can only be modelled exactly by Direct Numerical Simulation (DNS)[81]. This is computationally intensive and not possible for highly heterogeneous surface textures like pavement surfaces. As a consequence, empirical based resistance laws are commonly used.

Flow resistance in the Shallow Water Equations can be viewed as a nonlinear sink of momentum and is therefore treated as a source term in the momentum equations. In analogy to bottom slope a friction slope $\mathbf{S_f}$ is defined. The friction slope is linked to bottom shear stress τ_b by

$$\mathbf{S_f}\, gh = \boldsymbol{\tau}_b. \tag{3.40}$$

For a two dimensional flow τ_b can be estimated empirically by

$$\tau_{b,x} = \xi\, u\, \sqrt{u^2 + v^2},\ \tau_{b,y} = \xi\, y\, \sqrt{u^2 + v^2} \tag{3.41}$$

where ξ is the empirical resistance coefficient [77]. The resistance coefficient varies with the underlying resistance equation. In the following, three well-known empirical flow resistance equations are described, which are commonly used with the

Shallow Water Equations: the Darcy-Weisbach [37], Chézy [108] and Manning equation [6, 10, 15, 18, 20, 70, 78, 77, 86, 109, 113]. A detailed review of these equations is given in [14] and [102]. In Chapter 2 pavement surface runoff was characterised as gradually varied flow. All existing flow resistance equations, however, presume uniform flow conditions.

Darcy-Weisbach

The Darcy-Weisbach equation was originally developed to describe the frictional head loss h_f for uniform and steady pipe flow depending on pipe length L, diameter D and an empirical resistance coefficient f to

$$h_f = f \frac{L}{D} \frac{\tilde{u}^2}{2g} \tag{3.42}$$

where $\tilde{u}$ is the depth averaged velocity. For laminar flow, *Hagen* and *Poiseuille* found the relationship

$$f = \frac{64}{Re}. \tag{3.43}$$

It states that the resistance coefficient decreases inversely with the Reynolds Number and that the roughness of the pipe does not explicitly influence flow resistance in the laminar flow regime.

For the turbulent flow regime, boundary layer theory, which was introduced by *Ludwig Prandtl*, provides the theoretical background for an estimation of f. This fact is significant in two ways. First, the Darcy-Weisbach resistance coefficient is the only empirical resistance coefficient which can be derived from a theoretical background. Second, boundary layer theory provides the basic equations for its determination. For this reason, the basic ideas are presented herein. For detailed information about boundary layer theory the reader is referred to [100] or [111].

At high Reynolds Numbers (fully turbulent flow), a boundary layer develops when a fluid passes a solid body. Flow resistance, which is induced between fluid and solid surface, requires the no slip condition. Therefore, flow velocity is zero at the bodies surface. This, in turn, induces a difference in velocity from free flow to zero. This velocity gradient is confined to the boundary layer. Following this definition, a turbulent flow can be divided in two parts: the boundary layer where friction dominates and an outer layer where friction can be neglected. Flow in a boundary layer can be laminar or turbulent. Transition occurs after a certain length x in flow direction and can be estimated by the critical Reynolds Number

$$Re_{crit} = (\tilde{u} x)/\nu. \tag{3.44}$$

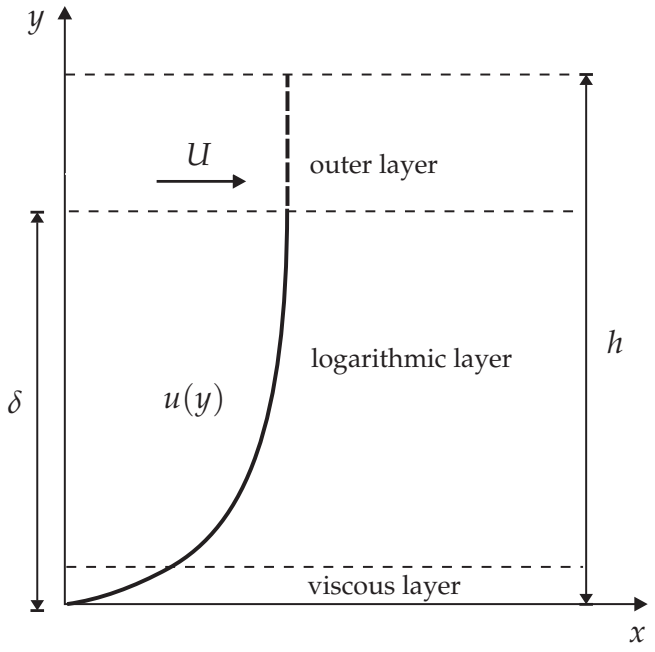

Figure 3.3.: Velocity profile for turbulent flow.

According to [100] Re_{crit} lies between $3 \cdot 10^5$ and $3 \cdot 10^6$ such that for pipe or open channel flow where flow paths are long, the turbulent boundary layer prevails. Figure 3.3 shows a velocity profile with a turbulent boundary layer. Besides the frictionless outer layer with free flow velocity U, two additional layers can be defined which both belong to the boundary layer. Close to the solid boundary, a very thin viscous sublayer develops. In this layer flow velocity is only influenced by fluid viscosity and the velocity gradient in this layer can assumed to be linear. The second layer connects the viscous sublayer and the outer turbulent layer. In the outer layer friction is independent of viscosity and only influenced by turbulent shear stresses. The velocity profile of the connecting layer can be derived with the mixing length theory as proposed by *Prandtl*, for example described in [1] or [34]. It states that the turbulent shear stresses τ_t is proportional to the square of the mixing length l^2 and the velocity gradient $(du/dy)^2$:

$$\tau_{\text{t}} = \rho \, l^2 \left(\frac{du}{dy} \right)^2. \tag{3.45}$$

At the solid boundary, τ_{t} equals the wall shear stress τ_{w}, which is defined by friction velocity

$$u_* = \sqrt{\frac{\tau_{\text{w}}}{\varrho}}. \tag{3.46}$$

It is assumed that mixing length varies linearly with distance y to the boundary and the dimensionless *von Kármán* constant κ. Applying the boundary condition for the

shear stresses $\tau_t(y = 0) = \tau_w$ (Equation (3.45)) and integrating the result yields

$$\frac{u(y)}{u^*} = \frac{1}{\kappa}\, ln(y) + C. \tag{3.47}$$

The integration constant C depends on the conditions at the solid boundary and is used to connect the velocity profile of the viscous sublayer to the logarithmic profile. *Nikuradse* did extensive experiments in rough pipes [89]. Roughness was artificially generated by sand grains of equal size which were glued to the pipe wall. The roughness parameter defined is equivalent sand grain roughness already mentioned in Section 2.1.4. Depending on k_s *Nikuradse* formulated an universal law for the velocity profile, which is valid for smooth and rough surfaces

$$\frac{u(y)}{u^*} = \frac{1}{\kappa}\, ln\left(\frac{y}{k_s}\right) + C(Re^*) \tag{3.48}$$

with $Re^* = (u^* k_s)/\nu$ as the grain Reynolds Number. Depending on Re^*, three different flow regimes are defined [34]:

- $Re^* < 5$: hydraulically smooth flow
- $5 \leq Re^* \leq 70$: transition
- $Re^* > 70$: hydraulically rough flow.

In hydraulically smooth flow, the viscous sublayer exceeds the roughness heights whereas in hydraulically rough flow, the viscous sublayer is well below the roughness heights.

According to [111], the logarithmic layer approximates almost the entire velocity profile whereas the viscous layer only extends over about 2 percent of the profile and therefore can be neglected. For this reason the logarithmic approach is sufficient to solve most of turbulent flow problems in pipes. Considering a uniform pipe flow problem, head loss can be expressed in terms of the wall shear stress τ_w by means of a momentum balance in flow direction as

$$h_f = \frac{4\tau_w L}{\varrho g d}. \tag{3.49}$$

Equating 3.49 and 3.42 yields

$$f = \frac{8\tau_w}{\varrho \tilde{u}^2}. \tag{3.50}$$

Combining this with the definition of the friction velocity (Equation (3.46)) results in

$$\frac{\tilde{u}}{u^*} = \left(\frac{8}{f}\right)^{1/2} \tag{3.51}$$

where $\tilde{u}$ represents the average velocity in the boundary layer which can be determined by integrating eq. 3.48. With this formulation the velocity distribution in the boundary layer can readily be used to give an estimation for f.

Several equations were developed to estimate f for turbulent flow in smooth and rough pipes. Using the concept of hydraulic radius r_h, the approach can also adapted to open-channel flow. Here, friction velocity can be expressed as

$$u_* = \sqrt{g r_\mathrm{h} S_0}. \tag{3.52}$$

Setting $r_\mathrm{h} = h$ in Equation (3.52) and assuming steady state $S_0 = S_\mathrm{f}$, Equation (3.51) yields the expression for S_f in one dimension

$$S_\mathrm{f} = f \frac{\tilde{u}^2}{8gh}. \tag{3.53}$$

In two dimensions, friction slope can be formulated following Equations (3.40) and (3.41) as:

$$S_{\mathrm{f,x}} = f \frac{u\sqrt{u^2+v^2}}{8gh} \quad \text{and} \quad S_{\mathrm{f,y}} = f \frac{v\sqrt{u^2+v^2}}{8gh}. \tag{3.54}$$

Two dimensional flow is depth-averaged. Therefore, the velocity components u and v correspond to the depth-averaged velocities $\tilde{u}$ and $\tilde{v}$.

Chézy

Antoine Chézy proposed an equation for flow resistance in open-channels which is

$$u = C\sqrt{r_\mathrm{h} S_\mathrm{f}} \tag{3.55}$$

where r_h is the hydraulic radius and C the Chézy resistance coefficient. If the hydraulic radius for pipe flow $r_\mathrm{h} = D/4$ is inserted into the Chézy equation and S_f is substituted by h_f/L, the comparison with the Darcy-Weisbach equation yields

$$C = \frac{\sqrt{8g}}{f}. \tag{3.56}$$

In consequence, Chézy's coefficient can be directly linked to the Darcy-Weisbach coefficient. Many attempts have been made to find an adequate estimation for C. These attempts were not successful since C depends on a variety of parameters besides roughness [26]. According to [102] approaching C with the Darcy-Weisbach friction coefficient f seems to be the most sound. However, experiments, which yielded the Chézy equation were done in large channels with shallow flow conditions and high relative roughness. That is why [84] suggests an approximation with

the resistance coefficient resulting from Manning's equation (Equation (3.58)), which is presented in the next paragraph. In the context of the Shallow Water Equations the Chézy equation is written as

$$S_{f,x} = \frac{u\sqrt{u^2+v^2}}{C^2 h} \quad \text{and} \quad S_{f,y} = \frac{v\sqrt{u^2+v^2}}{C^2 h}. \tag{3.57}$$

Manning

Experiments performed by *Manning* showed that C is proportional to the sixth root of the hydraulic radius $C \sim r_h^{1/6}$. Introducing a proportionality factor n, Chézy's equation (3.55) can be written as

$$V = \frac{1}{n}\, r^{2/3}\, \sqrt{S_f}, \tag{3.58}$$

which is known as Manning's equation. Estimation of n is strictly empirical. Mannings's n values are published in tables, which can be found in the basic hydraulic literature e.g. in [27]. The formulation of the friction slopes for the Shallow Water Equations using the Manning equation is:

$$S_{f,x} = n^2\, \frac{u\sqrt{u^2+v^2}}{h^{4/3}} \quad \text{and} \quad S_{f,y} = n^2\, \frac{v\sqrt{u^2+v^2}}{h^{4/3}}. \tag{3.59}$$

In open-channel and overland flow, the Darcy-Weisbach, Manning as well as the Chézy equation is used. However, each equation inherits advantages and disadvantages which should be kept in mind when applying them. The advantage of the Darcy-Weisbach equation is the fact that f is a dimensionless parameter and that the equation is able to cover the entire flow regime from laminar to turbulent. A disadvantage is the absence of ready f-values. They have to be determined either from the Moody diagram, by fitting a velocity profile or by directly fitting f to experimental data. For Manning's equation many published n-values exist. Disadvantages are that first, these values are mainly based on experiments in rough channels with high Reynolds Numbers. The use of Manning's equation should therefore be limited to these flow regimes [8, 49, 62, 66] and [87]. Second, Manning's equation is only applicable for relative roughness values of $100 < h/k < 10.000$ [102]. For pavement surface runoff, h/k lies between 1.0 and 15, approximately. Therefore, the application to pavement surface runoff seems questionable. As already presented, the Chézy coefficient always depends on f- or n-values, respectively. Therefore, Chézy is also not considered further.

Inserting specified source terms, the Shallow Water Equations used in this work can be formulated as follows:

$$\frac{\partial}{\partial t}\begin{pmatrix} h \\ uh \\ vh \end{pmatrix} + \frac{\partial}{\partial x}\begin{pmatrix} uh \\ u^2h + \frac{1}{2}gh^2 \\ uvh \end{pmatrix} + \frac{\partial}{\partial y}\begin{pmatrix} vh \\ uvh \\ v^2h + \frac{1}{2}gh^2 \end{pmatrix} = \begin{pmatrix} q_\mathrm{r} \\ ghS_{0,\mathrm{x}} - ghS_{\mathrm{f,x}} \\ ghS_{0,\mathrm{y}} - ghS_{\mathrm{f,y}} \end{pmatrix}. \quad (3.60)$$

3.3. Mathematical Characterisation

The Shallow Water Equation constitutes a system of partial differential equations. Partial differential equations can be characterised as parabolic, elliptic or hyperbolic. Depending on the type of the equation, different physical phenomena are described. Elliptic equations for example describe time-independent equilibrium states in fluid and structural mechanics as well as diffusion dominated thermodynamic processes. The Shallow Water Equation consists of hyperbolic partial differential equations. Hyperbolic equations describe wave propagation phenomena as well as transport processes which are convection dominated. The subsequent sections deal with the properties of hyperbolic partial differential equations because they strongly influence the numerical method used.

An extensive mathematical motivated overview of hyperbolic partial differential equations is given in [29], an overview of hyperbolic partial differential equations with focus on appropriate numerical methods can be found in [47] and [74]. For supplementary reading about the characterisation of partial differential equations in general the reader is referred to [9, 58] and [85].

3.3.1. Hyperbolic Partial Differential Equations

A homogeneous system of m partial differential equations in two space dimensions is defined by

$$\frac{\partial \mathbf{U}}{\partial t} + \frac{\partial \mathbf{F}(\mathbf{U})}{\partial x} + \frac{\partial \mathbf{F}(\mathbf{U})}{\partial y} = 0 \quad (3.61)$$

where $\mathbf{U}$ denotes the vector of conserved variables and $\mathbf{F}$ the numerical flux tensor. In the Shallow Water Equations, these terms correspond to

$$\mathbf{U} = \begin{pmatrix} h \\ uh \\ vh \end{pmatrix} \qquad \mathbf{F} = \begin{pmatrix} uh & vh \\ u^2h + \frac{1}{2}gh^2 & uvh \\ uvh & v^2h + \frac{1}{2}gh^2 \end{pmatrix}. \quad (3.62)$$

As can be seen from the flux tensor, the system is non-linear. Equation (3.61) is known as the conservative form of a partial differential equation. Using the Jacobians, which are defined by

$$\mathbf{J_x}(\mathbf{U}) = \frac{\partial(\mathbf{F}\cdot\mathbf{n}_\mathrm{x})}{\partial\mathbf{U}}, \qquad \mathbf{J_y}(\mathbf{U}) = \frac{\partial(\mathbf{F}\cdot\mathbf{n}_\mathrm{x})}{\partial\mathbf{U}} \tag{3.63}$$

the non-linear system can be transformed into its quasi-linear form

$$\frac{\partial\mathbf{U}}{\partial t} + \mathbf{J_x}(\mathbf{U})\frac{\partial\mathbf{U}}{\partial x} + \mathbf{J_y}(\mathbf{U})\frac{\partial\mathbf{U}}{\partial y} = 0. \tag{3.64}$$

The quasi-linear form of a partial differential equation also determines whether it is elliptic, parabolic or hyperbolic. A system of partial differential equations is said to be hyperbolic if the Jacobian has m real eigenvalues and m linearly independent right eigenvectors. For the Shallow Water Equations, the Jacobians are [4]:

$$\mathbf{J_x} = \begin{pmatrix} 0 & 1 & 0 \\ -u^2+c^2 & 2u & 0 \\ -uv & v & u \end{pmatrix}, \qquad \mathbf{J_y} = \begin{pmatrix} 0 & 0 & 1 \\ -uv & v & u \\ -v^2+c^2 & 0 & 2v \end{pmatrix} \tag{3.65}$$

and the respective eigenvalues are:

$$\begin{aligned} \lambda_{\mathrm{w,1,x}} &= u+c,\ \lambda_{\mathrm{w,2,x}} = u,\ \lambda_{\mathrm{w,3,x}} = u-c \\ \lambda_{\mathrm{w,1,y}} &= v+c,\ \lambda_{\mathrm{w,2,y}} = v,\ \lambda_{\mathrm{w,3,y}} = v-c \end{aligned} \tag{3.66}$$

where $c = \sqrt{gh}$ is the celerity of gravity waves. Consequently, the Shallow Water Equations consist of hyperbolic partial differential equations.

Hyperbolic partial differential equations describe propagation phenomena. Physically, the eigenvalues represent the speeds of information propagation. Information always travels along the characteristic curves. That is why the eigenvalues are often referred to as characteristic speeds. Characteristic curves can be defined as curves in the time-space plane along which the solution remains constant. In linear hyperbolic equations, characteristic curves always run parallel and the characteristic speed is constant. In non-linear hyperbolic equations, such as the Shallow Water Equations, characteristic speed depends on the flow variables. Consequently, characteristic curves are not parallel. They can rather merge, diverge or cross. In the latter case, the solution becomes discontinuous giving raise to shock formation. The fact that a discontinuous solution can occur within a continuous equation, even for smooth initial data, is special for hyperbolic partial differential equations. It requires solution strategies which are able to correctly describe and preserve the discontinuities. A helpful tool for the development of adequate solution strategies is the Riemann Problem, which is presented in the following section.

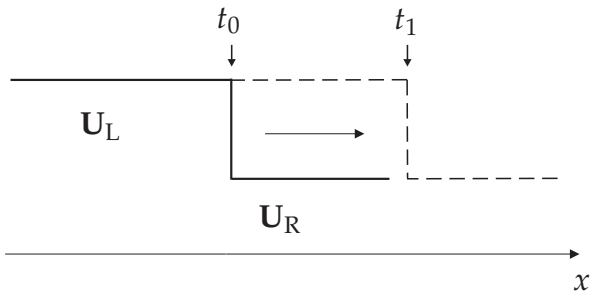

Figure 3.4.: Position of the discontinuity of a Riemann Problem for a linear, scalar equation at times t_0 and t_1.

3.3.2. Riemann Problem

A Riemann Problem is defined as an initial value problem for a partial differential equation with initially piecewise constant data separated by a single jump discontinuity as shown in Figure 3.3.2. The initial states, expressed by the conserved variables to the left and right of the discontinuity are denoted with the subscripts L respectively R. With time, the discontinuity will move along the characteristic curves with characteristic speed. Physically, this can be interpreted as a wave propagation. In this chapter, a characteristic curve carrying a discontinuity with characteristic speed is referred to as wave. Depending on the type of equation, the number and type of waves differ as shown in Figure 3.5. Scalar equations, for example, only exhibit one wave whereas a system of m equations exhibits m waves. The solution to the Riemann Problem aims to define the wave structure to find the solution for the conserved variables within the wave structure. A short overview of the different solution strategies shall be given herein because it substantially affects the flux approximation in the numerical method (see Chapter 4). The solution strategy for the Riemann problem and its complexity also vary with the underlying type of partial differential equation (linear, non-linear, scalar or system). A detailed description can be found in [74] and [105].

For linear partial differential equations, whether scalar or system, the characteristic speeds are constant and the characteristic curves run parallel. In a linear scalar partial differential equation, there is only one wave travelling at constant speed λ_w. The corresponding characteristic curve is shown in Figure 3.5a. There are two possible solutions to the Riemann Problem, either u_L or u_R. For a linear system of partial differential equations with m equations there are m waves as shown in Figure 3.5b. The solution at the leftmost and rightmost side corresponds to the states $\mathbf{U}_\mathrm{R}$ and $\mathbf{U}_\mathrm{L}$. The solution in the wedge between the $\lambda_{\mathrm{w},1}$ and $\lambda_{\mathrm{w,m}}$ wave can be found by a superposition of the waves.

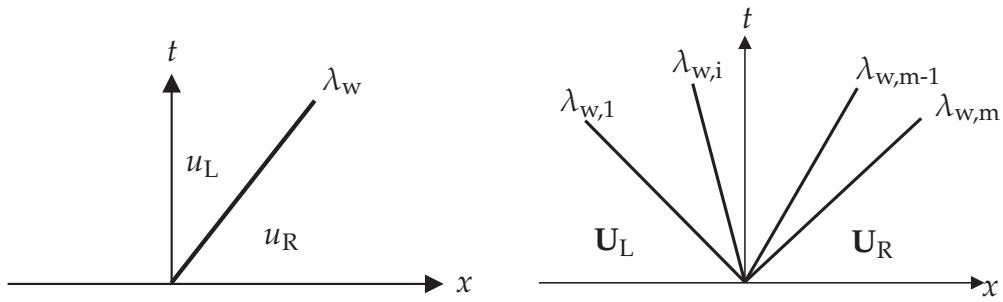

(a) Linear Scalar PDE (b) Linear System of PDEs

Figure 3.5.: Wave structure of the Riemann Problem for linear PDEs.

In non-linear partial differential equations the characteristic speeds are not constant but depend on the conserved variables and consequently $\lambda_w = \lambda_w(u)$. This can be verified when looking at the eigenvalues of the Shallow Water Equations (Equation (3.66)). The dependency on the conserved variables results in a deformation of the waves. The deformation can either be a compression or rarefaction. In a non-linear scalar partial differential equation of the form

$$u_t + f(u)_x = 0 \tag{3.67}$$

the flux function $f(u)$ strongly influences whether a wave has compressive or expansive character. The characteristic speed is given by $f'(u) = \lambda_w(u)$. The behaviour of $\lambda_w(u)$ reveals information about the character when looking at the criterion of monotonicity. Three possible cases are distinguished:

- convex flux: $\lambda(u)$ is a monotone increasing function: For increasing values of u, $\lambda_w(u)$ is also increasing.
- concave flux: $\lambda(u)$ is a monotone decreasing function: For increasing values of u, $\lambda_w(u)$ is decreasing.
- non-convex, non-concave flux: $\lambda_w(u)$ shows extrema.

Figure 3.6 illustrates the difference of convex and concave flux. In the uppermost figure, the initial conditions u_0^i with $i = 1\text{to}7$ are plotted. The two plots below show the corresponding characteristic curves for a convex respectively concave flux. It is obvious that in case of a convex flux, there is a rarefaction in direction of increasing u whereas for decreasing u a compression forms. For the concave flux, the situation is reversed. High magnitudes of u provoke a compression whereas decreasing u produces an expansion respectively rarefaction. An example for concave flux is the traffic flow equation.

There are three solutions to a non-linear Riemann Problem: rarefaction waves, shock waves and contact discontinuities. A contact discontinuity develops when the flow

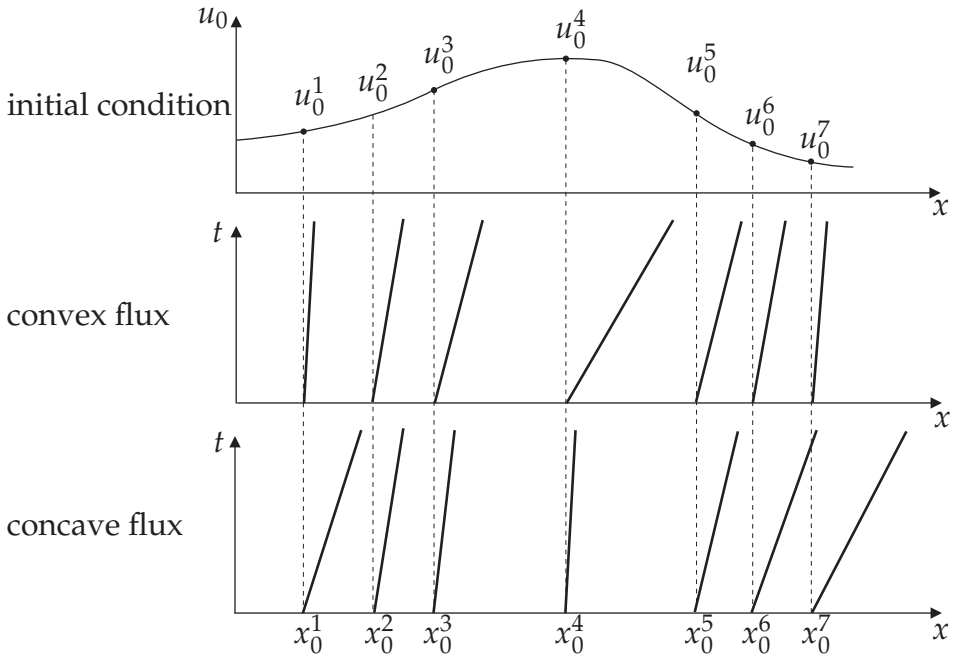

Figure 3.6.: Characteristics of a concave and convex flux.

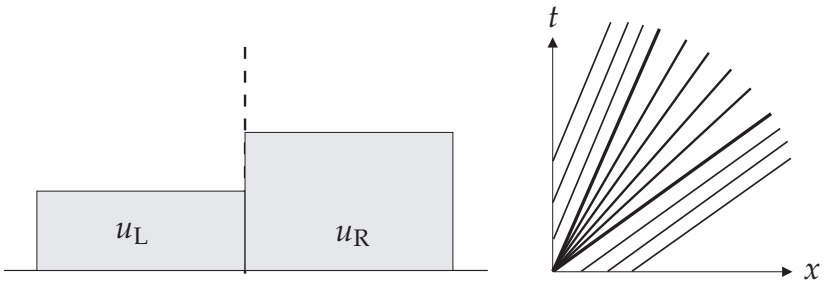

Figure 3.7.: Initial value problem and characteristic curves of a rarefaction wave for convex flux.

variables such as velocity and water depth are continuous and discontinuities occur in density or temperature. Since water is an incompressible fluid and temperature is neglected in this application, contact discontinuities are not further discussed here.

Rarefaction waves occur if the initial value problem shown in Figure 3.7 is considered in connection with a non-linear scalar equation. If convex flux is assumed, the characteristic speed on the left side of the interface is smaller than on the right. The characteristic curves expand and the solution is continuous.

In case of a shock wave, the initial values are switched (see figure 3.8). Consequently, the characteristic speed on the left side is higher than on the right side. Assuming convex flow, characteristics cross and the solution gets discontinuous. The speed of the shock wave can be determined by imposing an integral conservation condition

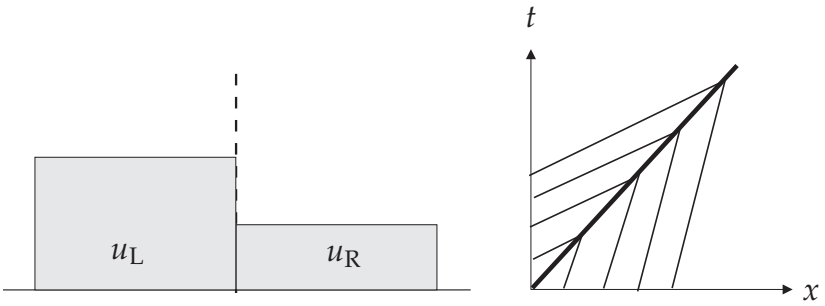

Figure 3.8.: Initial value problem and characteristic curves of a shock wave for convex flux.

on the jump, which is known as the Rankine Hugoniot Condition [74]:

$$s = \frac{f(u_R) - f(u_L)}{u_R - u_L} \tag{3.68}$$

with s denoting the shock speed. Knowing the shock speed, the solution of the Riemann Problem is defined by

$$u(x,t) = \begin{cases} u_L & x < s \cdot t \\ u_R & x > s \cdot t. \end{cases} \tag{3.69}$$

Sometimes there exist several solutions to the shock speed. To pick the unique and physically correct solution a second condition has to be imposed, which is known as Entropy Condition. A shock travelling with speed s satisfies the entropy condition if

$$\lambda_w(u_L) > s > \lambda_w(u_R). \tag{3.70}$$

It could be demonstrated that for a scalar non-linear equation the discontinuous solution to a Riemann Problem can be determined quite easily. For non-linear systems of partial differential equations the situation is more complex. There are m families of characteristics which are all parametrised over the conserved variables. If the Rankine-Hugoniot Condition is expanded to systems of equations, $\mathbf{f}$ and $\mathbf{u}$ are vectors and there are $m+1$ different states. Not every combination of vectors allows to solve for the shock speed s and additional conditions have to be imposed. Only if the vectors are linearly dependent, s can be determined holding the Rankine Hugoniot condition. That is the case, if $\mathbf{u}$ consists of eigenvectors of the linearised coefficient matrix and s the associated eigenvalue [73]. It is evident that the strategy to develop an analytical solution for these Riemann Problems is very complex. For detailed information the reader is referred to [73] and [74]. For practical purposes, approximate Riemann solvers have been developed. They do not consider the full wave structure of a Riemann problem but assume a simplified wave structure. Two of them are presented in Chapter 4.

Summarising, the mathematical model for the description of pavement surface runoff was set up in this chapter. Starting from the most general form of a conservation law, the depth-averaged Shallow Water Equations were derived from the Navier-Stokes Equations applying several assumptions and simplifications, which were discussed in Chapter 2. The Shallow Water Equations were completed by source terms to describe the relevant factors influencing pavement surface runoff: rainfall, bottom topography and flow resistance. Next, the Shallow Water Equations were characterised mathematically. They constitute a hyperbolic system of non-linear partial differential equations. Physically, these equations describe wave propagation phenomena. Special to hyperbolic equations is the possible occurrence of discontinuous solutions within the continuous equations. Finally, the Riemann problem was shortly discussed. It provides strategies for a consistent solution in the presence of discontinuities. This especially affects the discretisation of the mathematical model, which is presented in the following chapter.

4. Discretisation

In the preceeding chapter the mathematical model for a description of pavement surface runoff, namely the depth-averaged Shallow Water Equations with specific source terms, was derived. It is a system of three non-linear partial differential equations, which can not be solved analytically. Therefore, numerical methods are applied, which solve the discretised equations numerically. Discretisation is the process of expressing the general flow laws written for a continuous medium in terms of discrete values at a finite number of points in time as well in space. As discussed in section 3.3, the Shallow Water Equations are hyperbolic. Hyperbolic equations have strong directional properties and although they are formulated continuously, they allow discontinuous solutions. This has to be preserved when discretising the equations. Several methods exist to discretise and solve partial differential equations. Most common are the Finite Difference (FDM), Finite Element (FEM), Finite Volume (FVM) and Discontinuous Galerkin (DG) methods. For the discretisation of the Shallow Water Equations the Finite Volume Method is used. It is the standard discretisation method in fluid dynamics and is advantageous in several ways. First, there is a variety of methods available. Second, according to [114] it is usually less time consuming than other methods. Third, it is based on the integral form of the conservation law as will be explained in the subsequent section. Thus, the discretisation itself is conservative. Fourth, the discretised equations allow locally discontinuous solutions as required by hyperbolic partial differential equations. The numerical treatment of the Shallow Water Equations and hyperbolic equations in general is covered by many publications. An extensive overview can be found in [74, 103, 105, 106] and [110]. This chapter presents the finite volume discretisation of the Shallow Water Equations including its source terms. One focus is on the approximation of the intercell numerical fluxes using approximate Riemann solvers.

4.1. Finite Volume Discretisation

The finite volume discretisation is an approximation of the integral conservation law

$$\int_{\partial V} \frac{\mathbf{U}}{\partial t}\, dV + \int_{\partial A} \mathbf{F} \cdot \mathbf{n}\, dA = \int_{\partial V} \mathbf{Q}\, dV \tag{4.1}$$

where

$$\mathbf{U} = \begin{pmatrix} h \\ uh \\ vh \end{pmatrix} \qquad \mathbf{F} = \begin{pmatrix} uh & vh \\ u^2h + \frac{1}{2}gh^2 & uvh \\ uvh & v^2h + \frac{1}{2}gh^2 \end{pmatrix} \qquad \mathbf{Q} = \begin{pmatrix} q_\mathrm{r} \\ ghS_{0,\mathrm{x}} - ghS_{\mathrm{f,x}} \\ ghS_{0,\mathrm{y}} - ghS_{\mathrm{f,y}} \end{pmatrix}. \tag{4.2}$$

Space discretisation is done by transferring the continuous model domain into a grid consisting of a finite number of grid points. Finite volume methods can generally be applied to structured and unstructured grids. Since data handling and discretisation are easier for structured grids, a cartesian grid is used in this work. The underlying two dimensional grid is shown in Figure 4.1. Note that in a two dimensional grid the volume V of a grid cell is reduced to its area and $V = \Delta x \cdot \Delta y$. If $\Delta x = \Delta y$ the grid is called equidistant. The conserved variables are stored at the centre of each grid cell as cell-averaged values.

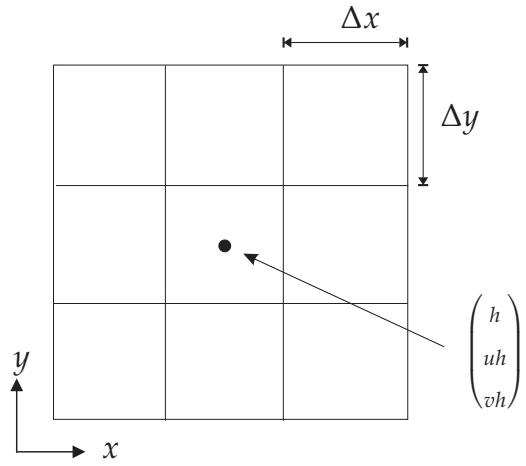

Figure 4.1.: Cell-centred finite volume discretisation on a cartesian grid.

Time discretisation is done with an explicit first order time step method. If the integral conservation equation (Equation (4.1)) is discretised in space and time as described before, the resulting finite volume scheme for the update of the conserved variables reads:

$$\mathbf{U}^{t+1} = \mathbf{U}^t + \frac{\Delta t}{\Delta V} \sum_{r=1}^{4} (\mathbf{F} \cdot \mathbf{n}_r)\, A_r + \Delta t \mathbf{Q}. \tag{4.3}$$

The update equation states that the new set of conserved variables at time $t + 1$ is determined on the basis of the state at time t and the change of conserved variables during the time step due to the flux and source term. The net flux of each grid cell is calculated as the sum of the fluxes $\mathbf{F}$ across the four interfaces $r = 1, 2, 3, 4$ with length A_r in direction of the normal vector $\mathbf{n}_r$. The source terms are not evaluated

at the interfaces but for the grid cell. Before the evaluation of the source term **Q** is presented, the approximation of the intercell flux is discussed.

4.2. Flux Approximation

The objective of flux approximation is to give a reasonable well estimation of the flux between two cells on the basis of the cell averaged values. For the computation of the intercell flux the conserved variables at the interface have to be determined. This is done using central or upwind methods.

A central method determines the conserved variables independently of the direction of information propagation. At the interface, the values of the two neighbouring cells are simply averaged and then used for flux calculation. This symmetric method is suitable for problems with diffusive character. However, the Shallow Water Equations have strong directional properties due to their hyperbolic character. As presented in Section 3.3 information is carried through the domain along the characteristics. Therefore, the direction of information propagation and the number of waves carrying the information has to be considered when determining the conserved variables at the interface. This is done with so-called upwind methods. The simplest upwind method is the first oder upwind method. It is a purely one sided method considering only one direction of information propagation, thus only one wave. In systems of partial differential equations at least two waves occur and therefore a one-sided method is not sufficient. The determination of the conserved variables at the interface within a wave structure corresponds to solving a Riemann Problem as discussed in Section 3.3.2. An upwind method which includes the solution to the Riemann Problem into the flux approximation is the method of *Godunov*.

Figure 4.2 shows a one dimensional grid with three grid cells $i-1, i$ and $i+1$. The conserved variables are cell averaged values. As a consequence, jump discontinuities develop at the interfaces $i-1/2$ and $i+1/2$.

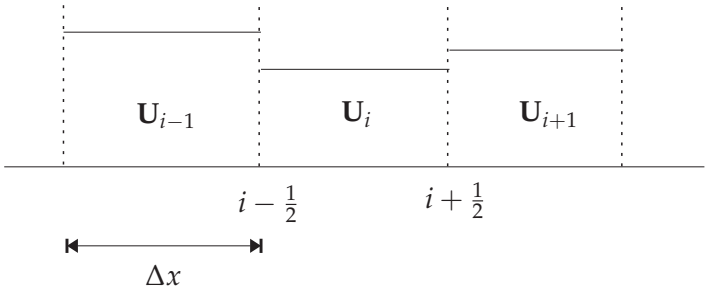

Figure 4.2.: Discontinuities at the cell interfaces due to volume averaging.

To compute the intercell fluxes $\mathbf{F}_{i-1/2}$ and $\mathbf{F}_{i+1/2}$, the conserved variables around the interface have to be determined by solving a Riemann Problem. Figure 4.3 shows the Riemann Problems at the interfaces and the emanating characteristics between times t and $t+1$. The dashed lines represent the interfaces and the solid lines represent the characteristics.

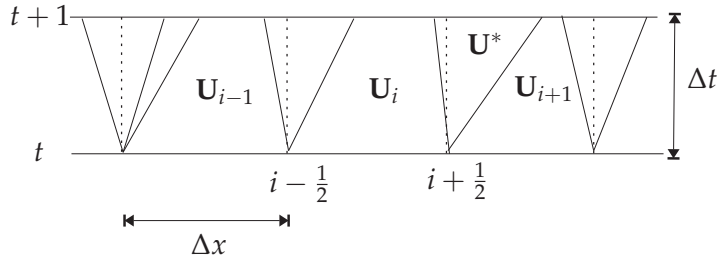

Figure 4.3.: Riemann Problems forming at the cell interfaces.

The solution of the Riemann problem between cells i and $i+1$ yields

$$\mathbf{U}^* = RP[\mathbf{U}_i^t, \mathbf{U}_{i+1}^t]. \tag{4.4}$$

Using $\mathbf{U}^*$, the intercell flux $\mathbf{F}^*$ is finally calculated as

$$\mathbf{F}^* = \mathbf{F}_{i+\frac{1}{2}}(\mathbf{U}_{i+\frac{1}{2}}^*). \tag{4.5}$$

In general, the Godunov intercell numerical flux is defined as

$$\mathbf{F}_{i+\frac{1}{2}} = \mathbf{F}^*(\mathbf{U}_i^t, \mathbf{U}_{i+1}^t). \tag{4.6}$$

An important restriction for the method in combination with an explicit time discretisation is that the waves emanating from an interface must not travel beyond the cell within a time step. Consequently, the time step size has to be restricted. This restriction is commonly known as the Courant Friedrichs Lewy (CFL) restriction. The restricted time step size is determined depending on the biggest wave celerity λ_{max} as

$$\Delta t_{\text{CFL}} = \frac{\Delta x}{|\lambda_{\max}|}. \tag{4.7}$$

According to Section 3.3.1, wave celerities are the eigenvalues of the Jacobian matrices. For the Shallow Water Equations the eigenvalues are given in Equation 3.66 and the CFL restriction in one dimension is defined as:

$$\Delta t_{\text{CFL}} = \frac{\Delta x}{\max(\left|u - \sqrt{gh}\right|, \left|u + \sqrt{gh}\right|)}. \tag{4.8}$$

Godunov's method has first order accuracy in time and space. The method has the important property that it respects the entropy condition (see Section 3.3.2) which guarantees a physically meaningful solution. Further information about Godunov's method can be found in [36, 53] and [105].

4.2.1. Approximate Riemann Solvers

The analytical solution to the Riemann Problem considers the complete characteristic wave structure. Therefore, Godunov's method is a 'natural upwinding' method. However, solving the Riemann Problem analytically for non-linear systems of equations is an iterative process and computationally expensive. Thus, approximate Riemann solvers were developed and combined with the Godunov method. A good overview and extensive description of various approximate Riemann solvers is given in [74] and [105]. The solvers mostly used for solving the Shallow Water Equations are the Roe solver [12, 15, 21, 45, 70], the HLL solver [20, 51, 108, 113, 115] and the HLLC solver [65, 77]. All three solvers are Godunov type methods. Other approximate Riemann solvers besides the Godunov type methods are the Osher Scheme and the Flux Vector Splitting Methods. The Osher scheme is used to solve the Shallow Water Equations in combination with a finite volume method in [106]. A well-known Flux Vector Splitting Method is the method of Steeger Warming used in [114]. A comparison of the various approximate Riemann solvers with an application to the depth-averaged Shallow Water Equations is given in [114].

Approximate Riemann solvers do not consider the full wave structure. Instead, they assume a simplified wave structure for the Riemann Problem. The solvers differ in the number of waves considered. The HLL solver developed by *Harten* [53] is the most simple and assumes a two wave structure, which considers the fastest wave in each direction. If the wave speeds are estimated according to *Einfeldt* [36], the HLL solver is also known as HLLE. The HLLC solver [107] considers a three wave structure with an additional wave travelling at intermediate speed. Roe's solver [96] considers the full wave structure but it approximates the solution to the Riemann Problem by exactly solving for the linearised equation (see Equation (3.64)). This is much more time efficient than solving the non-linear system.

It is evident that the quality of the flux approximation and the shock capturing properties increase with the number of waves considered. Good shock capturing properties and a high resolution of the shock wave are for example needed in dam break or tsunami simulations to determine the exact position and shape of the shock front. In pavement surface runoff modelling the description of shock fronts on a local scale is irrelevant. It rather focuses on the description of the global water depth distribution. For this reason, the HLL solver is considered sufficient. In the model, both, the HLL and HLLC solver are implemented. In the following sections, the latter is only shortly described. Both solvers are compared by a numerical experiment.

HLL Solver

The HLL solver assumes a two wave structure for the Riemann Problem with the fastest waves in each direction as shown in Figure 4.4. The wave speeds are S_L

and S_R for the directions left respectively right form the interface. The two wave structure separates three states of the conserved variables. The states $\mathbf{U}_L$ and $\mathbf{U}_R$ at time t and the state developing around the interface during the time step $\mathbf{U}_{HLL}$.

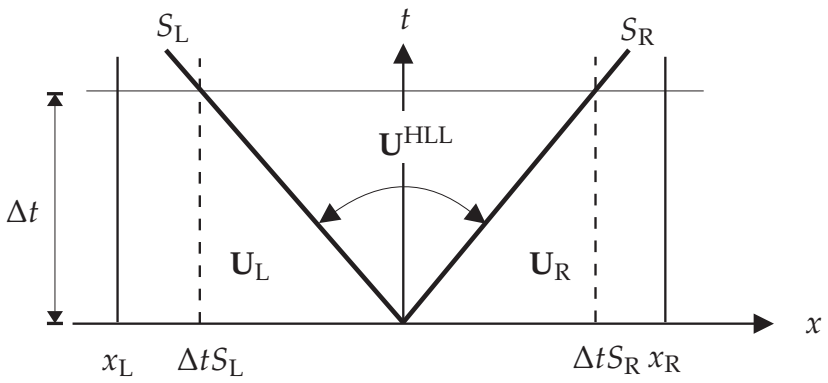

Figure 4.4.: Wave Structure assumed for the HLL solver within a control volume $[x_L, x_R]$.

For the derivation of the HLL solver, a control volume around the cell interface is considered. For a given time step Δt, the control volume exceeds the distance travelled by the two waves. The CFL restriction is thus fulfilled. The borders of the control volume are defined as

$$x_\mathrm{L} \leq \Delta t S_\mathrm{L} \text{ and } x_\mathrm{R} \geq \Delta t S_\mathrm{R}. \tag{4.9}$$

The integral form of the conservation law for the control volume can be expressed as

$$\int_{x_\mathrm{L}}^{x_\mathrm{R}} \mathbf{U}(x, t_0 + \Delta t)\, dx = \int_{x_\mathrm{L}}^{x_\mathrm{R}} \mathbf{U}(x, t_0)\, dx + \int_{t_0}^{t_0+\Delta t} \mathbf{F}(\mathbf{U}(x_\mathrm{L}, t))\, dt - \int_{t_0}^{t_0+\Delta t} \mathbf{F}(\mathbf{U}(x_\mathrm{R}, t))\, dt. \tag{4.10}$$

The new solution $\mathbf{U}$ at time $t_0 + \Delta t$ depends on the old solution at time t and the fluxes $\mathbf{F}_\mathrm{L}$ and $\mathbf{F}_\mathrm{R}$ through the boundaries at x_L and x_R during the time step. The evaluation of the right side of Equation (4.10) yields:

$$\int_{x_\mathrm{L}}^{x_\mathrm{R}} \mathbf{U}(x, t_0 + \Delta t)\, dx = x_\mathrm{R}\mathbf{U}_\mathrm{R} - x_\mathrm{L}\mathbf{U}_\mathrm{L} + \Delta t(\mathbf{F}_\mathrm{L} - \mathbf{F}_\mathrm{R}). \tag{4.11}$$

The left part of Equation (4.11) can be splitted into the three states defined before:

$$\int_{x_\mathrm{L}}^{x_\mathrm{R}} \mathbf{U}(x, t_0 + \Delta t)\, dx = \int_{x_\mathrm{L}}^{\Delta t S_\mathrm{L}} \mathbf{U}(x, t_0 + \Delta t)\, dx + \int_{\Delta t S_\mathrm{L}}^{\Delta t S_\mathrm{R}} \mathbf{U}(x, t_0 + \Delta t)\, dx + \int_{\Delta t S_\mathrm{R}}^{x_\mathrm{L}} \mathbf{U}(x, t_0 + \Delta t)\, dx. \tag{4.12}$$

Evaluating the integrals for the left and right state yields

$$\int_{x_\mathrm{L}}^{x_\mathrm{R}} \mathbf{U}(x, t_0 + \Delta t)\, dx = \int_{\Delta t S_\mathrm{L}}^{\Delta t S_\mathrm{R}} \mathbf{U}(x, t_0 + \Delta t)\, dx + (\Delta t S_\mathrm{L} - x_\mathrm{L})\mathbf{U}_\mathrm{L} + (x_\mathrm{R} - \Delta t S_\mathrm{R})\mathbf{U}_\mathrm{R}. \tag{4.13}$$

Inserting Equation (4.11) into Equation (4.13) and solving for the integral $\Delta t S_\mathrm{L} - \Delta t S_\mathrm{R}$ gives

$$\int_{\Delta t S_\mathrm{L}}^{\Delta t S_\mathrm{R}} \mathbf{U}(x, t_0 + \Delta t)\, dx = \Delta t(S_\mathrm{R}\mathbf{U}_\mathrm{R} - S_\mathrm{L}\mathbf{U}_\mathrm{L} + \mathbf{F}_\mathrm{L} - \mathbf{F}_\mathrm{R}). \tag{4.14}$$

The width of the of wedge between the two waves can be determined to be

$$\Delta t(S_\mathrm{R} - S_\mathrm{L}). \tag{4.15}$$

Dividing Equation (4.14) by Equation (4.15) yields

$$\frac{1}{\Delta t(S_\mathrm{R} - S_\mathrm{L})} \int_{\Delta t S_\mathrm{L}}^{\Delta t S_\mathrm{R}} \mathbf{U}(x, t_0 + \Delta t)\, dx = \frac{S_\mathrm{R}\mathbf{U}_\mathrm{R} - S_\mathrm{L}\mathbf{U}_\mathrm{L} + \mathbf{F}_\mathrm{L} - \mathbf{F}_\mathrm{R}}{S_\mathrm{R} - S_\mathrm{L}}. \tag{4.16}$$

It can be seen from the equation that the average of the integral on the left side is constant if the wave speeds are known. This state corresponds to the approximate solution in the star region $\mathbf{U}^{HLL}$ as determined by the HLL solver. It is defined as

$$\mathbf{U}^\mathrm{HLL} = \frac{S_\mathrm{R}\mathbf{U}_\mathrm{R} - S_\mathrm{L}\mathbf{U}_\mathrm{L} + \mathbf{F}_\mathrm{L} - \mathbf{F}_\mathrm{R}}{S_\mathrm{R} - S_\mathrm{L}}. \tag{4.17}$$

Now that the conserved variables around the interface $\mathbf{U}_\mathrm{HLL}$ are known, the flux across the interface is estimated. Note, that $\mathbf{F}^\mathrm{HLL}$ is not simply $\mathbf{F}(\mathbf{U}^\mathrm{HLL})$ because the width of the state $\mathbf{U}^\mathrm{HLL}$ varies during the time step. To evaluate the intercell flux $\mathbf{F}^\mathrm{HLL}$ the conservation law (Equation (4.10)) is applied to the left and right side of the interface reaching from $[\Delta t S_\mathrm{L}, 0]$ and $[0, \Delta t S_\mathrm{R}]$ and $[t_0, t_0 + \Delta t]$. The fluxes across the interface at $x = 0$ are denoted with $\mathbf{F}_{0,\mathrm{L}}$ and $\mathbf{F}_{0,\mathrm{R}}$. Evaluating these integral equations according to Equation (4.14) and solving for the intercell fluxes yields

$$\begin{aligned} \mathbf{F}_{0,L} &= \mathbf{F}_L - S_L\mathbf{U}_L - \frac{1}{\Delta t} \int_{\Delta t S_L}^{0} \mathbf{U}(x, t_0 + \Delta t)\, dx \\ \mathbf{F}_{0,R} &= \mathbf{F}_R - S_R\mathbf{U}_R + \frac{1}{\Delta t} \int_{0}^{\Delta t S_R} \mathbf{U}(x, t_0 + \Delta t)\, dx. \end{aligned} \tag{4.18}$$

Consistency requires that $\mathbf{F}_{0,\mathrm{L}} = \mathbf{F}_{0,\mathrm{R}}$ and thus the fluxes can be denoted as $\mathbf{F}^{\mathrm{HLL}}$. Substitution of the integrands in Equation (4.18) by $\mathbf{U}^{\mathrm{HLL}}$ gives

$$\begin{aligned} \mathbf{F}^{\mathrm{HLL}} &= \mathbf{F}_{\mathrm{L}} + S_{\mathrm{L}}(\mathbf{U}^{\mathrm{HLL}} - \mathbf{U}_{\mathrm{L}}) \\ \mathbf{F}^{\mathrm{HLL}} &= \mathbf{F}_{\mathrm{R}} + S_{\mathrm{R}}(\mathbf{U}^{\mathrm{HLL}} - \mathbf{U}_{\mathrm{R}}). \end{aligned} \tag{4.19}$$

This is equal to applying Rankine-Hugoniot jump condition at the interface (see Equation (3.68). Inserting Equation ((4.17)) yields

$$\mathbf{F}^{\mathrm{HLL}} = \frac{S_{\mathrm{R}}\mathbf{F}_{\mathrm{L}} - S_{\mathrm{L}}\mathbf{F}_{\mathrm{R}} + S_{\mathrm{L}}S_{\mathrm{R}}(\mathbf{U}_{\mathrm{R}} - \mathbf{U}_{\mathrm{L}})}{S_{\mathrm{R}} - S_{\mathrm{L}}} \tag{4.20}$$

and it can be seen from the equation that the intercell flux is only depending on the left and right state variables and the wave speeds. Within a Godunov type method, the intercell flux can be defined as follows:

$$\mathbf{F}^{\mathrm{HLL}}_{i+\frac{1}{2}} = \begin{cases} \mathbf{F}_{\mathrm{L}} & \text{if } S_{\mathrm{L}} \geq 0 \\ \frac{S_{\mathrm{R}}\mathbf{F}_{\mathrm{L}} - S_{\mathrm{L}}\mathbf{F}_{\mathrm{R}} + S_{\mathrm{L}}S_{\mathrm{R}}(\mathbf{U}_{\mathrm{R}} - \mathbf{U}_{\mathrm{L}})}{S_{\mathrm{R}} - S_{\mathrm{L}}} & \text{if } S_{\mathrm{L}} \leq 0 \leq S_{\mathrm{R}} \\ \mathbf{F}_{\mathrm{R}} & \text{if } S_{\mathrm{R}} \leq 0 \end{cases} \tag{4.21}$$

A common estimate for the wave speeds, which is also used in [20], [113], [77] and [109] is

$$\begin{aligned} S_{\mathrm{L}} &= \min\left(\mathbf{v}_{\mathrm{L}} \cdot \mathbf{n} - \sqrt{g h_{\mathrm{L}}}, u^* - \sqrt{g h^*}\right) \\ S_{\mathrm{R}} &= \max\left(\mathbf{v}_{\mathrm{R}} \cdot \mathbf{n} + \sqrt{g h_{\mathrm{R}}}, u^* + \sqrt{g h^*}\right) \end{aligned} \tag{4.22}$$

with the velocity vector $\mathbf{v} = (u, v)$ and

$$\begin{aligned} u^* &= \frac{1}{2}(\mathbf{v}_{\mathrm{L}} + \mathbf{v}_{\mathrm{R}}) \cdot \mathbf{n} + \sqrt{g h_{\mathrm{L}}} - \sqrt{g h_{\mathrm{R}}} \\ \sqrt{g h^*} &= \frac{1}{2}(\sqrt{g h_{\mathrm{L}}} + \sqrt{g h_{\mathrm{R}}}) + \frac{1}{4}(\mathbf{v}_L + \mathbf{v}_{\mathrm{R}}) \cdot \mathbf{n}. \end{aligned} \tag{4.23}$$

In presence of a dry neighbour cell the estimates reduce to

$$S_{\mathrm{L}} = \begin{cases} \mathbf{v}_{\mathrm{L}} \cdot \mathbf{n} - \sqrt{g h_{\mathrm{L}}} & \text{if the right neighbour cell is dry} \\ \mathbf{v}_{\mathrm{R}} \cdot \mathbf{n} - 2\sqrt{g h_{\mathrm{R}}} & \text{if the left neighbour cell is dry} \end{cases} \tag{4.24}$$

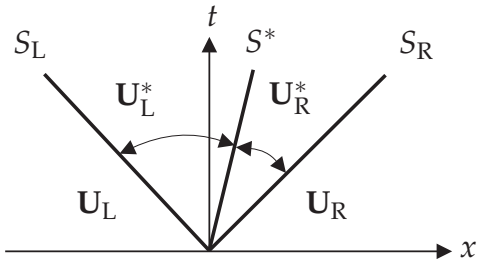

Figure 4.5.: Wave Structure assumed in the HLLC solver.

respectively

$$S_R = \begin{cases} \mathbf{v}_L \cdot \mathbf{n} + 2\sqrt{gh_L} & \text{if the neighbour cell is dry} \\ \mathbf{v}_R \cdot \mathbf{n} + \sqrt{gh_R} & \text{if the neighbour cell is dry.} \end{cases} \tag{4.25}$$

The assumption of a two wave structure as done in the HLL solver is not suitable for all kinds of flow problems. Especially for problems in two space dimensions, the neglection of intermediate waves can lead to smearing. The main disadvantage of the two wave assumption is that shear waves and contact discontinuities can not be resolved. A solver which considers an intermediate wave is the HLLC solver.

HLLC Solver

The HLLC solver assumes three waves emanating from the cell interface: the two fastest waves as well as a contact wave propagating at intermediate speed. Figure 4.5 shows the configuration. The derivation of the HLLC flux is similar to that of the HLL flux. The formulation of the integral conservation law yields Equation (4.14). To include the contact wave, the left part of Equation (4.14) is splitted in two parts, one going from $\Delta t S_L$ to S^* and the other from S^* to $\Delta t S_R$ where S^* is the speed of the intermediate wave. Definition of the intermediate states $\mathbf{U}_L^*$ and $\mathbf{U}_R^*$, substitution into the consistency condition (Equation (4.11)) and application of the Rankine Hugoniot condition yields the HLLC flux expressed by

$$\mathbf{F}_{i+\frac{1}{2}}^{\text{HLLC}} = \begin{cases} \mathbf{F}_L & \text{if } 0 \leq S_L \\ \mathbf{F}_L^* = \mathbf{F}_L + S_L(\mathbf{U}_L^* - \mathbf{U}_L) & \text{if } S_L \leq 0 \leq S^* \\ \mathbf{F}_R^* = \mathbf{F}_R + S_R(\mathbf{U}_R^* - \mathbf{U}_R) & \text{if } S^* \leq 0 \leq S_R \\ \mathbf{F}_R & \text{if } 0 \geq S_R. \end{cases} \tag{4.26}$$

To compute the HLLC intercell flux, an approximation for the intermediate wave speed is necessary. In [106] it is recommended to estimate the intermediate speed as

$$S^* = \frac{S_L h_R (u_R - S_R) - S_R h_L (u_L - S_L)}{h_R (u_R - S_R) - h_L (u_L - S_L)}. \tag{4.27}$$

4.2.2. Test Example

The two approximate Riemann solvers HLL and HLLC are compared within a numerical test example. Further, the example should verify that the finite volume discretisation of the Shallow Water Equations including the flux approximation is implemented correctly. As an example, a problem similar to a circular dam break problem is chosen. The domain is quadratic (20 x 20 m) and discretised with an equidistant grid with 50 cells in each coordinate direction. At the boundaries of the domain a no flow boundary condition is imposed. Thus, no water can enter or exit the domain. The initial water depth follows a Gaussian distribution with

$$h = 2.0 + 3.0\ e^{\left(\frac{-(x-10)^2-(y-10)^2}{4}\right)}. \tag{4.28}$$

The bottom of the domain is flat and friction forces are neglected. Figures 4.6 and 4.7 show the time dependent change of the water level for the time steps $t = 0, 1, 2, 3, 4, 5, 10$ and 15 s. For a better illustration isolines representing the water depth are added to the figures.

Both solvers show the expected symmetrical behaviour. Since the flux approximation is based on a two point stencil, flow behaviour in diagonal direction is slightly different than in coordinate direction and wave propagation is not perfectly radial. When comparing the isolines of the water depth distribution time steps $t = 1s$ and $t = 3s$, the HLLC solver seems to exhibit steeper waves. This can indicate better shock capturing properties due to the consideration of an intermediate wave.

In summary, the results of both solvers are very similar. For pavement surface runoff modelling, one is not interested in the detailed description of the wave front but rather in the resulting water depth distribution. And since the differences are very small, the two wave assumption of the HLL solver is justifiable. Another advantage of the HLL solver is its computational efficiency. It is slightly faster than the HLLC. Therefore, the HLL solver is chosen as the standard solver in the pavement surface runoff model.

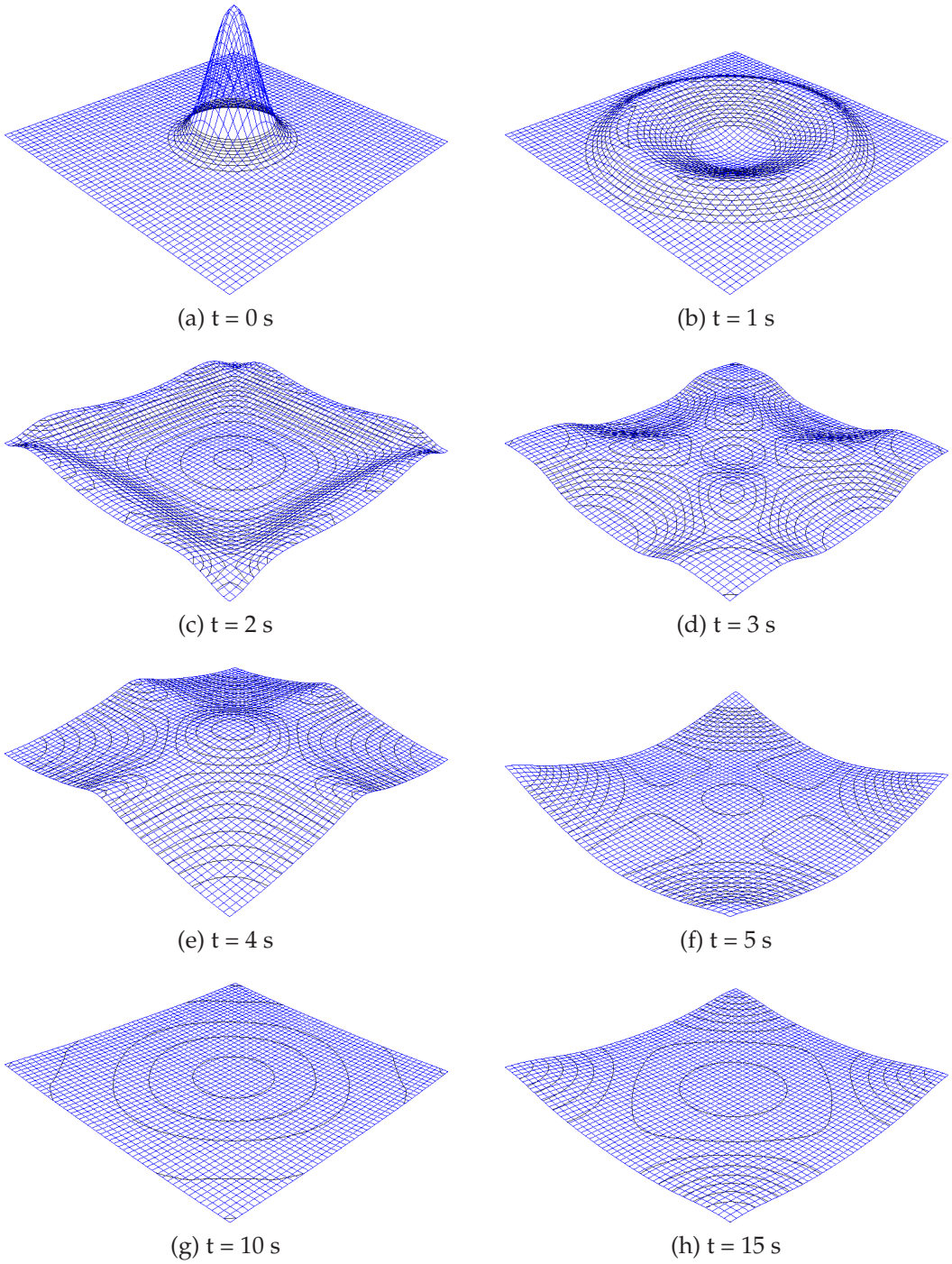

(a) t = 0 s (b) t = 1 s

(c) t = 2 s (d) t = 3 s

(e) t = 4 s (f) t = 5 s

(g) t = 10 s (h) t = 15 s

Figure 4.6.: Time dependent water level calculated with the HLL solver.

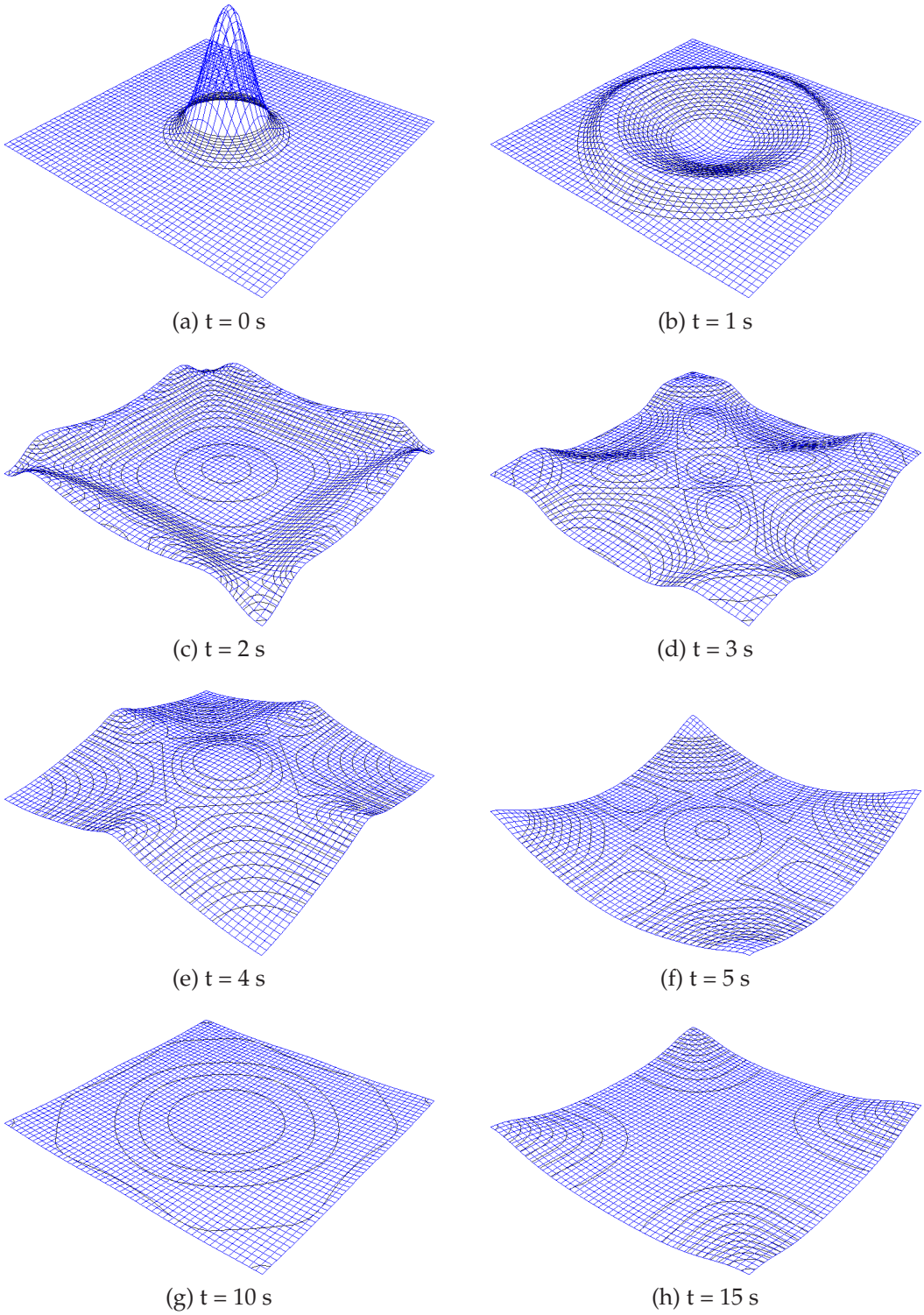

(a) t = 0 s (b) t = 1 s

(c) t = 2 s (d) t = 3 s

(e) t = 4 s (f) t = 5 s

(g) t = 10 s (h) t = 15 s

Figure 4.7.: Time dependent water level calculated with the HLLC solver.

4.3. Source Term Discretisation

Source terms in the Shallow Water Equations include topography $\mathbf{Q_0} = gh\mathbf{S}_0$ and flow resistance $\mathbf{Q}_\mathrm{f} = gh\mathbf{S}_\mathrm{f}$. Currently, the numerical treatment of source terms is subject to extensive research. Much effort has been put in developing and improving approximate Riemann solvers but they exclusively deal with homogeneous partial differential equations. Homogeneous equations, though, can barely be applied to practical flow problems where source terms exert a great influence on the flow behaviour. Especially, when dealing with irregular topography and large gradients, high roughness coefficients or wetting and drying, source terms can evoke great numerical difficulties if they are not well-balanced with the flux approximation.

4.3.1. Topography

The topography source term in the Shallow Water Equations is defined as

$$\mathbf{Q_0} = \begin{pmatrix} 0 \\ gh\, S_{0,\mathrm{x}} \\ gh\, S_{0,\mathrm{y}} \end{pmatrix} \tag{4.29}$$

where $S_{0,\mathrm{x}}$ and $S_{0,\mathrm{y}}$ represent the bottom slopes in the coordinate directions. The discretisation of the source term can follow various concepts:

- treatment in an upwinding manner like the flux approximation,
- inclusion into the flux term or
- straight evaluation of the source term.

The treatment of the source term in an upwinding manner is proposed in [11] or [15]. Like the intercell flux, the source term is splitted according to the wave structure of the underlying Riemann problem. It is recommended to use the same wave structure as for the flux approximation. Most often, the upwinding of the source term is used in combination with the Roe approximate Riemann solver.

In [108], the topography source term is reformulated as divergence term. This allows to include it in the flux term. The divergence formulation for the topography source term is

$$\frac{\Delta t}{\Delta V} \int\limits_{\Delta V} \mathbf{S}_0 \, dV = \frac{\Delta t}{\Delta V} \sum_{r=1}^{4} (\frac{1}{2} g h_r^2 \cdot \mathbf{n} \, A_r). \tag{4.30}$$

In the equation, h_r is the water depth at the interface r with length A_r. Figure 4.8 shows a section of an equidistant grid with two neighbour cells i and j. For the

centre cell, the water level η_i is additionally illustrated. It is assumed to be horizontal and is defined as the sum of water depth h_i and bottom elevation $z_{b,i}$:

$$\eta_i = h_i + z_{b,i}. \tag{4.31}$$

First, the bottom elevation at the interface $z_{b,r}$ is determined by averaging the bottom elevations of the neighbouring cells:

$$z_{b,r} = \frac{1}{2}(z_{b,i} + z_{b,j}). \tag{4.32}$$

Then, the water depth above each interface is estimated by subtracting the bottom elevation of the interface from the cell-averaged water level η_i:

$$h_r = \eta_i - z_{b,r}. \tag{4.33}$$

The influence of bottom slope in the divergence formulation is thus represented as the difference in water depth at the four interfaces related to the horizontal water level.

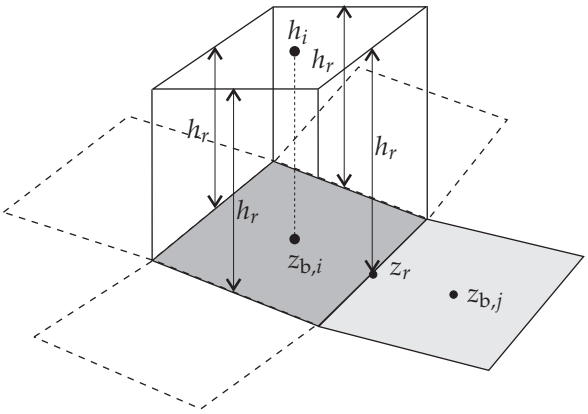

Figure 4.8.: Determination of water depth at the interface when using the divergence term formulation.

In [108], the divergence term formulation yielded very good results. The method was also implemented and tested within the pavement surface runoff model. Due to the small water depths though, numerical instabilities occurred, which is shortly explained by reference to Figure 4.9. The figure shows the profile of a cell. The solid line represents the bottom and the dashed line the water level. If the water level is assumed horizontal and the cell averaged water depth is very small, the water depth at the interface might become negative. For this reason, this discretisation method is rejected.

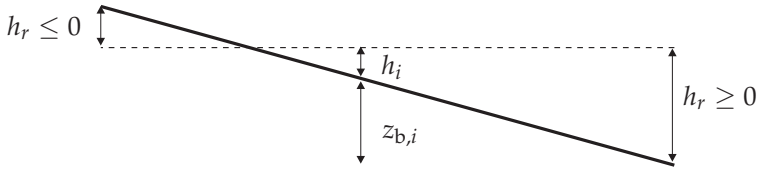

Figure 4.9.: Determination of water depth at the interface when using the divergence term formulation in combination with very small water depths.

In the pavement surface runoff model, the most simple way to discretise the source term is chosen. It is the straight evaluation of the source term equation (Equation (4.29)). However, in contrast to the conserved variables, which are stored as cell averaged values at the cell centre, bottom elevations are stored at the cell vertices. This has two advantages. First, the bottom elevation is continuous across the interface without exhibiting a jump discontinuity. Second, the average bottom slopes of a cell, which are needed for the evaluation of the source term are determined independently of the neighbouring cells. Although, in a quadrilateral grid, the vertices are not necessarily on the same plane, the bottom slopes are determined by an averaging method. First, the average bottom elevation for the interfaces $z_{b,r}$ is calculated:

$$z_{\mathrm{br},i} = \frac{1}{2}(z_{\mathrm{b},i} + z_{\mathrm{b},i+1}). \tag{4.34}$$

Then, the bottom slopes $S_{0,\mathrm{x}}$ and $S_{0,\mathrm{y}}$ are determined to:

$$\begin{aligned} S_{0,\mathrm{x}} &= \frac{(z_{\mathrm{br},1} - z_{\mathrm{br},3})}{\Delta x} \\ S_{0,\mathrm{y}} &= \frac{(z_{\mathrm{br},2} - z_{\mathrm{br},4})}{\Delta y}. \end{aligned} \tag{4.35}$$

The discretisation of the topography source term is tested with a well-known benchmark test where an analytical solution is available [77, 65, 108, 115]. It considers a 25 m long frictionless channel. At $x = 10$ m a bump is placed at the channel bottom. The bottom elevation at the bump is defined by:

$$z_{\mathrm{b}} = 0.2 - 0.05\ (x - 10)^2. \tag{4.36}$$

The domain is discretised with an equidistant grid with 250x10 cells of size 0.1 m. Depending on the boundary conditions imposed at the inflow (left) and outflow boundary (right), different flow states occur, which result in different profiles for the water level at the steady state. Three sets of boundary conditions are considered:

- subcritical: $(hu)_{\mathrm{inflow}} = 4.42\,\mathrm{m}^2/\mathrm{s}$, $h_{\mathrm{outflow}} = 2\,\mathrm{m}$
- transcritical: $(hu)_{\mathrm{inflow}} = 1.53\,\mathrm{m}^2/\mathrm{s}$, $h_{\mathrm{outflow}} = 0.66\,\mathrm{m}$

- transcritical with shock: $(hu)_{\text{inflow}} = 0.18\,m^2/s$, $h_{\text{outflow}} = 0.33\,\text{m}$.

The simulated time is 150 s for the subcritical and transcritical case and 300 s for the transcritical case with the shock. Figure 4.10 compares the resulting water level of the numerical model and the analytical solution. It can be observed that for all three cases there is a very good agreement.

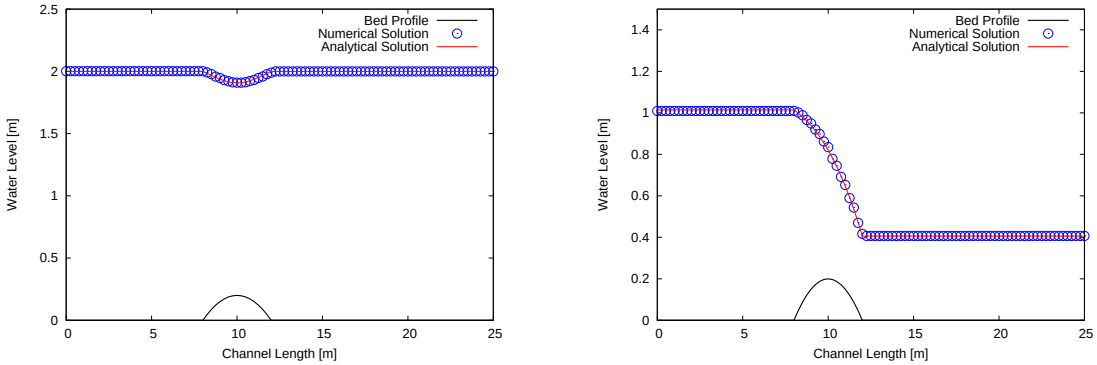

(a) Subcritical

(b) Transcritical

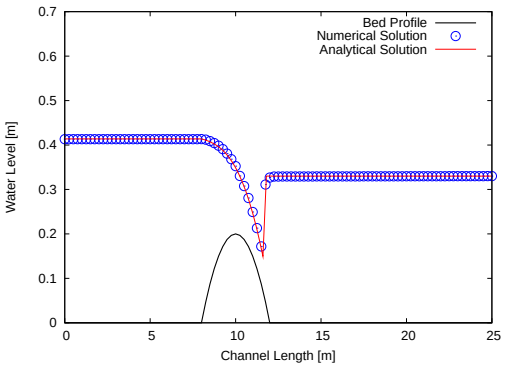

(c) Transcritical with shock

Figure 4.10.: Water level profiles for various boundary conditions at the steady state: comparison of analytical and numerical solution.

4.3.2. Flow Resistance

The flow resistance source term $\mathbf{Q}_f = ghS_f$ in the Shallow Water Equations can be implemented in an explicit [37, 108], semi-implicit [15, 109] or fully implicit way [78, 113, 70, 10]. Especially when water depths are very small, an explicit treatment can cause numerical instabilities whereas a semi-implicit or implicit treatment of the flow resistance source term stabilise the solution.

Small water depths and a notable influence of bottom roughness suggest a fully implicit discretisation of the flow resistance source term in the pavement surface

runoff model. This is achieved with an operator splitting technique as described for example in [78]. Operator splitting enables the overall update of the conserved variables ΔU to be splitted in two parts: an explicit update ΔU_{expl}, which includes the intercell fluxes and the topography source term and an implicit update ΔU_{impl}, which includes the flow resistance source term. The explicit update is used as initial condition for the implicit update.

In a cell-centred finite volume method assuming piecewise constant data, the implicit update of cell i is an ordinary differential equation:

$$\frac{d\mathbf{U}_{i,\mathrm{impl}}}{dt} = \mathbf{Q}_{\mathrm{f}}. \tag{4.37}$$

Performing a Taylor series expansion about the n^{th} time level leads to

$$\mathbf{Q}_{\mathrm{f},i}^{n+1} = \mathbf{Q}_{\mathrm{f},i}^{n} + \left(\frac{\partial \mathbf{Q}_{\mathrm{f,i}}}{\partial U}\right)^{n} \Delta \mathbf{U}_{i,\mathrm{impl}} + O(\Delta U^2). \tag{4.38}$$

After some algebraic manipulations and the neglection of the higher order terms Equation (4.38) can be written as

$$\left(\mathbf{I} - \Delta t \frac{\partial \mathbf{Q}_{\mathrm{f,i}}^{\mathbf{n}}}{\partial U}\right) \Delta \mathbf{U}_{i,\mathrm{impl}} = \Delta t\, \mathbf{Q}_{\mathrm{f,i}}^{\mathbf{n}} \tag{4.39}$$

where $\mathbf{I}$ is the identity matrix and $\partial Q_{\mathrm{f},i}^{n}/\partial U = \mathbf{J}_{\mathrm{f}}$ the Jacobian matrix of the flow resistance term. It can be easily verified that the implicit update can be determined by solving the system of non-linear equations for $\Delta \mathbf{U}_{i,\mathrm{impl}}$.

In the pavement surface runoff model, the update sequence with explicit and implicit update is implemented as follows. First, the explicit part is solved and the explicit time step is determined by the CFL restriction. The global solution is then updated yielding $\mathbf{U}_{i,\mathrm{expl}}^{n+1}$. As mentioned before, the explicit solution $\mathbf{U}_{i,\mathrm{expl}}^{n+1}$ is taken as initial condition for the solution of the implicit part. The implicit part is solved with the time step determined for the explicit part yielding $\Delta \mathbf{U}_{i,\mathrm{impl}}$. Finally, the new solution can be determined to

$$\mathbf{U}_{i}^{n+1} = \mathbf{U}_{i,\mathrm{expl}}^{n+1} + \Delta \mathbf{U}_{i,\mathrm{impl}}. \tag{4.40}$$

The CFL restriction is applied for the explicit part. Since the influence of flow resistance damps the flow velocities, the CFL restriction is rather too stringent and anyway fulfilled for the entire solution.

For the evaluation of the implicit discretisation of the flow resistance part, a benchmark is used which has been already presented in [48] and [54]. The analytical solution can be found in [48]. The test example considers the rainfall-runoff from an inclined slab. At the downstream end of the slab discharge produced by the runoff is

measured and summarised to a hydrograph. Flow resistance is modelled using the Manning equation. The length of the slab is $l = 400$ and bottom slope is $s = 0.05$ %. Manning's n is chosen to $n = 0.02$ and rainfall intensity is $i = 0.33$ mm/min. Rainfall starts at $t = 0$ min and ends after $t = 200$ min. The total simulated time is $t = 300$ min. Therefore, the drying process is partially simulated in this problem. The domain is discretised by an equidistant grid with 400 cells.

Figure 4.11 compares the hydrograph of the analytical solution and the hydrograph generated with the numerical model.

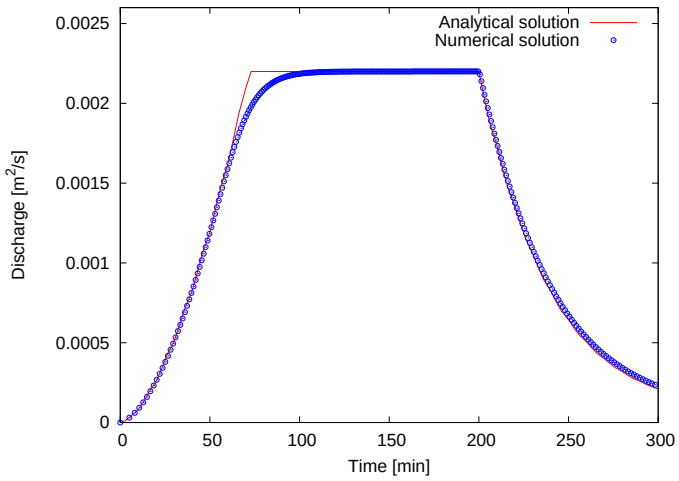

Figure 4.11.: Discharge at the outflow boundary of an inclined slab over time using the Manning's resistance equation: comparison of analytical and numerical solution.

It can be observed that the steady state is reached after 100 min simulated time. Until the steady state is reached, discharge increases almost linearly. As soon as rainfall stops, discharge decreases. There is a very good agreement between the numerical and analytical results. The deviation of the solutions between $t = 50$ and 100 min can be significantly reduced when using a finer mesh [54].

In summary, this chapter defined the numerical model to solve the Shallow Water Equations. Discretisation was done with a cell centred finite volume method on a cartesian grid. To account for the hyperbolic characteristic of the equations, the HLL approximate Riemann solver was applied to determine the intercell fluxes. It is the simplest of the Godunov type Riemann solvers and was considered to be sufficient for the modelling of pavement surface runoff. The topography source term was discretised by a direct evaluation of the term. For the flow resistance discretisation an implicit scheme on the basis of an operator splitting method was chosen. This enables to solve the flow resistance source term without numerical instabilities. The

discretisation was tested with well-known benchmarks. In the following chapter, the numerical model is adapted to handle real pavement surface runoff problems.

5. Pavement Surface Runoff Model

In the previous chapter, the numerical framework to solve the Shallow Water Equations was set up. It allows to solve flow problems including arbitrary bottom topography and flow resistance. This chapter covers the adaption of the Shallow Water Equations to yield a model which is able to describe pavement surface runoff considering the requirements formulated in Chapter 2. These include: the import and processing of topographic point data, the development of a flow resistance model, which is able to consider various pavement surface textures and a model to represent drainage facilities.

5.1. Import of Topographic Data

Topography in the Shallow Water Equations is represented by the bottom slopes in both coordinate directions. The bottom slopes are calculated from the bottom elevations, which are stored at the vertices of each grid cell (see Section 4.3.1). There are two ways to assign bottom elevations to the grid vertices: by geometric functions or the interpolation of point clouds.

If a surface can be described mathematically, bottom elevations can be directly assigned to the vertices applying the underlying geometric function. Usually, these surfaces are alignment elements, e. g. transition curves. They are used as model surfaces for example to perform alignment parameter studies. Model surfaces are restricted to a rectangular model domain. For alignment elements this implies that only the vertical alignment as well as the superelevation of the cross section are considered. Curvature is neglected because it can not be represented by a rectangular domain. For drainage purposes curvature is not an essential parameter. Therefore, the application of rectangular model domains is possible.

Complexity increases if instead of isolated alignment elements, road sections with several different elements or variable road widths are modelled. In this case, it is cumbersome to establish the geometric functions and it would be helpful to use data from CAD based highway design tools. Another application is the examination of existing road sections for which alignment parameters are not available anymore. Further, one could be interested to model the real pavement topography including

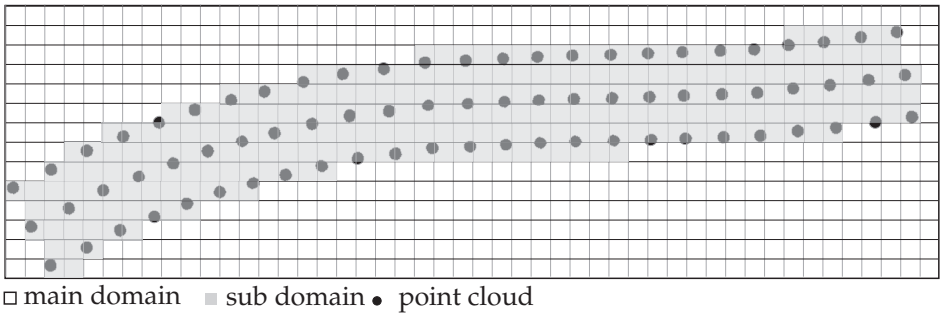

Figure 5.1.: Main and sub domain of a grid defined by a point cloud.

the irregularities caused by traffic loading. For the latter application data originating from lidar (light detection and ranging) measurements should be processed. If point clouds either exported from CAD tools or generated by lidar measurements are used to represent the pavement's topography, bottom elevations have to be interpolated to the grid vertices.

Another specialty evokes when looking at the shape of the point clouds. In contrast to the model surfaces, the domain represented by a point cloud is not rectangular because curvature is included in the data. The elimination of curvature via coordinate transformation is only possible when the alignment elements and parameters are known. Since this assumption will not hold in the majority of cases, the model is extended to treat arbitrary shaped domains. The import and processing of arbitrary shaped point clouds is divided in three steps. First, a rectangular bounding box with an equidistant grid is reconstructed around the point cloud as shown in Figure 5.1. Then, the sub domain occupied by the point cloud is defined by setting up a boundary polygon. Since the sub domain is relevant for the simulation, only grid vertices within the sub domain are interpolated from the point cloud. For the simulation, the sub domain is exported as an independent grid to the model using the "Multi Domain Grid" module available in DUNE [104]. The method developed for the definition of the boundary polygon (boundary tracing) and the chosen interpolation algorithm are presented in the subsequent sections.

5.1.1. Boundary Tracing

For the processing of point clouds, the definition of the boundary polygon is essential. If point data is exported from a CAD tool the boundary polygon is already known. Therefore, boundary tracing mainly focuses on data generated with lidar measurements.

The boundary tracing algorithm developed in this work is based on the theory of convex hulls [30, 67]. A convex hull is defined as the minimal set of connected

boundary points surrounding the entire data set. This implies that all angles between the polygon sections are $< 180°$. Relating this to a visual presentation, a convex hull can be compared to an elastic rubber band spanned around the data set as shown in Figure 5.2a. The convex hull is also the shortest way to enclose the data set.

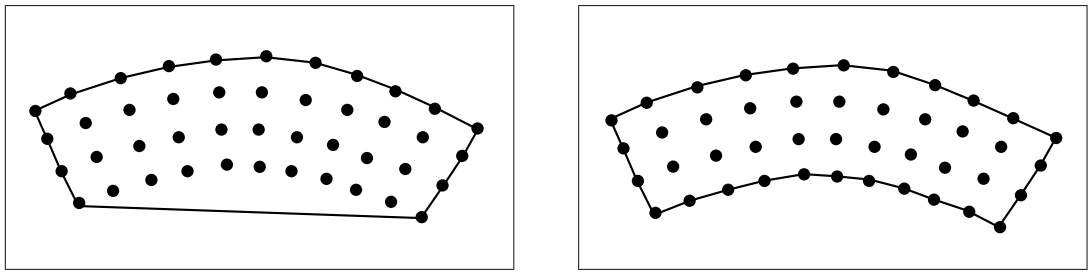

(a) Convex hull (b) True boundary

Figure 5.2.: Convex hull and true boundary of a point cloud.

For the computation of the convex hull, computational geometry provides several algorithms, e.g.the graham scan, Jarvis march or quick hull algorithm [50, 93]. Graham scan is the fastest of the above mentioned and therefore included in the Pavement Surface Runoff Model. It is described shortly by reference to Figure 5.3.

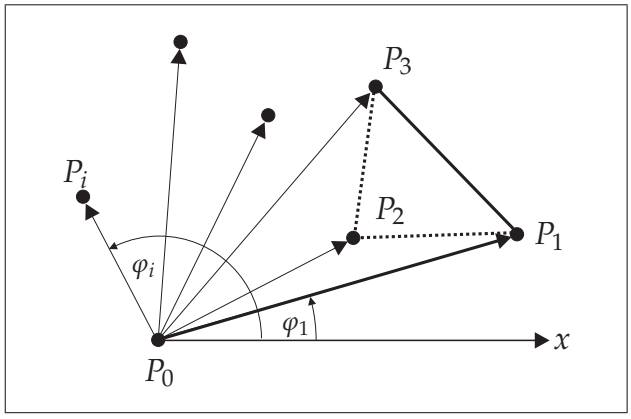

Figure 5.3.: Concept of the graham scan algorithm to determine the convex hull of a point cloud.

First, a data point P_0 is selected which definitely is part of the convex hull. A possible choice would be the left-, rightmost, lowest or uppermost point of the data set. Subsequently, the angles φ_i from P_0 to all other data points are computed and sorted anti clockwise in increasing order $P_1 - P_i$. Sorting of the point cloud is time consuming and point clouds processed in the Pavement Surface Runoff Model can

include up to 500,000 points. Thus, a stable and fast sorting algorithm is needed such as the merge sort or quicksort algorithm [28]. In this work, the merge sort algorithm is implemented. It is a stable comparison-based algorithm on the basis of the 'divide and conquer' principle. Contrary to quicksort, it needs less comparisons to sort a data set. Assuming n points, its worst case performance is about $O(n\,log(n))$ comparisons whereas quicksort has $O(n^2)$.

After the data points have been sorted, a stack is created and filled with the first two points P_0 and P_1. In each step, the algorithm checks three points, the two points on top of the stack, which are already part of the convex hull, and the new point. The basic idea of graham scan is that during the traversion of the sorted data set only left turns are allowed. At first, the algorithm looks at P_0, P_1 and P_2 and checks if the third point lies left or right of $\overline{P_0P_1}$. In figure 5.3, P_2 is left. Consequently, P_1 is further on part of the convex hull and P_2 is added to the stack. The next step includes P_1, P_2 as upper elements of the stack and P_3 as new point. Since P_3 lies right of $\overline{P_1P_2}$, P_2 is no longer part of the convex hull and erased from the stack. P_3 is added instead. The algorithm will proceed until all points are checked and the boundary polygon is complete. Finding the convex boundary polygon for a point cloud is almost trivial. The construction of the boundary polygon of point clouds representing road geometries is challenging though. The reason is that in the majority of cases they are not convex. Consider the point cloud in Figure 5.2b. There are convex as well as concave parts and the true boundary does not match the convex hull in figure 5.2a. On freeways, curvature of the roadcurb is usually very small. However, the smallest concave curvature distorts the boundary polygon. Therefore, the method has to be modified such that also concave boundaries are detected.

One method to detect non-convex boundaries are so called alpha shape methods [7, 35, 82]. Alpha shapes are a generalisation of the convex hull and constitute a subgraph of the Delaunay triangulation. For a finite point set S and a real parameter alpha with $0 \leq \alpha \leq \infty$, the alpha shape of S is a polytope, which is not necessarily convex. The level of detail of the alpha shape is controlled by α. For sufficiently large alpha, the alpha shape is identical to the convex hull of S. As alpha decreases, the shape shrinks and gradually develops cavities. For sufficiently small α, the alpha shape is empty. A big advantage of the method is that it even works on unevenly distributed data sets. Draw-backs are that α has to be chosen properly. Therefore, the performance of the method strongly depends on α. Furthermore, the method is computationally complex and intensive. Another approach is to divide the data into subsets and to apply the convex hull algorithms to the sub sets as done in [99]. Such methods are easier to implement as alpha shapes. However, they only work well on evenly distributed data sets. Data originating from lidar measurements is evenly distributed and due to the easier implementation, the latter approach is used.

A method is developed which is further on referred to as segmented graham scan.

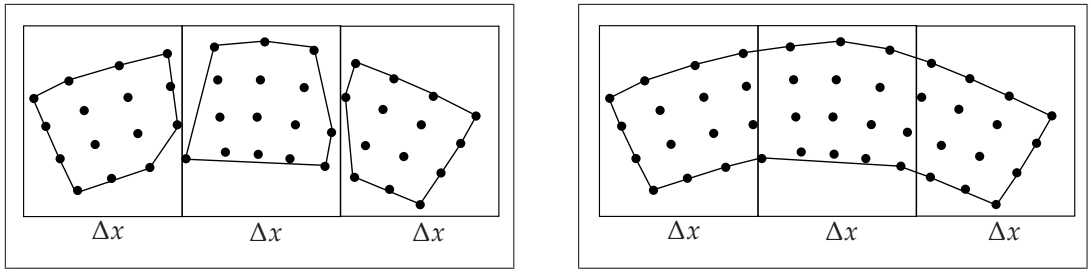

(a) Segmented Graham Scan (b) Result of the Segmented Graham Scan

Figure 5.4.: Preliminary and final result of a segmented graham scan.

It divides the data set into an arbitrary number of rectangular segments with equal widths Δx as shown in 5.4a. For each segment, the convex hull is computed with the ordinary graham scan method. Next, the convex hulls of the segments are merged. After merging, points which belonged to the convex hull of a segment are not necessarily part of the convex hull of the whole data set. These points are eliminated as follows: For each point of the data set the angles to all other data points are calculated. If the difference between the smallest and biggest angle exceeds a given value $\varphi_{\text{boundary}}$ the point is identified as true member of the convex hull. Results of the method strongly depend on the choice of φ and Δx. If the concavity of the data set is pronounced with boundary angles $< 120^\circ$, the results are not perfectly reliable. Therefore, it is recommended to set $\varphi_{\text{boundary}} > 120^\circ$.

Figure 5.5 shows the influence of the segment width Δx. The boundary points of a road section are determined with the segmented graham scan for the segment widths Δx of $1, 2, 5, 7$ and 10 m. The smaller Δx the more points in the concave part are detected. For $\Delta x = 7$ m, point density in the concave parts is already much lower than in the convex parts of the point cloud. If Δx exceeds a certain value concave boundaries are not detected at all (Figure 5.5e). The choice of Δx depends on the shaping and the density of the data set. Besides a maximum limit, Δx should also not be chosen too small to guarantee a sufficient number of points in a subset. Unlike the ordinary graham scan where boundary points are ordered anti clockwise in the stack, the sequence in the stack resulting from the segmented graham scan is orderless. To define the boundary polygon, boundary points have to be sorted. Due to the concave parts of the boundary, conventional methods to generate the boundary polygon fail. Instead, points are sorted by distance in a nearest neighbour sense. However, it has to be guaranteed that the distance between two boundary points across the polygon (what corresponds to road width) is bigger than the distance along the boundary. Otherwise, sorting fails. Therefore, it is convenient to choose Δx well below the modelled road width to assure that the maximum distance of two polygon points is smaller. A reasonable range for Δx can be given to $2 \leq \Delta x \leq 10$ m.

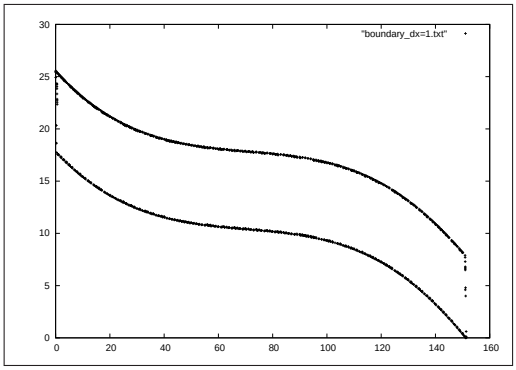

(a) Δx = 1 m

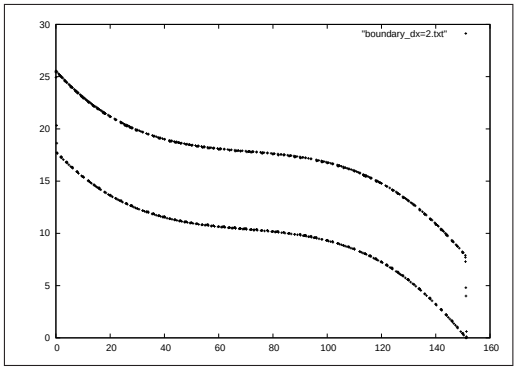

(b) Δx =2 m

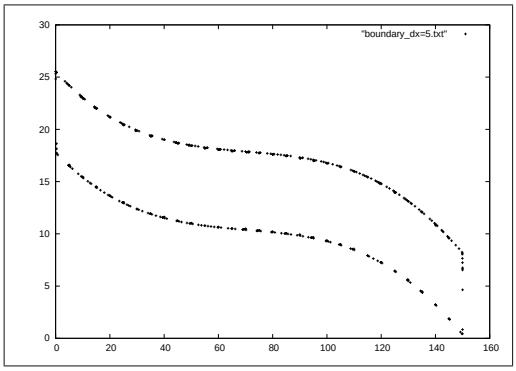

(c) Δx =5 m

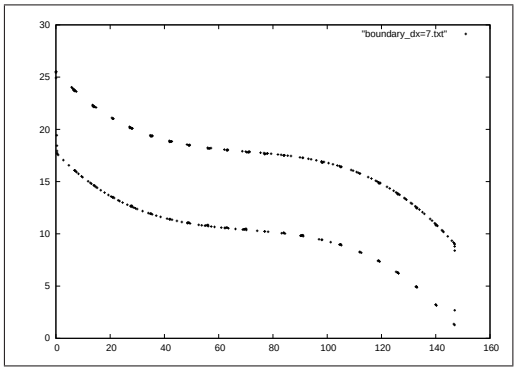

(d) Δx =7 m

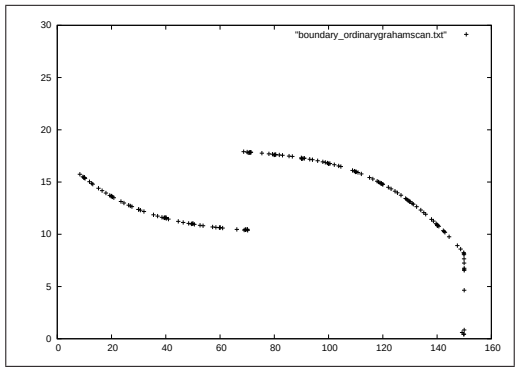

(e) Δx =10 m

Figure 5.5.: Boundary points determined by a segmented graham scan with variable segment widths Δx [m].

In summary, the segmented graham scan algorithm developed for the Pavement Surface Runoff Model allows to define the boundary polygon for the majority of point clouds. Most road sections exhibit small concavities compared to the size of the entire domain. However, the method inherits limitations. If concave angles along the boundary are $\varphi_{\text{boundary}} < 120^{\circ}$ application of the segmented graham scan does not yield proper results. Further on, the sorting of the boundary points with the nearest neighbour method can only be safely applied if the distance of boundary points along the boundary is significantly higher than across the boundary.

5.1.2. Interpolation

Various methods for spatial interpolation exist. An extensive overview of methods and their classification is given in [19] and [75]. A short summary is given in the following:

- Global vs local: global interpolation methods use the entire data set for interpolation and capture the general trend. A change in a single value may therefore affect the whole domain. Global methods tend to generate smooth surfaces with less abrupt changes. Local methods are repeatedly applied to subsets of the data. A changed input value may therefore only affect the result in the subset. Local methods capture the short-range variation which may also lead to abrupt changes. Global methods are for example trend surface analysis or regression models. Nearest neighbour methods or triangulation are local methods.

- Deterministic vs stochastic: in contrast to deterministic models, stochastic models include the concept of randomness. Besides the estimation of missing data, they provide an error prediction for the estimation. An example for a stochastic model is kriging which is often used in geostatistics.

- Exact vs inexact: if a surface is generated with an exact interpolation method, every data point used for interpolation is part of the surface. An example are triangular irregular network based models. An inexact method is regression or trend surface analysis where data points are not necessarily part of the generated surface.

- Grid based vs triangular: In terrain modelling, triangular irregular network as well as grid based models are used to reconstruct surfaces. All geometric elements like quadrilaterals, polygons, etc. can be split up in a set of triangles. Triangles are therefore the basic geometric element which can be adapted well to nearly every shape. Triangle based methods are thus used to describe broken terrain with steep slopes and break lines and they are suitable for any data pattern, regular or irregular [76]. The triangular network is generated via a

triangulation algorithm such as the delaunay triangulation. Implementation and data handling are fairly complex. Grid based models, which work on rectangular grid cells, are easy to implement and to handle [13]. They are suited to model rolling terrain over large areas. However, they do not work well with clustered data or data originating from contour lines. Grid based models are for example nearest neighbour, natural neighbours or inverse distance weighting.

For the reconstruction of the pavement topography, a local and deterministic model is chosen. The only decision left is whether the model is triangle or grid based, exact or inexact. Since the Pavement Surface Runoff Model works on a cartesian grid, it is necessary to have gridded elevation data. If a triangular based method was used, elevations at the vertices would have to be determined via interpolation within the triangular structure. Consequently, the triangulation as well as interpolation procedure would have to be implemented. When a grid based model is used, only the interpolation procedure has to be implemented. Data from lidar measurements is dense and regularly distributed. Therefore, the grid based inverse distance weighting algorithm is chosen.

Inverse distance weighting is a widely used, inexact, spatial interpolation method to create raster overlays from point data [19]. The main idea of this method can be described best by Tobler's first law of geography: *"Everything is related to everything else, but near things are more related than distant things."* [83]. It assumes that the elevation of an unknown point is inversely related to the distance to its known neighbours. The unknown elevation of a vertice i can be determined by the summation of the weighted elevations of the neighbouring data points :

$$z_i = \sum_{k=1}^{n} w_k z_k \tag{5.1}$$

where n is the number of data points used for the interpolation and w_k is the weighting factor expressed by

$$w_k = d_{ik}^{-p}. \tag{5.2}$$

The weighting factor w_k of a single neighbour is proportional to its distance d_{ik}. Proportionality can be varied by the power parameter p. To ensure that the sum of weights equals one, the single weight factor is normalised with the sum of weights:

$$w_k = \frac{d_{ik}^{-p}}{\sum_{k=1}^{n} d_{ik}^{-p}}. \tag{5.3}$$

If a point coincides with a grid vertice, the weight is set to 1 and all other weights to 0. The number of data points included in the interpolation n is either determined by specifying a fix search radius or a fix number of data points. In this model, both

parameters are specified. The fix search radius restricts the area the model has to screen. A fix number of data points ensures that always the same number of points is used. Since n is constant over the entire domain the method only works for equally distributed data. On irregularly distributed data, the search radius for regions with sparse data could become too small to get the desired number of points. Usually, n is chosen between 15 and 30 [17]. When choosing n it is important that the data points surround the unknown point so that every possible direction is covered. One disadvantage of inverse distance weighting is that it is not directional. If a point is only estimated with data points from the same direction, the result might be distorted. Therefore, inverse distance weighting does not work when data from contour lines is interpolated.

As already mentioned. the power parameter p decides whether the distance weighting is more or less than proportional. Three cases are distinguished:

- $p > 1$: distance will be accounted more than proportional,
- $p = 1$: corresponds to an inverse proportionality,
- $p < 1$: distance will be accounted less than proportional.

The most popular choice is $p = 1$ or 2 [17, 75]. Although it seems that the choice of p is rather arbitrary it also depends on the the data pattern, especially on data density. If data is dense, p should not be too big as all neighbouring points will have relatively large weights. A value for p close to 1 ensures that very close points do not have too much influence on the result. If data points are sparse, a bigger value for p should be chosen so that closer points explicitly have more influence. Apparently, a constant value for p can only be satisfactory for an equally distributed data set with a fairly constant density. Data used in the Pavement Surface Runoff Model are dense and equally distributed. Thus, a constant p is chosen and set to $p = 1$ by default.

The advantage of inverse distance weighting is its easy implementation. Disadvantages are that it only works reliably on equally distributed and fairly dense data sets and that the interpolation is not directional. To face these shortcomings, several modifications if the method for the use with scattered data sets were developed. For detailed information about the improved methods the reader is referred to [44, 75, 101].

5.2. Flow Resistance

Flow resistance in the Pavement Surface Runoff Model is described by the Darcy-Weisbach equation. Reasons for this choice are given in Section 3.2.3. For the estimation of the resistance coefficient f a model based on experimental data is developed.

First, the experimental setup is described. Afterwards, different methods to setup a model for the estimation of f are discussed and relevant parameters are defined. Finally, the experimental data is analysed with the chosen method and results are discussed.

5.2.1. Experimental Setup

Data to calibrate the flow resistance model originates from experiments performed in [95]. The experimental setup is only described briefly herein. For more information the reader is referred to [56] and [95].

Figure 5.6 shows a schematic view of the test station. The experiments were carried out on platforms 2.0 m in length and 1 m in width. The platforms consisted of variable asphalt and concrete material placed on a steel plate. The concrete covers were additionally textured after placement with jute fibre cloth and artificial turf. For the characterisation the roughness of the surface covers, mean texture depth k was measured with the sand patch method described in Section 2.1.4. Five surface covers were tested:

- concrete with jute fibre texture (CJ), k = 0.4 mm,
- concrete with artificial turf texture (CAT), k = 0.84 mm,
- stone matrix asphalt with 8 mm max. grain size (SMA08), k = 0.89 mm,
- stone matrix asphalt with 11 mm max. grain size (SMA011), k = 0.98 mm and
- dense graded asphalt with 8 mm max. grain size (DGA), k = 1.83 mm.

The platforms were adjustable in longitudinal slope. Tested slopes varied from 0.5 % to 5 %. Rainfall was simulated with a pipe system containing regularly spaced leaks. The leak diameter was 0.6 mm and the spacing 15 cm. The rainfall intensities generated with the pipe system ranged from 0.5 mm/min to 1.5 mm/min. According to the definitions made in Section 2.1.1 this corresponds to a very strong rain event. Beneath the pipe system, a metal grid mesh with mesh size 3 mm was installed to ensure realistic drop sizes and a random but steady distribution of the drops. In addition to the rainfall simulator there was an inflow installed on top of the platform. Inflow varied from 0.0 m^3/h up to 5 m^3/h.

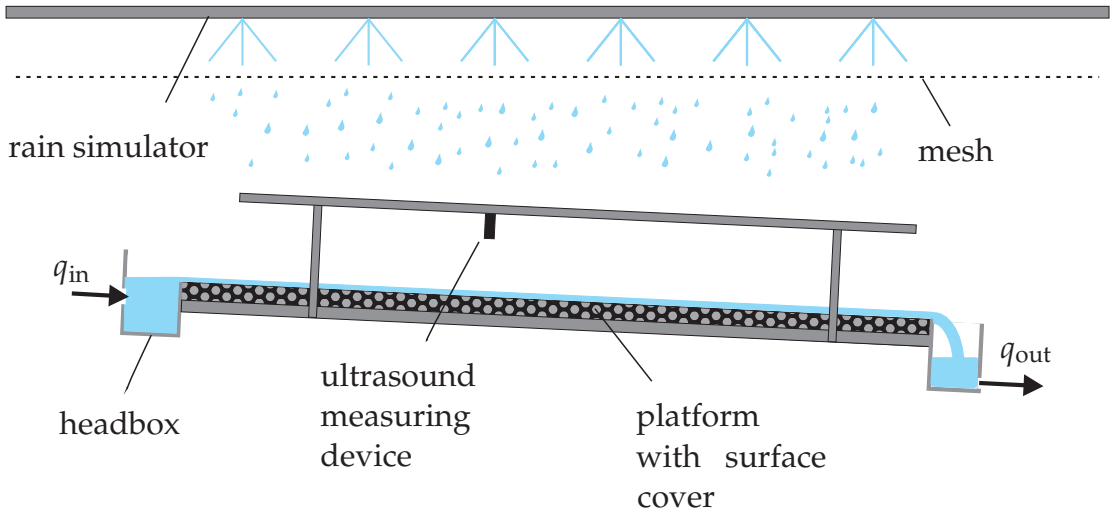

Figure 5.6.: Schematic view of the test station used in [95].

Water depths on the platform were measured at 27 points with an ultrasound measuring device. The experiments showed that water depths did not increase in downstream direction. Further on, the cross section and surface texture remained constant over the platform. Therefore, uniform conditions were assumed and all water depth measurements were combined to one averaged water depth per experiment as shown in Figure 5.7a:

$$h = \frac{1}{n}\sum_{i=1}^{n} h_i \quad \text{with} \quad n = 27. \tag{5.4}$$

The averaged water depth h was used to calibrate the one dimensional model in [95]. It is also used in the Pavement Surface Runoff Model as conservative variable and for the calibration of the resistance model. This corresponds to the assumption of a flat bottom with a certain resistance coefficient where the actual texture geometry is neglected as shown in Figure 5.7b. As mentioned in Section 2.1.4, the surface texture provides a retention volume and therefore, the averaged water depth h is not a sound parameter to describe the hydroplaning risk. Only the water depth above the roughness peaks is relevant for the hydroplaning effect. Therefore, an additional water depth is defined, which takes into account the retention volume. This parameter is called the referenced water depth h_{ref} and can be calculated as

$$h_{ref} = h - k \tag{5.5}$$

as shown in Figure 5.7c. The simulations are based on h, the visualisation of water depths is done on the basis of h_{ref}.

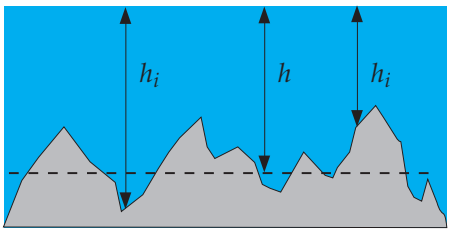

(a) Averaged water depth h

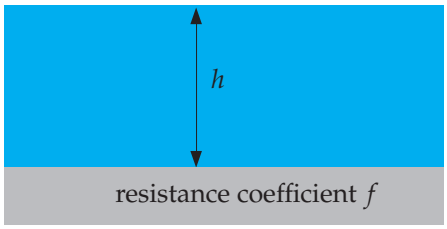

(b) Model concept for flow resistance

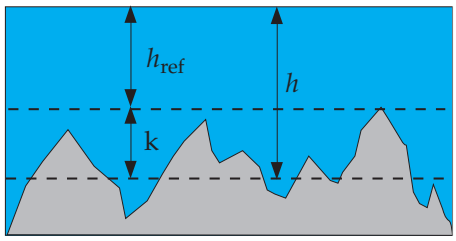

(c) Referenced water depth h_{ref}

Figure 5.7.: Definition of averaged and referenced water depth and model concept for flow resistance.

The experiments in [95] were carried out with and without simulated rainfall. The tests with rainfall though were limited to a zero inflow condition. In total, 275 configurations were tested (75 with and 200 without rainfall). Available data from the experiments are discharge q and averaged water depth h. For the experiments carried out without rainfall, q is readily available from the inflow measurement. As mentioned before uniform flow is assumed. For the experiments with simulated rainfall, q is not available since flow is gradually varied and discharge changes along flow path. Discharge would have to be determined depending on rainfall intensity at every cross section where water depth is measured. Since only three measurements per cross section are available the experiments with simulated rainfall are neglected in this study. This is acceptable since the effect of rainfall on the flow variables was shown to be very small [25, 95]. For the calibration of the resistance model a set of 200 data points (40 for each surface cover) are available.

5.2.2. Estimation of the Resistance Coefficient

Assuming steady state and uniform flow conditions, the Darcy-Weisbach resistance coefficient f can be computed from the experiments by

$$f = \frac{8gh^3S_0}{q^2}. \tag{5.6}$$

The process which influences flow resistance in pavement surface runoff the most, is bottom friction. Bottom friction in turn is caused by the pavement's surface texture. For the characterisation of the surface texture, mean texture depth k is available from the experiments. Therefore, the objective is to set up a general equation to estimate f depending on mean texture depth. A general equation will enable to estimate f also for surface covers which were not considered in the experiments. Although bottom friction will be the only parameter used to estimate the resistance coefficient, it has to be noted that the quantities obtained from the experiments also include other effects on flow resistance, like turbulence or shape resistance. Therefore, these effects are included indirectly in the resistance model.

Existing Approaches to Estimate the Resistance Coefficient

For pipe flow the Darcy-Weisbach resistance coefficient f can be determined by Equation (3.51) if the velocity profile near the boundary is known. For turbulent flow, the velocity profile can be assumed to be logarithmic. The logarithmic equations derived for pipe flow have been modified to open-channel flow on the basis of extensive experiments. A general form of these equations for the flow regimes 'smooth' and fully 'rough' was given by the ASCE Task Force on Friction Factors in Open Channels, which are presented in [38]:

$$\text{Smooth:} \qquad \frac{1}{\sqrt{f}} = c\ log_{10}\left(\frac{a\,h}{k_s}\right) \tag{5.7}$$

$$\text{Rough:} \qquad \frac{1}{\sqrt{f}} = c\ log_{10}\left(\frac{Re\sqrt{f}}{b}\right). \tag{5.8}$$

The coefficients a, b and c vary with channel shape among others. Values are also given in [38]. In these equations, the Reynolds Number and an inundation ratio based on the equivalent sand grain roughness h/k_s are used as explaining parameters. For open-channel flow over very rough and irregular surfaces, like natural river beds, equations depending on other parameters than k_s and Re such as grain size distribution or roughness density were established. A detailed review can be found in [1, 34] and [98].

The use of logarithmic equations to estimate the resistance coefficient constitutes the standard analysis technique in open-channel flow hydraulics. However, they can not be applied in this work for the following reasons. First, they presume fully turbulent flow conditions. Pavement surface runoff is, however, dominated by Reynolds Numbers covering the entire flow regime from laminar to turbulent with a significant portion being in the transitional regime. Second, the parameters describing the roughness of a surface, e. g. k_s, are not available from the experiments. Third, the logarithmic equations presume sufficient inundation.

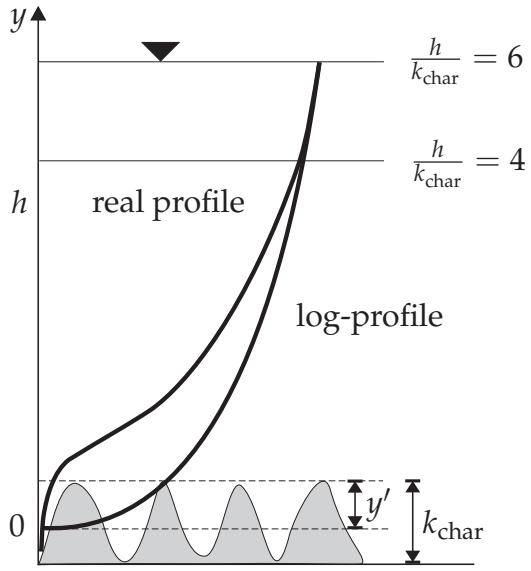

Figure 5.8.: Comparison of real and logarithmic velocity profile for a flow over large scale roughness according to [34] (not to scale).

Inundation is expressed by the inundation ratio λ, which is defined as the relation of water depth h to a characteristic length scale of the rough surface k_{char}

$$\lambda = \frac{h}{k_{char}}. \tag{5.9}$$

In the equations posted above, the characteristic length scale of the rough surface is the equivalent sand grain roughness k_s and therefore, $k_{char} = k_s$. In the following, mean texture depth is chosen as characteristic length scale for the surface roughness in pavement surface runoff since it is available from the experiments. It follows that $k_{char} = k$. In pavement surface runoff, mean texture depth has a similar length scale as water depth and therefore it exhibits rather low inundation ratios, which range only up to $\lambda = 15$. For low inundation ratios, the velocity profile of turbulent flow close to the boundary deviates from the logarithmic shape as shown in Figure 5.8. According to [34] the profiles coincide at an inundation ratio of $\lambda = 4$. Comparing mean texture depth k with the characteristic length scale marked in Figure 5.8 and recapitulating the definition of k in Section 2.1.4, it has to be noted that k is not absolutely equal to k_{char}. It rather follows that $k < k_{char}$. Therefore, threshold values for λ may be slightly bigger using k than using k_{char}. Approximately 50 % of the experimental data is below $\lambda = 4$. If an increased threshold is assumed due to the difference between k and k_{char}, the portion even increases. As a consequence, an altered velocity profile should be considered in the Pavement Surface Runoff Model.

In summary, the application of existing logarithmic equations to estimate f is rejected because the condition of fully turbulent flow is not met. Furthermore, for low

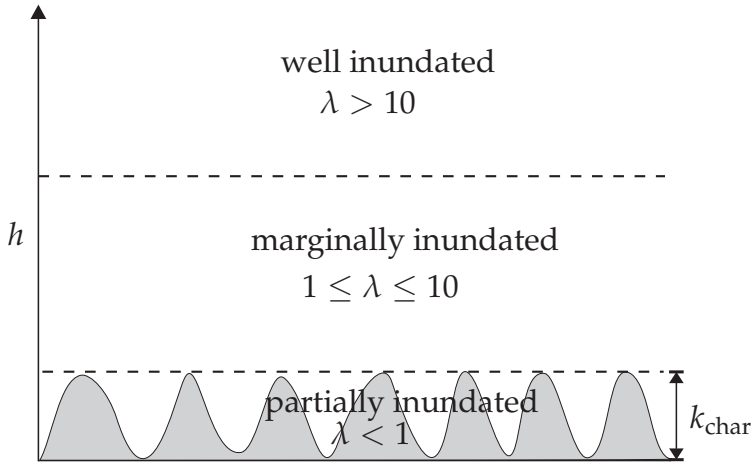

Figure 5.9.: Flow regions defined in [72] depending on inundation ratio λ.

inundation ratios, the velocity distribution near the boundary deviates from the logarithmic profile. Consequently, velocity measurements would be needed to verify the velocity profile. Measurements of the velocity profile are, however, not available and it would be difficult to measure them for such small water depths.

Nevertheless, inundation is a parameter which strongly influences flow resistance over rough surfaces. An approach to estimate f depending on inundation ratio was given in [72]. Depending on $\lambda = h/k_{char}$ three flow regimes are defined (also see Figure 5.9):

- well inundated: $\lambda > 10$,
- marginally inundated: $1 \leq \lambda \leq 10$ and
- partially inundated: $\lambda < 1$.

In the well inundated region roughness elements are relatively small compared to the flow depth and fully rough flow conditions can be assumed. Since a high inundation allows to interpret roughness rather as a microscale than macroscale roughness, standard hydraulic analyses can be applied. The following logarithmic equation is derived for fully rough turbulent flow

$$\frac{1}{\sqrt{f}} \backsim 1.64 + 0.803\, ln(\lambda). \tag{5.10}$$

In [72], comparison with experimental data showed that the well inundated region can be described sufficiently by Equation (5.10). The fact that the logarithmic law (Equation (5.10)) is suggested for $\lambda > 10$ confirms the assumption that the velocity profile deviates from the logarithmic shape close to the boundary. Recalling that $k < k_{char}$ the threshold for being in a well inundated region would be even larger than 10. Consequently, this region is neglected.

The marginally inundated flow region is also characterised by fully inundated roughness elements. However, inundation is small enough that roughness affects the whole velocity profile. It is assumed that the disturbance introduced into the flow field scales with the size of the roughness elements. The following equation is derived mathematically applying a modified mixing length model where mixing length scales with surface roughness

$$f = 10\ \lambda^{-2}. \tag{5.11}$$

The potential relationship of f and λ could not be verified in [72] due to a lack of available data. Furthermore, hydraulics in this region are not well understood yet. Nevertheless, it is the region which is of interest when modelling flow resistance for pavement surface runoff.

In the third region, roughness elements are partially inundated. Variations in water depth do not only result in changes of flow resistance but also change the hydraulic radius. Further, the effect of individual roughness elements becomes important. To account for this, the drag force associated with a roughness element is used to estimate bottom shear stress. For spherical particles and a bimodal distribution of particles an equation for f is presented in [72]. For a highly heterogeneous surface such as the pavement surface texture, drag forces can not be determined reliably. In this work, the partially inundated region is therefore neglected. Instead, it is assumed that no considerable flow occurs when $\lambda < 1$.

Since the marginally inundated region is the one of interest in this work, the potential relationship of Equation (5.11) is checked on the available experimental data. Figure 5.10 shows the computed f-values plotted against λ. There is a tendency of decreasing flow resistance with increasing inundation. However, data is considerably scattered and the potential relationship can not be verified clearly. For this reason, a new approach to estimate the resistance coefficient is developed in this work, which is presented in the following section.

Approach Used in this Work

The preceeding section illustrated that inundation ratio λ influences the flow resistance coefficient f. Since no clear relationship could be established with the experimental data, other parameters influencing f have to be found. To identify the relations among physical quantities, dimensional analysis is a powerful tool. Therefore, a dimensional analysis of the momentum equation is performed. For reasons of simplicity, the one dimensional momentum equation is chosen. Since steady and uniform conditions are assumed in the experiments, only the steady state is considered. Applying these simplifications to the one dimensional momentum equation

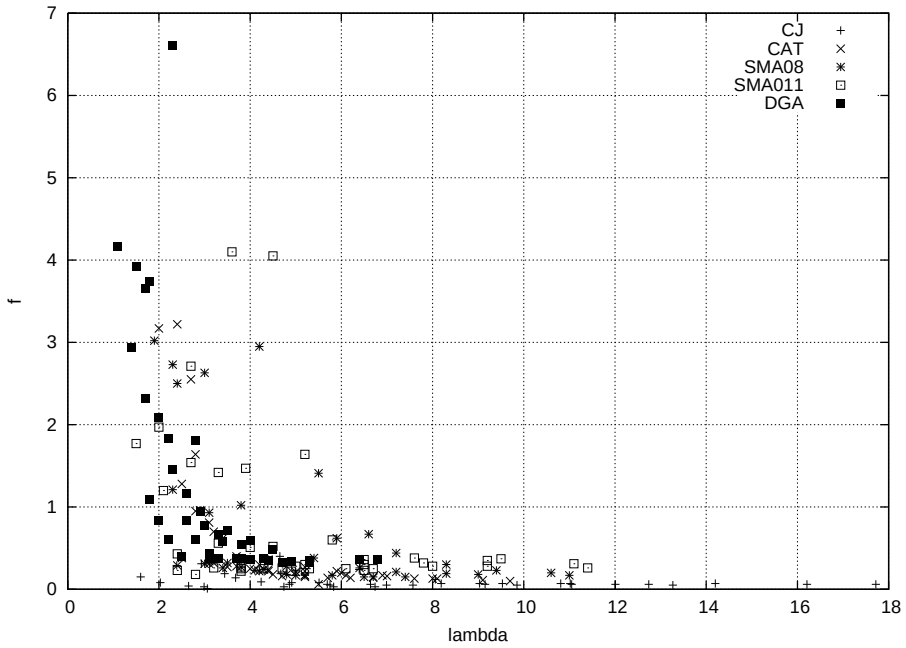

Figure 5.10.: Darcy-Weisbach resistance coefficient f plotted against inundation ratio λ for the five investigated surface covers.

yields:

$$\frac{\partial z_b}{\partial x} = f\frac{u^2}{8gh}. \tag{5.12}$$

First, a characteristic length l_c and a characteristic acceleration $a_c = g$ are defined. This enables the definition of dimensionless expressions for water depth $\mathcal{H}$, velocity $\mathcal{H}$, length $\mathcal{X}$, bottom elevation $\mathcal{Z}$ and gravity $\mathcal{G}$:

$$\mathcal{H} = \frac{h}{l_c}, \qquad \mathcal{V} = \frac{u}{\sqrt{gl_c}}, \qquad \mathcal{X} = \frac{x}{l_c}, \qquad \mathcal{Z} = \frac{z_b}{l_c}, \qquad \mathcal{G} = \frac{g}{g} = 1. \tag{5.13}$$

Inserting the expressions into Equation (5.12) and solving for f yields

$$f = \frac{\partial \mathcal{Z}}{\partial \mathcal{X}}\,\frac{8\mathcal{H}}{\mathcal{V}^2}. \tag{5.14}$$

Depending on the choice of l_c, two dimensionless groupings can be generated. Note that independent of the choice of l_c, the term $\partial\mathcal{Z}/\partial\mathcal{X}$ will always yield bottom slope as a dimensional parameter.

Usually, water depth h is chosen as characteristic length l_c. Then, the resistance coefficient f can be expressed as a function of bottom slope S_0 and Froude Number Fr since $\mathcal{H} = 1$. The dimensionless grouping can thus be identified as:

$$f = f(Fr, S_0). \tag{5.15}$$

An estimation of f using one of these parameters would fail because mean texture depth k is not included as well as any other friction related parameters. For the development of the second dimensionless grouping, it is therefore suggested to define l_c as mean texture depth k. As mentioned before, bottom slope S_0 can be already identified as part of the dimensionless grouping. The dimensionless water depth can be formulated as

$$\mathcal{H} = \frac{h}{k} = \lambda \tag{5.16}$$

which corresponds to inundation ratio. Finally, the dimensionless velocity can be written as

$$\mathcal{V} = \frac{u}{\sqrt{gk}} = Fr_k. \tag{5.17}$$

The expression for the dimensionless velocity is similar to that of the Froude Number. Thus, it is further on defined as texture related Froude Number Fr_k. It represents the relation of inertial forces of the flow and the gravitational forces acting at height k. Finally, the second dimensionless grouping can be summarised as

$$f = f(\lambda, Fr_k, S_0). \tag{5.18}$$

The influence of λ on f was already illustrated in Figure 5.10. No clear relationship $f = f(\lambda)$ could be identified. In Figure 5.11, f is plotted against the texture related Froude Number Fr_k. Although data is slightly scattered, the potential dependency is much more distinct than for λ. To model flow resistance in pavement surface runoff, mean texture depth was defined significant. Therefore, it is mandatory to include either λ or Fr_k or both quantities into a flow resistance model. Bottom slope S_0 can be included as a second parameter. This will be discussed later.

Besides their influence on the resistance coefficient, inundation ratio and texture related Froude Number exhibit one important difference: inundation ratio depends on water depth and the texture related Froude Number depends on velocity. Water depth and velocity are directly coupled and therefore, including both quantities into the model is rejected. (Data analysis moreover showed that adding inundation ratio to the model does not increase its accuracy.) Furthermore, the influence of Fr_k is more pronounced. For this reason, it is chosen as an explaining variable in the resistance model. Bottom slope, which is independent of mean texture depth might be added as a second explaining variable as mentioned before. Figure 5.11 shows again f plotted against the texture related Froude Number Fr_k. However, data is not grouped by surface cover but by bottom slope. It can be verified that bottom slope influences the resistance coefficient and that f can probably be expressed as a family of potential functions $f = f(Fr_k, S_0)$.

So far, the texture related Froude Number Fr_k was derived from dimensional analysis. It will be used as explaining variable for an estimation of the resistance coefficient f. In the next section possible potential equations depending on Fr_k and

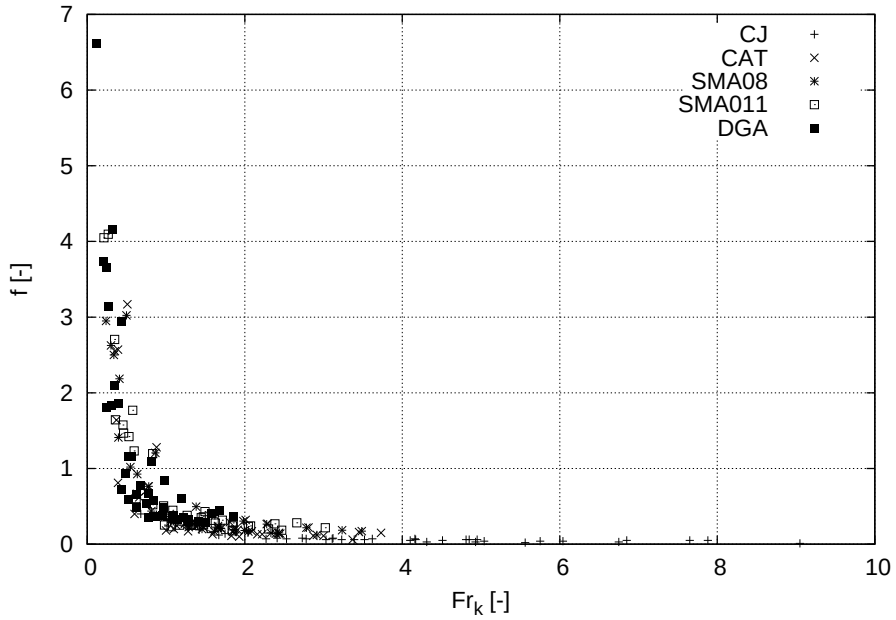

Figure 5.11.: Darcy-Weisbach resistance coefficient f plotted against the texture related Froude Number Fr_k for the five investigated surface covers.

optionally S_0 will be set up an fitted to the experimental data to obtain a general equation for the estimation of the resistance coefficient depending on mean texture depth.

5.2.3. Data Analysis and Results

Three potential functions are set up and fitted to the experimental data. A one parameter model, which only includes the texture related Froude Number as explaining variable

$$f = a\,(Fr_k)^c \tag{5.19}$$

and a two parameter model with an additional linear dependency on bottom slope

$$f = (a\,S_0 + b)\,{Fr_k}^c \tag{5.20}$$

which is further on referred to as linear two parameter model. Finally, a potential two parameter model of the form

$$f = a\,{S_0}^b\,{Fr_k}^c \tag{5.21}$$

is formulated. Curve fitting is performed with the least squares method on the basis of the entire data set containing all surface covers. In this way, the resulting resistance model has general coefficients and can also be used for surface covers which

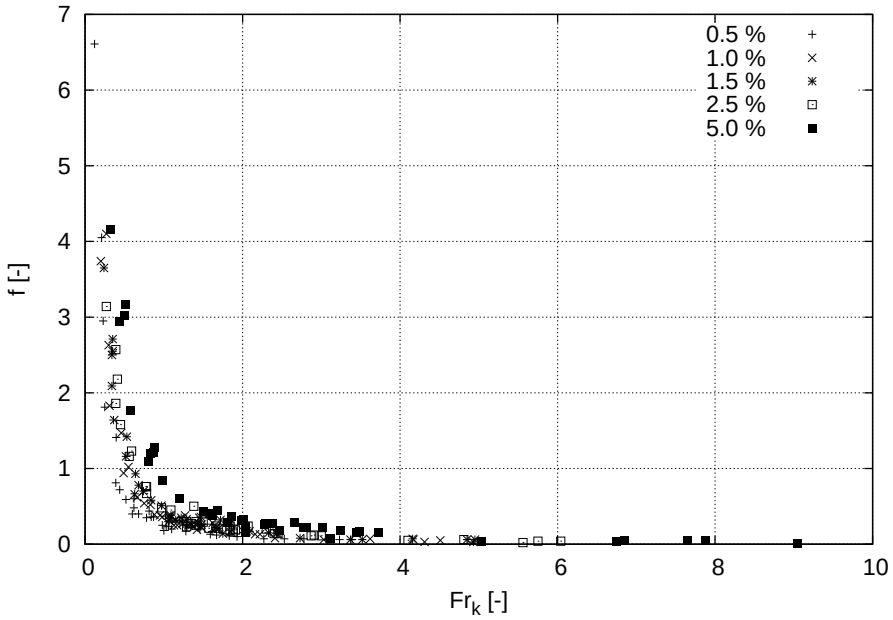

Figure 5.12.: Darcy-Weisbach resistance coefficient f plotted against the texture related Froude Number Fr_k for the five investigated surface covers and variable bottom slopes.

were not tested in the experiments. The coefficients of determination R are calculated for each surface cover separately to better evaluate the fit. The coefficient of determination is interpreted as the percentage of explained data expressed by

$$R = 1 - \frac{RSS}{SSY} \qquad R \leq 1 \tag{5.22}$$

with RSS being the residual sum of squared errors

$$RSS = \sum_{i=1}^{n} (f_{i,\text{experiments}} - f_{i,\text{model}})^2 \tag{5.23}$$

and SSY the sum of squared measured f-values

$$SSY = \sum_{i=1}^{n} (f_{i,\text{experiments}})^2. \tag{5.24}$$

Table 5.1 presents the results of the curve fitting process with the three models. In general, the two parameter models have higher coefficients of determination than the one parameter model. The question is if the increased accuracy is justifiable in a physical sense or if it is just a mathematical phenomenon. Adding an additional explaining variable to a regression model will always increase its mathematical accuracy. On the one hand, longitudinal slope is reflected by velocity and therefore

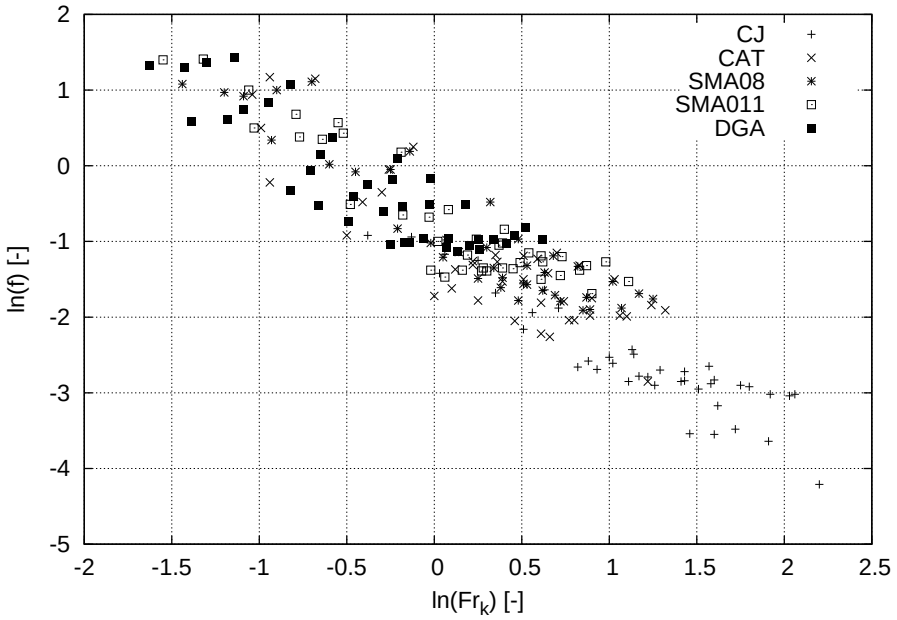

Figure 5.13.: Logarithmus of the Darcy-Weisbach resistance coefficient $ln(f)$ plotted against $ln(Fr_k)$ for the investigated surface covers.

would not have to be included necessarily as a separate explaining variable. On the other hand, velocity is not explicitly included in the equation but only indirectly by Fr_k. To account explicitly for gravitational forces due to longitudinal slope, S_0 is therefore added to the model.

When looking at the results for the surface covers, CJ has the lowest coefficient of determination independent of the model used. In case of the one parameter model, actually $R < 0$. A negative coefficient of determination indicates that the sum of the squared deviations exceeds the sum of the squared "f-values". This can be explained by the fact that the curve fitting process is performed on the whole data set. The least squares method weights the absolute deviations and tries to find the minimum deviation with respect to the whole data set. Since CJ has the lowest resistance coefficients because of the small mean texture depth, deviations for other surface covers, especially SMA011 and DGA, have a bigger influence on the fit. Therefore, the absolute deviations for CJ with respect to the entire data set are small but the relative deviations with respect to the CJ data set are big. To achieve a more balanced fit, data and model equations are transformed to a logarithmic form. Figure 5.13 shows the $ln(f)$-values plotted against the $ln(Fr_k)$-values. It can be seen that each surface cover roughly covers the same range of $ln(f)$. Therefore, deviations in the fitting process are also in the same range and a more balanced fit is expected. The

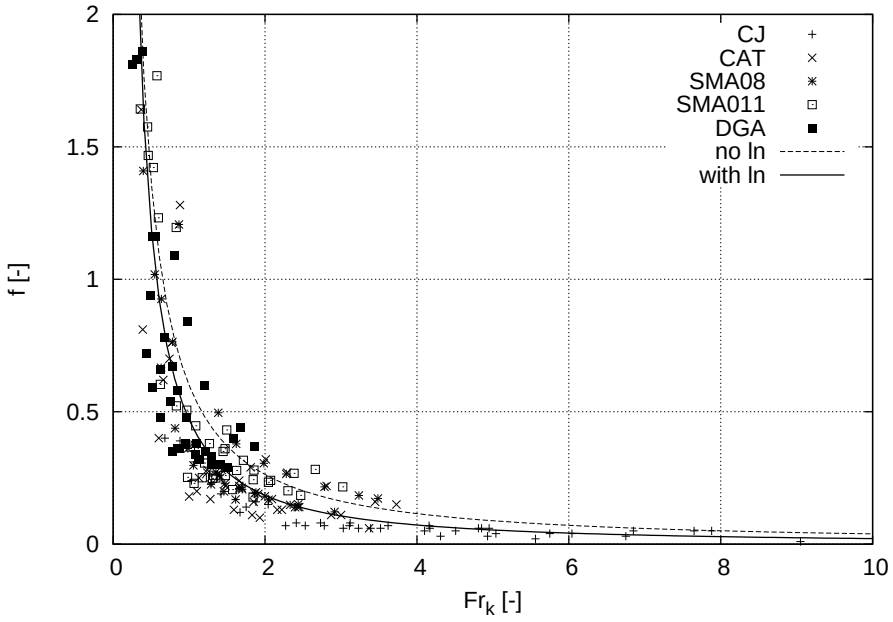

Figure 5.14.: Comparison of the non-logarithmic and logarithmic fit for the Darcy-Weisbach resistance coefficient.

model equations in logarithmic form read:

$$\begin{aligned} ln(f) &= ln(a) + c\ ln(Fr_k) \\ ln(f) &= ln(a\,S_0 + b) + c\ ln(Fr_k) \\ ln(f) &= ln(a) + b\ ln(S_0) + c\ ln(Fr_k). \end{aligned} \tag{5.25}$$

After the logarithmic equations are fitted to the experimental data, the model equations including the coefficients are transformed back into the original equations. Figure 5.14 shows the resulting curves with a non-logarithmic and a logarithmic fit for the one parameter model. As expected, the curve resulting from the logarithmic approach achieves a more balanced fit. This can be confirmed when looking at the coefficients of determination shown in Table 5.2. In contrast to the non logarithmic fit, CJ has much higher coefficients of determination. However, coefficients of determination for the other surface covers are slightly lower. Due to the more balanced fit, the equations from the logarithmic fit are used in the Pavement Surface Runoff Model. The equation with the best performance is the potential two parameter model.

Surface cover	$f = 0.6\,Fr_k^{-1.19}$	$f = (13.93\,S_0 + 0.28)\,Fr_k^{-1.41}$	$f = 3.41\,S_0^{0.45}\,Fr_k^{-1.44}$
CJ	-0.13	0.74	0.79
CAT	0.76	0.95	0.96
SMA08	0.89	0.98	0.98
SMA011	0.94	0.95	0.95
DGA	0.91	0.98	0.98

Table 5.1.: Coefficients of determination for the one and two parameter models.

Surface cover	$f = 0.47\,Fr_k^{-1.35}$	$f = (5.0\,S_0 + 0.36)\,Fr_k^{-1.40}$	$f = 3.50\,S_0^{0.47}\,Fr_k^{-1.50}$
CJ	0.62	0.82	0.88
CAT	0.75	0.83	0.95
SMA08	0.87	0.92	0.98
SMA011	0.93	0.93	0.95
DGA	0.89	0.95	0.99

Table 5.2.: Coefficients of determination for the one and two parameter models calculated with the logarithmic transformation.

5.2.4. Extended Model Equations

The experiments used to calibrate the resistance coefficient were restricted to one dimension. Therefore, the model equations have to be extended to two dimensions. Additionally, new Jacobians for the implicit friction update have to be defined.

The model used to describe the resistance coefficient f in one dimension is

$$f = a{S_0}^b \, {Fr_k}^c = a{S_0}^b \left(\frac{u}{\sqrt{gk}} \right)^c . \tag{5.26}$$

When the equation is extended to two dimensions it has to be discussed if velocity and bottom slope are included as vectorial or scalar quantities. Since mean texture depth is the main factor of influence and it is assumed that it is independent of direction, the resistance coefficient should be a scalar quantity. Therefore, velocity and bottom slope are not included as vectors but as scalars representing the absolute cell values defined by

$$|U| = \sqrt{u^2 + v^2} \qquad \text{and} \qquad |S_0| = \sqrt{S_{0,\mathrm{x}}^2 + S_{0,\mathrm{y}}^2}. \tag{5.27}$$

This results in a scalar resistance coefficient for a cell. Friction slope S_f in two dimensions can be written as:

$$S_\mathrm{f} = a|S_0|^b \left(\frac{\sqrt{u^2 + v^2}}{\sqrt{gk}} \right)^c \begin{pmatrix} 0 \\ \frac{u\sqrt{u^2+v^2}}{8gh} \\ \frac{v\sqrt{u^2+v^2}}{8gh} \end{pmatrix} . \tag{5.28}$$

For the implicit friction update according to Equation (4.39) the Jacobian $\mathbf{J}_\mathrm{f}$ of the flow resistance source term $\mathbf{Q}_\mathrm{f} = gh\,\mathbf{S}_\mathrm{f}$ is needed. The Jacobian of the newly introduced two parameter model is presented in the Appendix A.1.

5.3. Drainage Model

An effective drainage of road pavements is essential to maintain their service level and traffic safety. Drainage facilities consist of the visible gutter and inlets on the pavement as well as the closed drain system underground, which conveys the water from the inlet to the point of discharge. Here, only the gutters and inlets are considered, which remove the storm water from the pavement.

There are two possible failures of drainage facilities. First, the drainage capacity of the drain system is exceeded what results in backwater effects. These are not

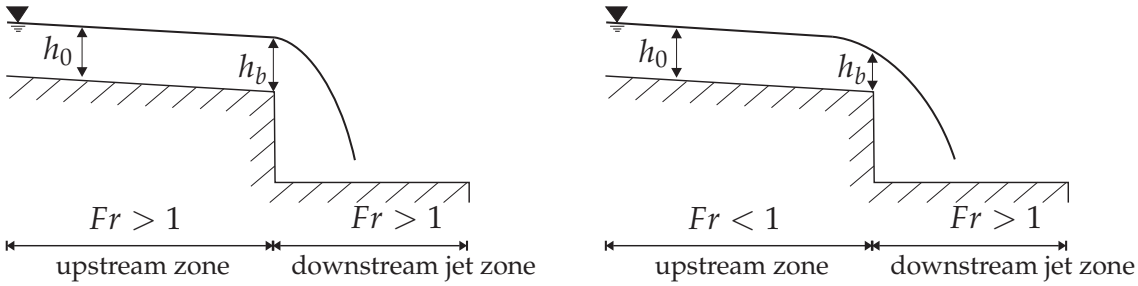

(a) Free overfall with supercritical flow in the upstream zone.

(b) Free overfall with subcritical flow in the upstream zone.

Figure 5.15.: Water depth at a brink depending on upstream flow conditions.

modelled in this work. Second, velocity and discharge of the approaching flow from the gutter are that high that it passes the drain grate (splash-over). In this case, a certain amount of water does not even enter the inlet. The ratio of intercepted flow q_{in} and approaching flow q_{approach} is defined as drainage efficiency

$$\varepsilon = \frac{q_{\text{in}}}{q_{\text{approach}}}. \tag{5.29}$$

Drainage efficiency varies with the type of inlet, the discharge from the gutter, flow velocity and longitudinal slope of the gutter. There are various types of inlets such as curb-opening inlets, grate-inlets and combinations of these. Therefore, implementing drainage efficiency in the Pavement Surface Runoff Model would require detailed experimental data for various inlet and gutter configurations. Since these are not available, drainage efficiency is implemented as factor ε, which can be adjusted by the user. In general it is set to 1.

Assuming $\varepsilon = 1$, flow into an inlet can be interpreted as a free overfall. It is the simplest case of a weir flow where the weir has zero height as shown in Figure 5.15. The brink divides the flow into the upstream zone (approaching flow) and into the downstream jet zone (flow behind the brink). Flow processes behind the brink are not investigated further. A free overfall implies that the upstream zone is not influenced by the downstream jet zone. This is a valid assumption as long as the drainage capacity of the inlet is not exceeded and no backwater effects occur. Therefore, disturbances can only be transmitted downstream. Consequently, flow in the downstream jet zone is always supercritical. Depending on the flow condition in the upstream zone two cases have to be considered, which are presented in Figure 5.15. Depending on the flow condition in the upstream zone, different water depths will set up at the brink. For supercritical flow in the upstream zone as shown in Figure 5.15a, flow conditions across the brink do not change and water depth at the brink h_b equals water depth in the upstream zone h_0. Thus, discharge can be simply

modelled as a free outflow condition. If flow in the upstream zone is subcritical as shown in Figure 5.15b, flow state changes to reach the supercritical state behind the brink. As a consequence, water depth at the brink will be smaller than in the upstream zone ($h_b \neq h_0$) and the flow will inevitably pass the critical state, which is characterised by $Fr = 1$. The water depth at the brink can be determined on the basis of the concept of critical flow. For the sake of simplicity it is assumed that the critical state will set up right at the brink. The concept of critical flow presented in the next paragraph assumes a hydrostatic pressure distribution and a uniform velocity distribution. Since the Shallow Water Equation is based on the same assumptions, the use of this concept is justifiable. It was also applied in [25]. Literature about the concept of critical flow, especially extended and generalised equations as well as historical review are presented in [22, 23] and [24].

According to the Bernoulli equation, the energy head E for a parallel streamline flow (hydrostatic pressure conditions) with uniform velocity distribution is defined as

$$E = h + \frac{u^2}{2g} \tag{5.30}$$

where h is the water depth respectively pressure head representing the amount of potential energy E_{pot} and $u^2/2g$ the velocity head representing the amount of kinetic energy E_{kin}. Equation (5.30) is derived for a single point not for a channel section. If a rectangular cross section is assumed Equation (5.30) can be reformulated to

$$E = h + \frac{q^2}{2gh^2}. \tag{5.31}$$

When expressed in terms of h, the equation becomes

$$h^3 - Eh^2 + \frac{q^2}{2g} = 0. \tag{5.32}$$

Therefore, the local water depth is a function of specific energy and unit discharge. Figures 5.16a and 5.16b show Equation (5.32) plotted for $E = \text{const}$ and $q = \text{const}$ respectively. It is obvious that for every given E and q there are two possible and physically correct solutions for h (besides the third negative solution). However, there exists one singularity solution for h when $E = E_{\text{min}}$ and $q = q_{\text{max}}$. This solution occurs at the critical depth h_c. For the critical state, $Fr = 1$ and therefore

$$u_c = \sqrt{gh_c}. \tag{5.33}$$

Inserting the expression for u_c into (5.30) yields

$$E = \frac{3}{2}h_c. \tag{5.34}$$

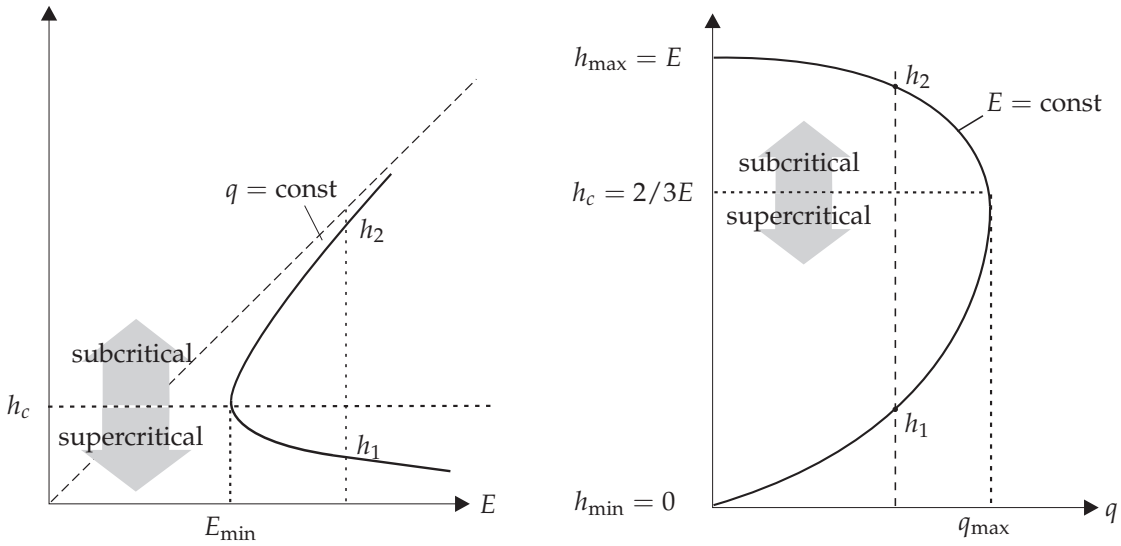

(a) Constant Discharge (b) Constant Energy

Figure 5.16.: Relation of water depth, discharge and energy.

The critical water depth h_c can therefore be determined depending on the specific energy (Equation (5.30)). The critical velocity follows from Equation (5.33).

In the Pavement Surface Runoff Model, inlets are cells which do not belong to the model domain. Instead, the interface between an inlet and a computational cell is treated as a boundary where the Neumann condition is applied. Depending on the Froude Number in the computational cell i, the Neumann flux into the inlet $\mathbf{F}_{\text{neu}}$ is defined as free flow condition ($Fr_i > 1$) or as critical flow condition ($Fr_i < 1$).

In case of a free flow condition, the conserved variables at the boundary are the same as in the cell ($\mathbf{U}_{\text{neu}} = \mathbf{U}_i$) and the flux reads:

$$\mathbf{F}_{\text{neu}}(\mathbf{U}_i) = \varepsilon \begin{pmatrix} hu \\ 0.5\,gh^2 + hu^2 \end{pmatrix}. \tag{5.35}$$

If the critical flow condition applies, the critical variables h_c and u_c are used ($\mathbf{U}_{\text{neu}} = U_c$) and the Neumann flux reads:

$$\mathbf{F}_{\text{neu}}(\mathbf{U}_c) = \varepsilon \begin{pmatrix} h_c u_c \\ 0.5\,g{h_c}^2 + h_c {u_c}^2 \end{pmatrix}. \tag{5.36}$$

If the velocity of the computational cell i is directed away from the inlet, $\mathbf{F}_{\text{neu}} = 0$.

Figure 5.17 shows the water level profiles at the steady state along a slab with a free overfall calculated with the Pavement Surface Runoff Model using Equations 5.35

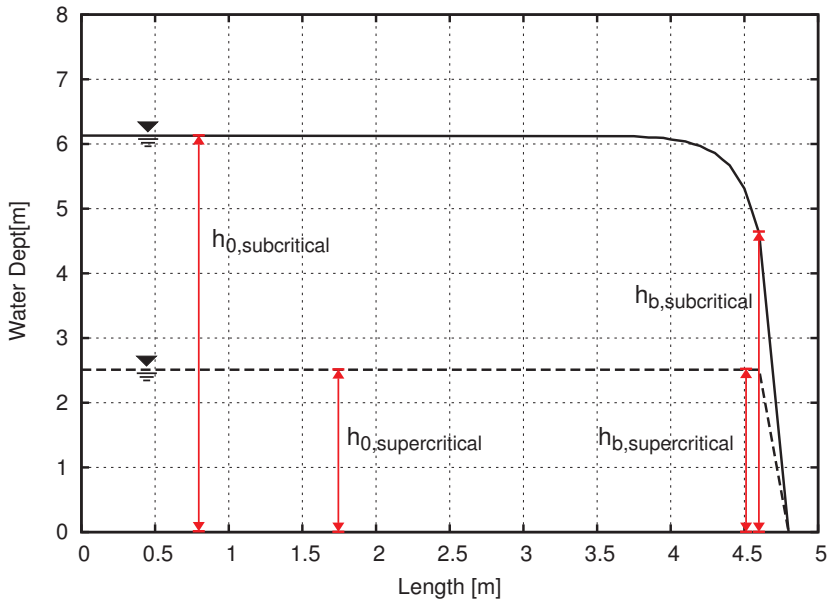

Figure 5.17.: Comparison of water depths near a brink for sub and supercritical flow conditions calculated with the Pavement Surface Runoff Model.

and 5.36. The brink is located at x = 4.5 m. The solid line represents the water level profile for subcritical flow conditions in the upstream zone whereas the dashed line represents the water level profile for supercritical flow conditions in the upstream zone. The profiles clearly exhibit the differences regarding the water depth at the brink h_b. For supercritical conditions in the upstream zone, water depth at the brink equals the water depth in the upstream zone ($h_0 = h_b$). For subcritical inflow conditions water depth at the brink is smaller ($h_0 > h_b$).

The concept of critical flow is one dimensional. For the application in two dimensional flow problems, the following assumptions are made. The Pavement Surface Runoff Model is developed for the use on a cartesian grid. Consequently, the boundaries to an inlet always coincide with one of the coordinate directions. If the flow variables are splitted into the coordinate directions, the fraction orthogonal to the boundary primarily influences the flow into the inlet. Therefore, the velocity component and the flow parallel to the brink are neglected. Thus, the energy head at the boundary E_{bound} is calculated as:

$$E_{\text{bound}} = \begin{pmatrix} u^2/2g \\ v^2/2g \end{pmatrix} \cdot \mathbf{n}_{\text{bound}} + h_i. \tag{5.37}$$

Using E_{kin} and E_{pot}, which remains unchanged in two space dimensions, the critical variables can be calculated according to Equations (5.34) and (5.33). In two dimen-

sions, flux into the inlet reads:

$$\mathbf{F}_{\text{neu}} = \varepsilon \begin{pmatrix} hu & hv \\ 0.5\,gh^2 + hu^2 & 0 \\ 0 & 0.5\,gh^2 + hv^2 \end{pmatrix} \cdot \mathbf{n} \tag{5.38}$$

Depending on the Froude Number the neumann flux is calculated as $\mathbf{F}_{\text{neu}}(\mathbf{U}_i)$ or $\mathbf{F}_{\text{neu}}(\mathbf{U}_c)$.

In this chapter, the Pavement Surface Runoff Model was set up by adding specific features to the Shallow Water Equations, which are needed to solve real pavement surface runoff flow problems. First, a method to import and process topographic point data was developed. It includes a boundary tracing algorithm on the basis of the graham scan algorithm. A modification of the algorithm enables the detection of convex boundaries. For the interpolation of the topographic data to the underlying grid, the inverse distance weighting algorithm was implemented. Second, an equation was developed to describe the Darcy-Weisbach resistance coefficient depending on the mean texture depth of a pavement surface. Since a rather theoretical estimation of the resistance coefficient assuming a logarithmic velocity distribution was rejected due to the flow characteristics and available data, a potential equation was fitted directly to the experimental data originating from [95]. The best coefficients of determination were obtained with a two parameter model including bottom slope and the texture related Froude Number Fr_k, which was derived from a dimensional analysis. Finally, a method was suggested to describe drainage facilities on the basis of the one dimensional critical flow theory. In the following chapter, the Pavement Surface Runoff Model is applied to various flow problems to demonstrate the features developed herein.

6. Model Application

In the preceeding chapters, the development of the Pavement Surface Runoff Model (PSRM) was described. The model is based on the depth-averaged Shallow Water Equations, which are discretised by a cell-centred finite-volume method on a cartesian grid. For the approximation of the intercell fluxes, the HLL approximate Riemann solver is used. Flow resistance is modelled with the Darcy-Weisbach equation. For the resistance coefficient, a potential equation depending on velocity and mean texture depth was developed and calibrated using the experimental data from [95]. Additional features of the model are its ability to import and process topographic data for a simulation on pavements with irregular topography and the simulation of drainage facilities.

Now, all the above mentioned parts, which were treated separately in the previous chapters, are put together and the Pavement Surface Runoff Model is applied to real world flow problems. The objective of the chapter is to present the spectrum of possible applications of the model. These include a model road section with drainage facilities, an existing road section with irregular topography as well as a road section designed in CAD with a complex boundary. At first, though, the Pavement Surface Runoff Model is compared to Planus, the model which was developed in [95].

6.1. Comparison with Planus

The simulation of water depths on surfaces with regular topography (parametrised surfaces) is the simplest case, which is covered by all pavement surface runoff models, either empirical or hydrodynamic, e. g. [25, 59, 68, 95]. However, the comparison of models is rather difficult since they are calibrated with different data and experiments are restricted to different conditions. In fact, Planus and the Pavement Surface Runoff Model were calibrated with the same data base. This offers the possibility to compare both models and to discuss differences and similarities. First of all, both model concepts are briefly summarised.

Planus is an empirical model, which considers the steady state equilibrium of bottom and friction slope along a flow path similar to a kinematic wave equation. The flow paths are determined from the surface topography as paths along the maximum bottom slope. Although the flow paths move in two dimensional space, the

flow is strictly limited to these flow paths and therefore, the model is quasi one dimensional. After the steady state water depth distribution on the flow paths is determined, water depths are interpolated between the flow paths to generate a two dimensional distribution. The flow parameters in Planus are combined in a potential function as follows:

$$h = c \cdot k^a \cdot q^b \cdot S_0^d. \tag{6.1}$$

In the equation, k is mean texture depth, S_0 bottom slope and q the discharge, which depends on flow path length and rainfall intensity. The coefficients a, b, c, and d are empirically determined. It can be seen from Equation (6.1) that the flow is solely generated by bottom slope, hence gravitational forces.

The Pavement Surface Runoff Model is a two dimensional, time dependent hydrodynamic model. In contrast to Planus, flow is not limited to the flow paths but can move in two dimensions. Therefore, water depth distributions are not interpolated but directly result from solving the Shallow Water Equations. Further on, the model considers the full dynamic wave equation including the time dependent change of momentum, the momentum flux, the horizontal pressure gradient as well as bottom and friction slope. Therefore, momentum and horizontal pressure gradient are additional driving forces for the flow besides bottom slope. In addition, all terms of the Shallow Water Equations are based on the physical law of conservation and apart from friction slope, they are all uniquely defined. The friction slope is the only term to be determined empirically.

The two models are compared on the basis of the water depth distribution in a basic superelevation transition as shown in Figure 6.1 and presented in Section 2.1.3. These are the most critical sections in the road alignment with respect to drainage. The chosen configuration is a superelevation transition within a 120 m long road section of a 6 lane divided motorway with a cross section RQ 36 according to German guidelines [41]. Modelled pavement width is $b = 14.5$ m since only one direction is considered. The superelevation transition is implemented according to the guidelines with a transition length of $L_V = 50$ m and a relative gradient of 0.1 a, which corresponds to 0.725 %. Superelevation respectively cross slope outside the transition zone is set to the minimum value of q_p = 2.5 %. Longitudinal slope is set to s = -2 %. Rainfall intensity is chosen to $i = 0.75$ mm/min. This corresponds to a rainfall event with a return period of n = 1 year and a duration of $t_r = 15$ min in the area around Stuttgart (see Section 2.1.1). The simulations are performed on a cartesian grid with 0.2 m x 0.2 m grid cells.

Three aspects are treated by the comparison:

- the maximum water depth
- the spatial distribution of water depths and
- the frequency distribution of water depths.

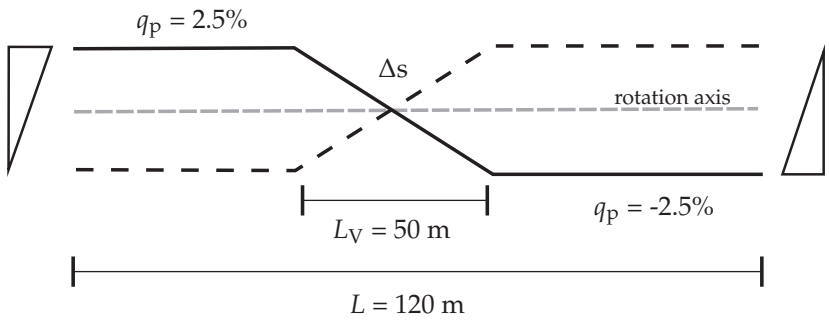

Figure 6.1.: Superelevation transition used for the comparison of the Pavement Surface Runoff Model and Planus.

The maximum water depth on a pavement is strongly influenced by the surface cover and its mean texture depth k. Five different surface covers are implemented in the models as presented in Section 5.2.1. These are: CJ (k = 0.4 mm), CAT (k = 0.84 mm), SMA08 (k = 0.89 mm), SMA011 (k = 0.98 mm) and DGA (k = 1.83 mm). Table 6.1 presents the maximum averaged water depths h and referenced water depths h_{ref} (defined in Section 5.2.1) for the different surface covers calculated for the example transition.

		CJ	CAT	SMA08	SMA011	DGA
Planus	h [mm]	2.5	3.6	3.8	4.0	5.2
PSRM	h [mm]	2.5	3.5	3.6	3.8	5.1
Planus	h_{ref} [mm]	2.1	2.8	2.9	3.0	3.4
PSRM	h_{ref} [mm]	2.1	2.6	2.7	2.8	3.3

Table 6.1.: Maximum averaged water depths h and referenced water depths h_{ref} for the basic superelevation transition with s = -2 % and variable surface covers.

Both models confirm the correlation of mean texture depth and maximum water depth. The higher mean texture depth, the higher is h and h_{ref} respectively. The maximum deviation of the water depths between the models is 0.2 mm what is neglectable. Besides flow resistance, water depths are also affected by the retention volume of the surface texture. This becomes visible when the arithmetic and referenced water depths are compared. The difference of h between the two surface covers CJ and DGA is 2.7 mm (Planus) and 2.6 mm (PSRM) and for h_{ref} it is only 1.3 mm (Planus) and 1.2 mm (PSRM). Therefore, a surface cover with high mean tex-

ture depth can partially compensate the increased flow resistance by an increased retention volume. However, this is only valid to a certain extent. Since $h_{ref} = h - k$ the effect of the retention volume is equally reproduced by both models.

Figures 6.2 to 6.6 show the spatial distribution of the referenced water depths h_{ref} for the example transition. The upper plot in each figure corresponds to the distribution calculated with the Pavement Surface Runoff Model, the lower plot is calculated with Planus.

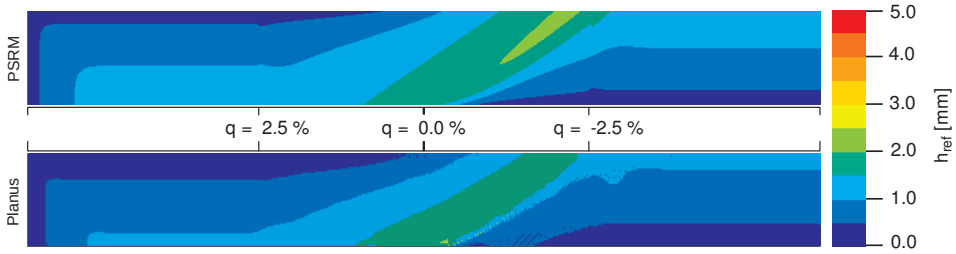

Figure 6.2.: Comparison of water depth distribution for surface cover CJ.

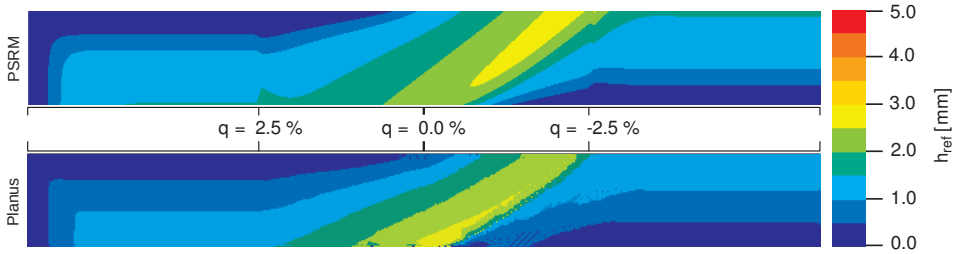

Figure 6.3.: Comparison of water depth distribution for surface cover CAT

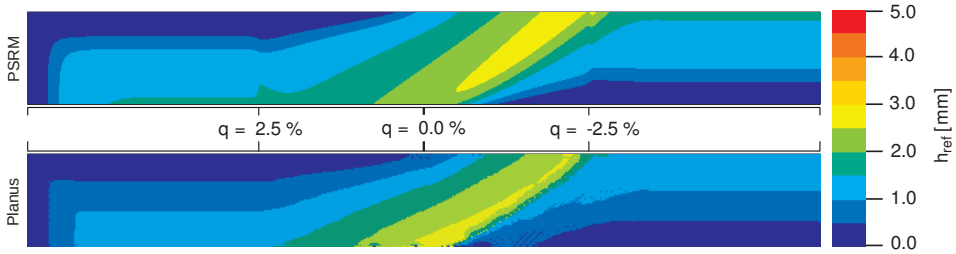

Figure 6.4.: Comparison of water depth distribution for surface cover SMA08

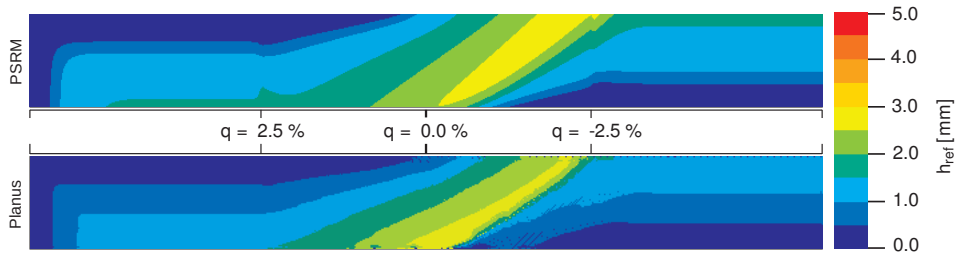

Figure 6.5.: Comparison of water depth distribution for surface cover SMA011.

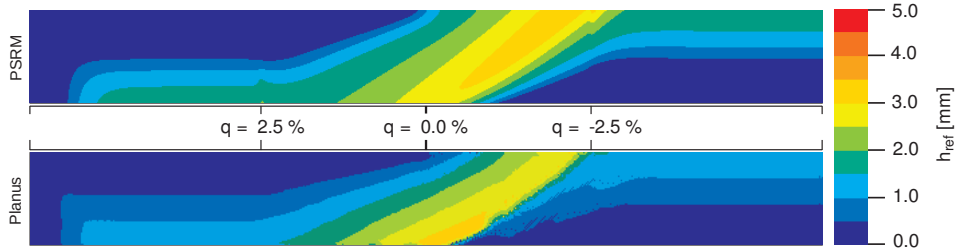

Figure 6.6.: Comparison of water depth distribution for surface cover DGA.

Both models show an accumulation of water in the transition zone next to the point of zero cross slope ($q = 0$ %). Since longitudinal slope is negative the accumulation is slightly shifted downwards (to the right). The range of water depths in the transition depends on the surface cover and is also nearly the same for both models. However, the location of the water accumulation differs what can be explained best referring to Figure 6.6. In Planus, the accumulation develops from the lower boundary of the plot whereas in the Pavement Surface Runoff Model it emanates from the upper boundary of the plot. Figure 6.7 shows again the water depth distribution for the DGA surface cover. Additionally, a qualitative sketch of the flow paths is added. The arrows indicate the direction of flow.

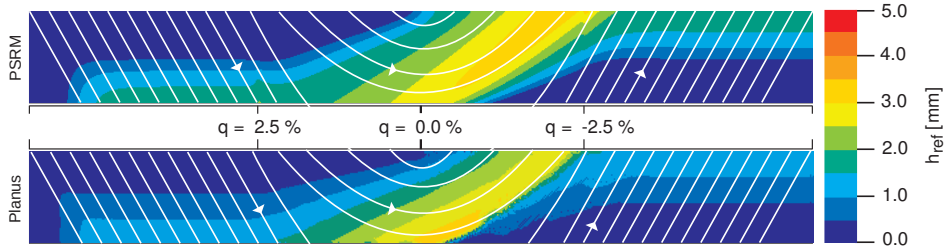

Figure 6.7.: Water depth distribution for surface cover DGA including qualitatively determined flow paths and flow directions.

The accumulation of water in the Pavement Surface Runoff Model emanates from the outflow boundary. This is consistent because the volume of water reaches its maximum near the outflow boundary as long as it is not decreased by an inlet or damed in a pit. In Planus though, the accumulation does not develop at the outflow boundary but at the turning point of the longest flow path. One explanation could be that the slope of the flow path at this point is very low. Furthermore, momentum and horizontal pressure gradient are neglected as driving forces. Since the model is one dimensional and water is forced to move on the given flow path, bottom slope significantly affects water depth. In the Pavement Surface Runoff Model, the two dimensional effects are preserved. Especially the consideration of momentum and pressure gradient avoid an accumulation of water at the lower boundary. This effect is emphasised if a transition with a longitudinal slope of $s = 0$ % is considered as shown in Figure 6.8. The flow paths are qualitatively sketched around the centre. Again, the water accumulation in Planus emanates from the turning points of the flow paths because there the slopes are very small. Right in the centre of the transition, a pond seems to develop. The model treats this location as a sag and water depth in the centre reaches up to $h_{\text{ref}} = 5$ mm. However, geometrically the centre is not a sag but a saddle point. If water depth in the centre reaches a certain depth momentum and pressure gradient should lead to a movement of water towards the boundary. This behaviour is observed in the Pavement Surface Runoff Model. As a result, water depth in the centre is only $h_{\text{ref}} = 3$ mm instead of 5 mm.

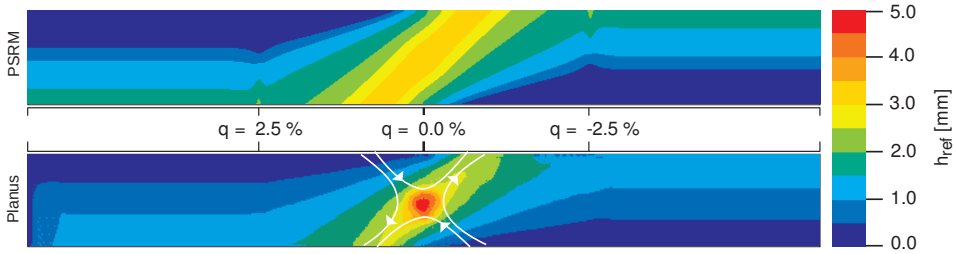

Figure 6.8.: Water depth distribution of a basic superelevation transition with s = 0 %.

Summarising it can be stated that the spatial distribution of water depths as well as the maximum water depth calculated with the two models is comparable as long as slopes are not too small. Then, momentum and pressure gradient as driving forces can be neglected. As soon as these forces become significant driving forces, Planus tends to create a distinct accumulation of water. In these cases, the Pavement Surface Runoff Model yields better results.

When looking at Figures 6.2 to 6.6 again, another difference in the models becomes visible, which was neglected so far. The Pavement Surface Runoff Model shows

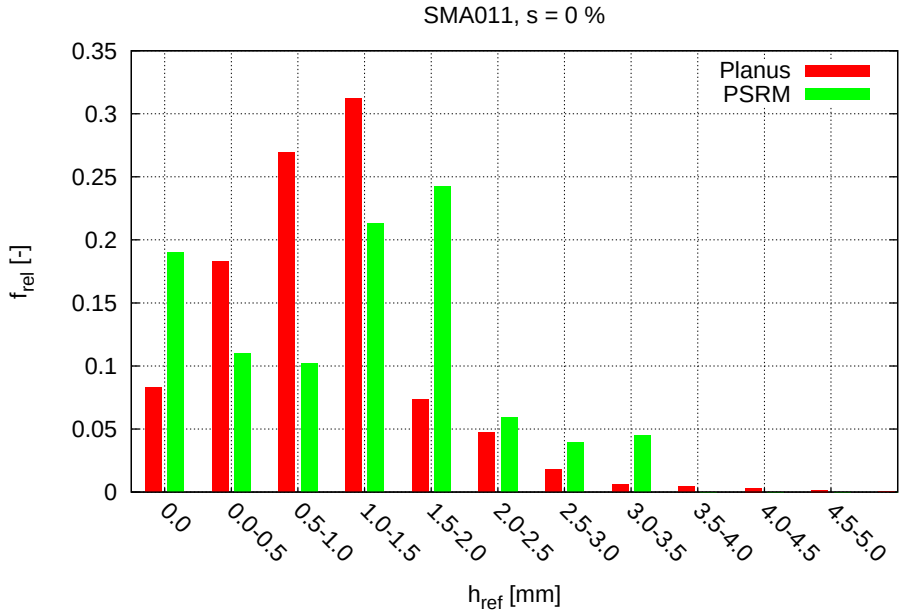

Figure 6.9.: Histogram of water depths in the example superelevation transition for SMA011 and s = 0 %).

slightly higher water depths at the boundaries. In Figure 6.6, water depth at the boundary is around 2.0 mm whereas Planus shows water depths around 1.5 mm. In addition, the increase of the water depths near the boundary is higher for the Pavement Surface Runoff Model than for Planus. This difference in water depth distribution can be very well illustrated when plotting the relative frequency curves (histogram) for the water depths calculated with both models. Data is divided in 11 frequency classes ranging from 0 to 5.0 mm. The first class only includes h_{ref} = 0 mm. Note that h_{ref} = 0.0 mm does not mean that there is no water on the pavement but that $h < k$. The histograms are plotted for the example transition with longitudinal slopes s = 0 %, 2 %, and 4 % and for all surface covers. Since the general trend is similar for all surfaces, the plots for SMA011 are exemplary presented herein. The histograms for the remaining surface covers can be found in the appendix (A.2).

Figures 6.9 to 6.11 show the histograms for the SMA011 surface cover and the three longitudinal slopes. The following aspects are observed when looking at the frequency distributions. First, in Planus, the relative frequency f_{rel} of water depths increases almost steadily from h_{ref} = 0 until h_{ref} = 1.5 mm. In contrast, frequencies of the Pavement Surface Runoff Model tend to increase exponentially. Second, results of the Pavement Surface Runoff Model exhibit a larger fraction h_{ref} = 0.0 mm ('dry fraction'). The water depth range $h_{ref} < 1.5$ mm is mainly present in the pavement section outside the superelevation transition. Here, bottom and cross slope are constant. One explanation for the different behaviour of the models in this range can

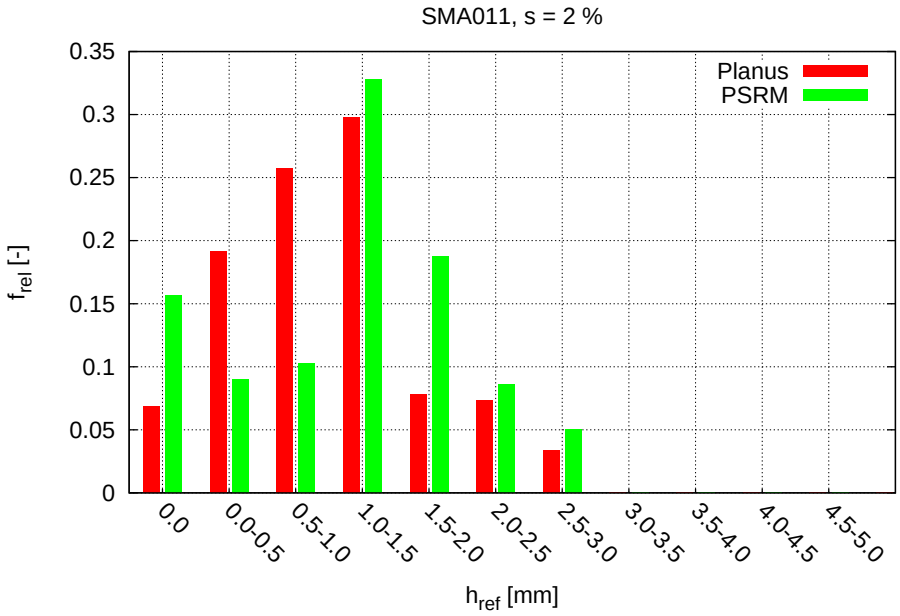

Figure 6.10.: Histogram of water depths in the example superelevation transition for SMA011 and s = 2 %).

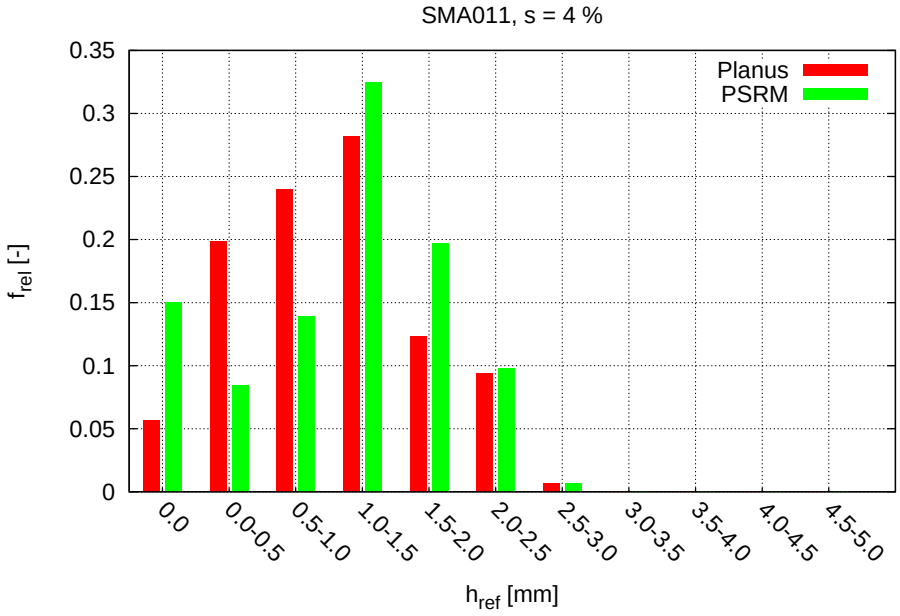

Figure 6.11.: Histogram of water depths in the example superelevation transition for SMA011 and s = 4 %).

be the flow resistance model. In Planus (Equation (6.1)), flow resistance is modelled as a constant. Besides flow resistance, water depth depends on bottom slope, flow path length and rainfall intensity. Bottom slope is constant outside the superelevation transition and rain intensity is also constant for the simulation. Therefore, flow path length is the only varying parameter. This leads to the almost linear behaviour. In the Pavement Surface Runoff Model, the flow resistance equation and the resistance coefficient are non-linear because they depend on velocity. Furthermore, the Shallow Water Equation itself is a non-linear equation. This, in turn, can explain the non-linear increase of water depths. Third, In the range of $h_{\text{ref}} > 1.5$ mm, the Pavement Surface Runoff Model shows higher frequencies than Planus but the decrease of frequencies is also non-linear. Frequencies of Planus, however, significantly drop in comparison to the lower range. After the drop, they also decrease non-linearly but as already discussed above, Planus tends to create distinct accumulations of water for $s = 0$ %. In these cases, maximum water depth calculated with Planus is significantly higher than for the Pavement Surface Runoff Model. The non-linear decrease of frequencies can be explained as follows. In contrast to the lower range of water depths, the range of $h_{\text{ref}} > 1.5$ mm is mainly related to the superelevation transition. Here, bottom and cross slope are not constant. Consequently, the flow path length is not the only variable factor determining water depth. The significant drop of frequencies in Planus shows that accumulations of water within the transition zone are locally bounded. Maybe this is due to the fact that the one dimensional approach does not allow water moving between the flow paths. Additionally, flow velocity in sections with small longitudinal slope is small what also evokes accumulations.

The comparison shows that both models yield the same maximum water depth. However, the spatial and frequency distribution of water depths differ. The fraction of water depths above 1.5 mm is bigger in the Pavement Surface Runoff Model than in Planus. In contrast, the Pavement Surface Runoff Model exhibits smaller fractions in the lower range. Furthermore, the accumulations of water develop from different locations in the transition. In Planus, they develop from the turning point of the longest flow path whereas in the Pavement Surface Runoff Model they develop from the outflow boundary. Reasons for that are due to the different model concepts. The Pavement Surface Runoff Model is two dimensional and considers momentum and horizontal pressure gradient as additional driving forces besides bottom slope. Therefore, it yields more reasonable results in the presence of small slopes.

6.2. Drainage

Modelling drainage facilities is a substantial element in an integrated simulation of pavement surface runoff. In the following, a road section is considered which

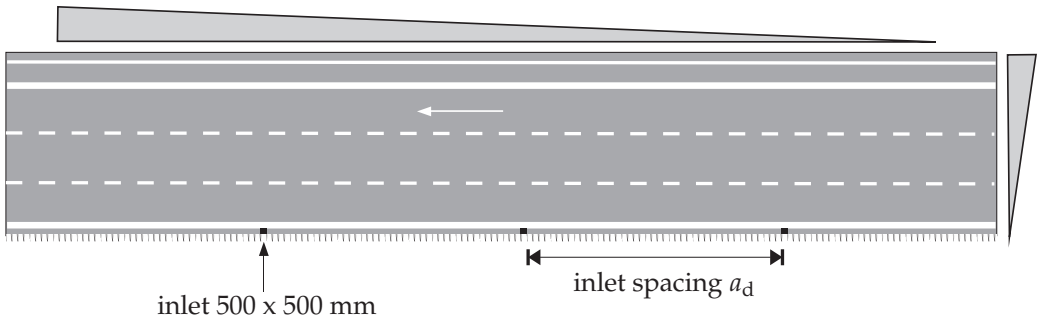

Figure 6.12.: Sketch of the modelled road section.

drains to the median as shown in Figure 6.12. The median is constructed as a curb and constitutes a closed boundary. This configuration can be a serious safety risk because surface runoff accumulates at the median right beside the lane of fast traffic. If accumulations extend to the lane, the hydroplaning risk will increase drastically. Therefore, inlets are placed along the curb to prevent water from extending to the lane. The simulation of closed boundaries in combination with inlets is an exclusive feature of the Pavement Surface Runoff Model. Therefore, a comparison with Planus is not possible.

The modelled roadway section is sketched in Figure 6.12. The pavement is 14.5 m in width and belongs to a 6 lane motorway with a dual carriageway and a cross section RQ 36 according to [41]. Driving direction is indicated by the white arrow. Longitudinal slope $s = 2.0$ % and cross slope $q_p = 2.5$ % are both constant. Inlets are placed at fixed spacings a_d and are assumed to have a size of 500 x 500 mm. According to the German road drainage guidelines (RAS-Ew, [40]) the cross section close to the curb can be constructed in two ways:

- forming a simple channel with the same cross slope q_p as the roadway shown in Figure 6.13a, or
- forming an inclined channel with a higher cross slope than the roadway ($q_{p,1} > q_{p,2}$) as shown Figure 6.13b.

The spacing a_d of the inlets is designed depending on the desired maximum water level width b_w at the curb. In the guidelines, the design is done with a one dimensional open-channel flow equation. Runoff from the pavement is treated as lateral inflow into the channel. Velocity and direction of the inflow are not considered. Flow resistance is modelled using the equation of Manning-Strickler with a resistance coefficient $k_{Str} = 70$. In the following, variable spacings and the corresponding water level widths as determined by the guidelines are compared to the results of the Pavement Surface Runoff Model. To guarantee similar conditions, the Manning equation (Equation (3.59)) is used to describe flow resistance in the Pavement Surface Runoff Model. The Manning coefficient can be derived from the Strickler

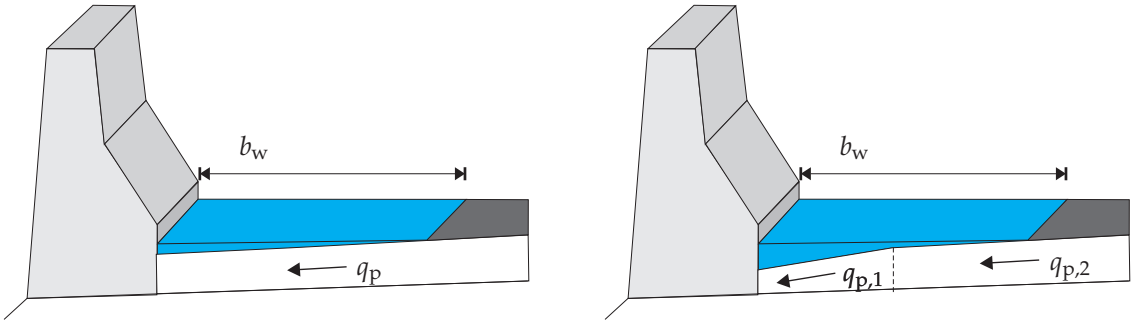

(a) Simple channel (b) Inclined channel

Figure 6.13.: Channel geometries near the curb.

Figure 6.14.: Two dimensional water depth distribution for the modelled road section with a_d = 39 m calculated with the Pavement Surface Runoff Model.

coefficient by $n = 1/k_{Str}$. Rain intensity is $i = 0.75$ mm/min, assuming a drainage efficiency of 100 % ($\varepsilon = 1$). The simulation is performed on a cartesian grid with grid cells of size 0.25 x 0.25 m.

Before the water level widths for various configurations are compared, the two dimensional water depth distribution calculated with the Pavement Surface Runoff Model for an inlet spacing a_d = 15 m and a simple channel is exemplary shown in Figure 6.14. The effect of the inlets becomes clearly visible in the plot. Water accumulates at the curb and water depth as well as water level width increase towards the inlet. Since a drainage efficiency of 100 % is assumed, water is totally removed by the inlet and no water is conveyed to the next section. The inlet is further on sufficient to prevent water level width reaching the marking of the fast traffic lane. Table 6.2 summarises the water level widths for a simple channel calculated according to the guidelines and with the Pavement Surface Runoff Model for the spacings a_d = 6 m , 15 m and 35 m. The water level widths calculated with the Pavement Surface Runoff Model are consistently smaller than those determined by the guidelines. The difference between the water level widths increases with increasing inlet spacing. Since a drainage efficiency of 100 % is assumed and the water level widths are smaller, the velocity in the channel must be higher in the two dimensional Pavement

a_{d}[m]	6	15	39
$b_{w,\text{RAS-Ew}}$	0.50	0.70	1.00
$b_{w,\text{PSRM}}$	0.45	0.65	0.90

Table 6.2.: Water level widths calculated according to [40] and with the Pavement Surface Runoff Model for a simple channel.

a_{d} [m]	63	135
$b_{w,\text{RAS-Ew}}$	0.50	0.70
$b_{w,\text{PSRM}}$	0.50	0.68

Table 6.3.: Water level widths calculated according to [40] and with Pavement Surface Runoff Model for an inclined channel with $b_c = b_w$.

Surface Runoff Model. One explanation can be that the Pavement Surface Runoff Model simulates the two dimensional flow on the entire pavement and therefore also considers the direction and velocity of the lateral inflow. In the one dimensional open-channel equation inflow is just quantitatively added as source term along the channel. Another explanation might be that the two dimensional model considers momentum, which constitutes an additional force in downslope direction. In the open-channel equation, bottom slope is the only driving force.

Table 6.3 summarises the results for an inclined channel with a cross slope of 10 %. The channel width b_{c} is identical to the desired maximum water level width b_{w}. In contrast to the simple channel the water level widths calculated with the models are the same for a_{d} = 63 m and differ only slightly for a_{d} = 135 m. Therefore, two dimensional effects do not seem to be as strong as for the simple channel. Due to the significant inclination of the channel, flow in the channel is influenced less from the flow on the pavement and therefore flow behaviour has a more distinct one dimensional character. In this case, the one dimensional open-channel flow equation is a better approximation than for a simple channel.

A shortcoming of the one dimensional approach is, however, that it can not cope with an overflowing channel. It has been mentioned already that for an inclined channel the guidelines assume the channel width to equal the desired maximum water level width ($b_{\mathrm{c}} = b_{\mathrm{w}}$). Consequently, the guidelines always assume the channel running full. The resulting water level width in case of an overflow can not be determined since this would presume the capability of the model to deal with variable cross sections. For the determination of the inlet spacings for a new road

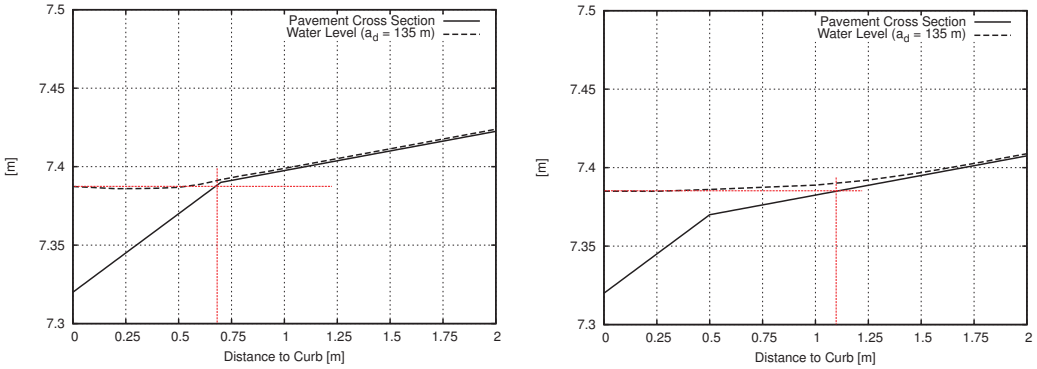

(a) Channel width = 0.7 m (b) Channel width = 0.5 m

Figure 6.15.: Width of water level for a drainage spacing of 135 m and variable channel widths.

design, the assumption $b_c = b_w$ is adequate since the channel width should be designed depending on the worst case. If existing road sections are modelled though, the feature of describing an overflowing channel is indispensable. In the Pavement Surface Runoff Model this effect can be represented. Figure 6.15a shows the water level width for a spacing of a_d = 135 m calculated with the Pavement Surface Runoff Model. The channel width is chosen according to the guidelines to be b_c = 0.7 m and consequently also b_w = 0.7 m. Figure 6.15b, in contrast, shows the water level width for the same inlet spacing a_d = 135 m but for a decreased channel width b_c = 0.5 m. For this configuration, the channel capacity is not sufficient and the channel is overflowing. The resulting water level width is $b_w = 1.1$ m and would probably reach the fast traffic lane.

Finally, three conclusions can be drawn from the example. First, the results of the Pavement Surface Runoff Model and the guidelines are very well comparable, what confirms the Pavement Surface Runoff Model to a certain extent. Second, the Pavement Surface Runoff Model considers the entire pavement and is therefore able to model the whole two dimensional runoff process. In case of a simple channel two dimensional effects such as the direction and velocity of the lateral inflow have proven to be significant when determining the resulting water level width. Since water level widths calculated with the one dimensional approach are larger than those determined by the two dimensional model, they constitute the 'worser' case. Thus, the findings do not have negative influence on the existing guidelines. Third, the Pavement Surface Runoff Model offers the possibility to simulate channels with a variable cross section as well as overflowing channels. This feature is especially important when existing road sections are investigated.

6.3. Analysis of an Existing Road Section

If existing road sections are evaluated three additional aspects have to be considered in comparison to parametrised road sections as covered in the preceeding sections:

- Alignment parameters are usually not known. Therefore, the topography can not be described by a mathematical function. Furthermore, one is interested in modelling the real surface including deformations due to traffic loading. Consequently, the topography has to be measured and reconstructed in the model.
- The domain to be modelled can not be represented as a rectangle since the measured topography includes the curvature of the horizontal alignment.
- Surface covers vary spatially and may not correspond to the ones used in the experiments to calibrate the resistance model. therefore, a model should be able to handle varying surface covers in the model domain. In addition, the flow resistance model should provide the possibility to simulate surface covers with arbitrary texture depths.

To the authors knowledge, there is no pavement surface runoff model which can handle all these aspects without limitation. The reasons are described referring to the both recently developed models. The model developed in [25] is not adjusted to process and simulate on irregular topographic data, although the underlying diffusion wave equation could handle it correctly. Furthermore, the empirical coefficient of the resistance model was determined for each surface cover separately. Consequently, the resistance model can not be used to simulate surface covers which were not experimentally investigated. In [56], Planus was enhanced to process point clouds and to do simulations on irregular topography. However, determining the flow paths on the irregular topography is not trivial. They may start or end inside the model domain. This makes the algorithm unstable and strongly depending on input parameters for the flow path generation. Further, flow over adverse slopes and ponding can not be adequately described by a the model where the only driving force is bottom slope. If the model equation of Planus is recalled (Equation (6.1)), setting $S_0 = 0$ leads to an infinite water depth since the exponent is negative. Hence, the flow equation can not be solved for $S_0 = 0$. In most cases, the slope of the flow paths is not zero. Then, the model can be applied as far as flow paths are generated adequately. However, the model is limited to the restriction $S_0 \neq 0$. Due to its hydrodynamic nature and the consideration of the full dynamic wave equation, the Pavement Surface Runoff Model can be applied easily to irregular topographies. The flow resistance equation developed in Section 5.2.3 also allows the use of arbitrary mean texture depths.

The import and processing of topographic data as well as the simulation of the water depth distribution on the reconstructed surface with variable surface covers is illus-

Figure 6.16.: Aerial picture of the example road section [71].

trated for a section which was also considered in [56]. This section is chosen because the alignment parameters were determined from the point cloud therein. This offers the possibility to compare the results for the irregular pavement surface and the regular, parametrised surface. The example road section is part of the Federal Highway A8. It is situated between km 171.000 and km 170.000 and designed as a six lane dual carriageway. Lidar measurement data is available for the carriageway in driving direction Stuttgart-Munich. Figure 6.16 shows an aerial picture of the section. The different colours of the wearing course indicate different surface covers. The pale areas correspond to concrete with a jute fibre texture (CJ) whereas the darker areas correspond to stone matrix asphalt (SMA011). The varying surface covers are considered in the simulation. Figure 6.17 presents the parameters of the vertical alignment (top) and the cross section design (bottom) as determined from the lidar data in [56]. They are used as input for the parametrised version of the transition zone into the Pavement Surface Runoff Model. The vertical alignment consists of a sag curve between km 170.259 and 170.840 connecting the two grades $s_1 = -1.59$ % and $s_2 = 2.81$ %. The sag curve parameter is determined to be H = 13187 m and the tangent length T = 290.1 m. The cross section design includes a superelevation transition between km 170.207 and km 170.361 with the cross slopes q_1 = 2.36 % and q_2 = 3.49 %. The length of the transition zone is 154 m and the location of zero cross slope is identified at km 170.266. The resulting relative gradient of the transition is $ds = 0.2754$ %, which falls well below the minimum of ds = 0.725 % required by the guidelines [41]. To reconstruct the real surface the point cloud resulting from the measurements is imported into the Pavement Surface Runoff Model. The routine to determine the boundary polygon and the interpolation of the topographic data with the inverse distance weighting algorithm were described in Section 5.1.1 and Section 5.1.2. The cartesian simulation grid consists of cells with size of 0.2 x 0.2 m.

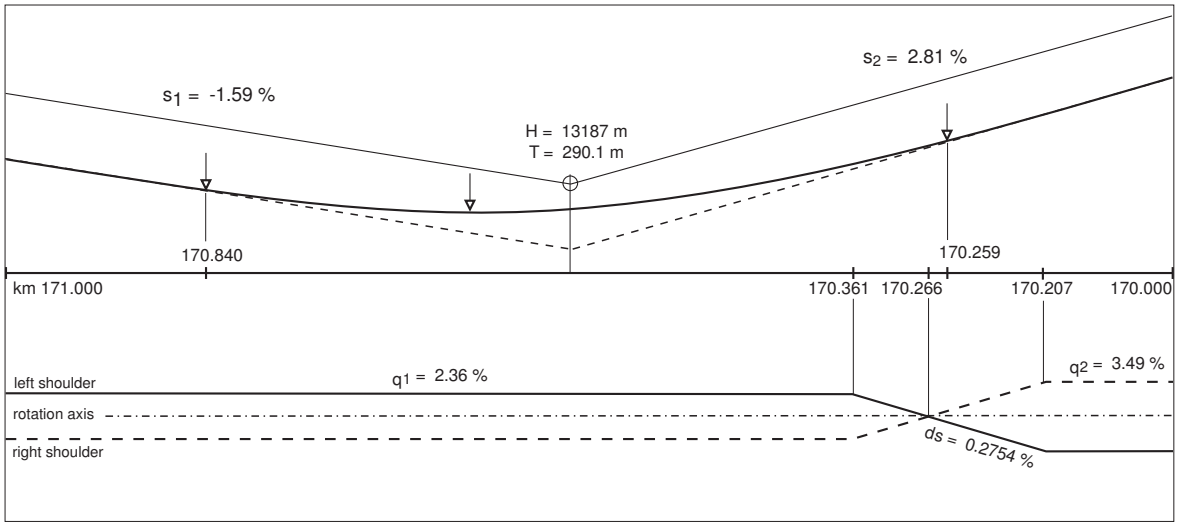

Figure 6.17.: Vertical alignment (top) and superelevation design (bottom) of the example road section.

Both configurations, irregular topography and parametrised surface, are simulated with a rainfall intensity $i = 0.75$ mm/min and a free flow boundary condition at all domain boundaries.

Figure 6.18 presents the elevation plots and the steady state water depth distributions for the parametrised surface (top) and the real surface (bottom). In addition, the variable surface covers are indicated. First of all, it can be stated that the boundary of the real surface is well defined when comparing it to the aerial picture in Figure 6.16. On a large scale, there are also no significant differences in the two elevation plots. The sag curve and the superelevation transition can be easily verified from the plots. The general trend of the water depths is also similar for both surfaces. For example, water depths increase for the SMA011 surface cover and, of course, near the centre of the superelevation transition. However, water depths on the irregular surface reach higher values and vary stronger than those on the parametrised surface. Obviously, this is due to the deformations in the surface, which give rise to accumulations of water. For the irregular topography, a water accumulation is observed within the SMA011 surface cover right at the boundary. This accumulation can be a result of the low longitudinal slopes in this section, which is right beside the low point of the sag curve. For the parametrised surface, this accumulation can not be detected though. Another explanation would be the irregular topography. If the boundary cells have a lower or even adverse bottom slope in comparison to the cells in the model domain, flow retards and water depth increases, although there is not necessarily a depression.

Figure 6.19 shows the water depth distribution in the transition zone for the example with the real topography. Obviously, deformations of the pavement surface have a

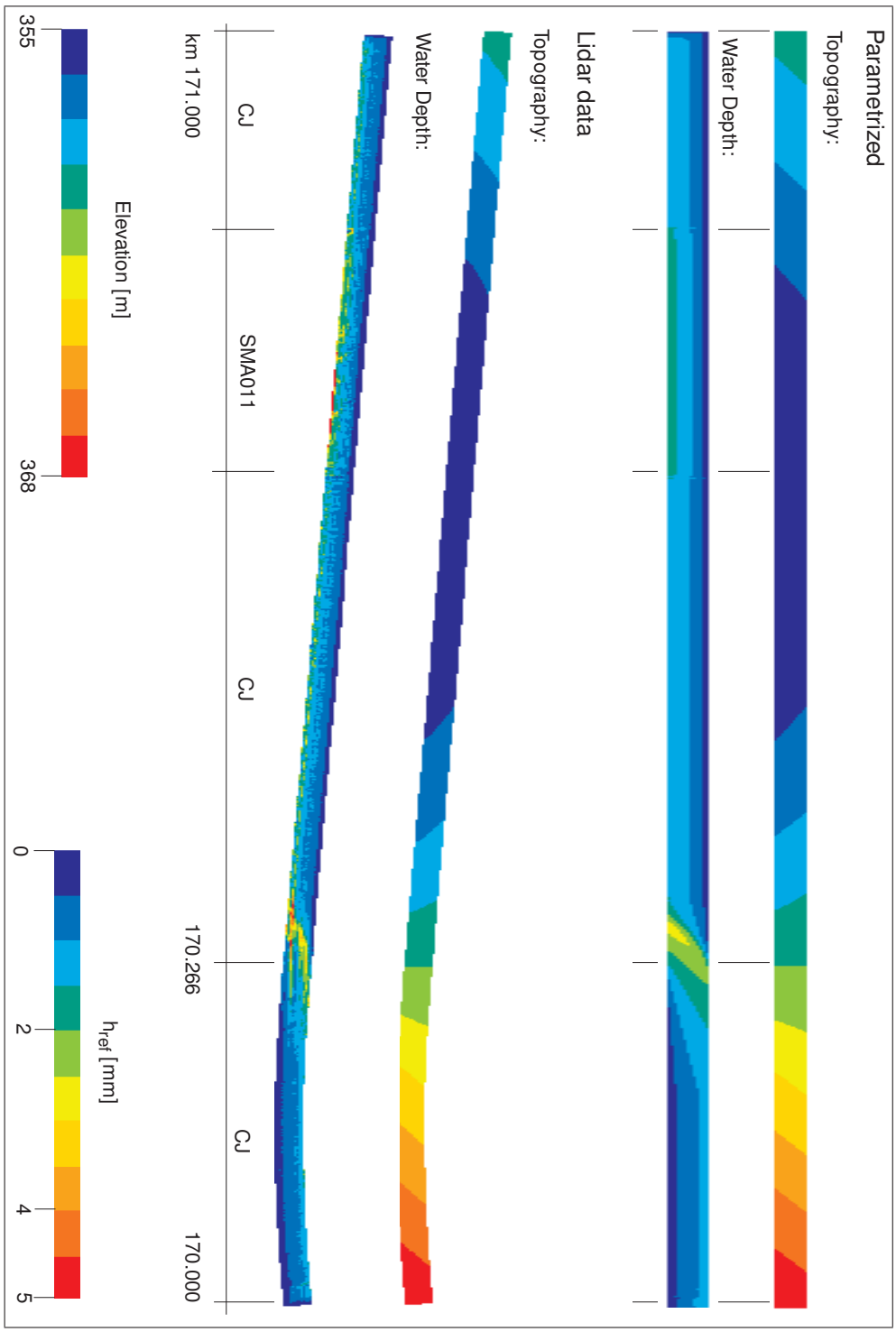

Figure 6.18.: Comparison of the water depth distribution of the example road section for the parametrised and real topography calculated with the Pavement Surface Runoff Model.

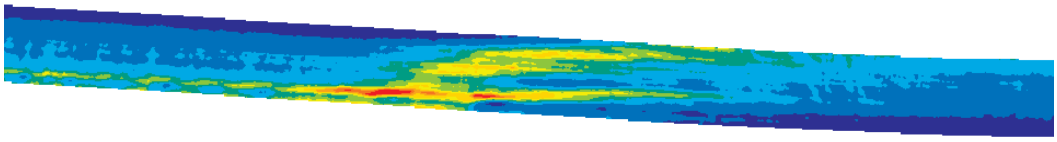

Figure 6.19.: Water depth distribution in the transition zone for the real topography calculated with the Pavement Surface Runoff Model.

bigger effect in the transition zone near the point of zero cross slope than outside. This can be explained by the fact that cross slope in the transition zone is very low and therefore the effective depth of a deformation is bigger than for a section with higher cross slopes. Consequently, unevenness of the pavement, especially in the form of ruts, carries a higher risk in terms of drainage in transition zones than in other road sections.

The example shows that the Pavement Surface Runoff Model easily handles irregular topographies and that the boundary tracing algorithm developed in this work detects the non-rectangular boundary. The results of the water depth distribution are very well comparable to the parametrised surface. Further on, the variable surface covers are represented adequately. Due to general resistance equation, surface covers with arbitrary mean texture depth can be approximatively simulated. This is very important when examining existing road sections.

6.4. Analysis of a Designed Road Section

Importing topographic data is not only required when lidar measurement data are to be processed. For road designs with several alignment elements, variable pavement widths or the design of intersections, the parametrisation of the surface is very complex and time consuming. Thus, the import of point data form a CAD software is preferred to the implementation of a parametrised surface. Due to its complexity, an intersection is chosen exemplary to demonstrate this feature of the Pavement Surface Runoff Model.

The example intersection was designed within the software tool VESTRA CAD. First, the underlying digital elevation model is converted into a set of raster points, which can then be imported into the Pavement Surface Runoff Model. In case of an intersection, the boundary polygon has a strong curvature. Therefore, it is determined within the CAD tool and exported independently as point set to the Pavement Surface Runoff Model. As discussed in Section 5.1.1, the developed boundary tracing method is limited to $\varphi_{boundary} > 120°$. The detection of the boundary polygon within the Pavement Surface Runoff Model is thus omitted. For a comparison of

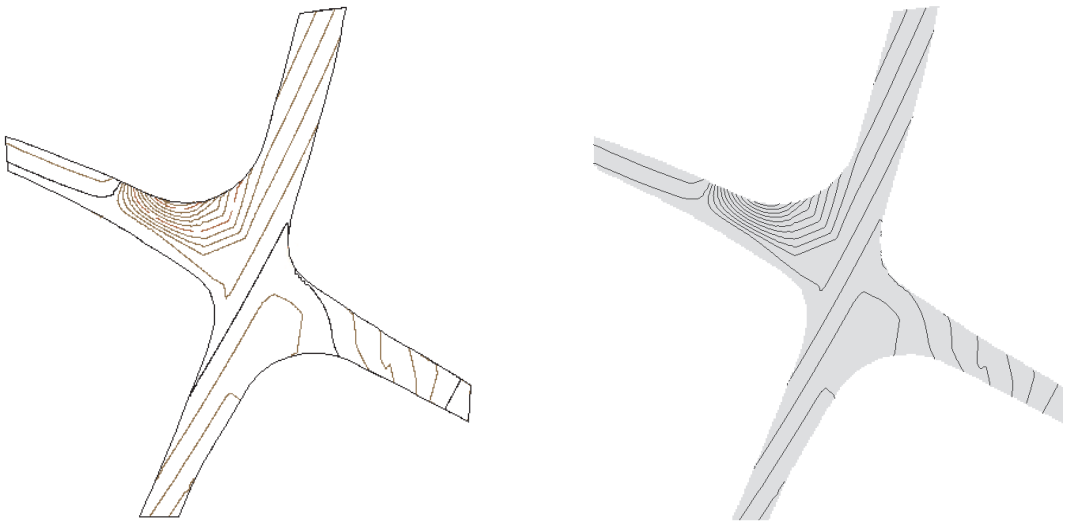

(a) CAD (b) Pavement Surface Runoff Model

Figure 6.20.: Elevation contour lines determined in CAD and with the Pavement Surface Runoff Model for the example intersection.

the reconstruction, the pavement surface is additionally reconstructed in VESTRA. Figure 6.20 presents the elevation contour lines calculated with CAD and the Pavement Surface Runoff Model. There is a very good agreement with respect to the elevation as well as the boundary of the domain.

Since the geometry of an intersection is very complex due to variable longitudinal and cross slopes drainage capability should be checked during the design process. For this purpose, VESTRA offers the possibility to determine flow paths on the basis of the contour lines. Flow paths are paths along the maximum gradient and are therefore strictly orthogonal to the elevation contour lines. The flow paths determined in VESTRA are shown in Figure 6.21. When looking at the flow paths four neuralgic points in terms of drainage can be identified for the intersection. They are indicated with circles numbered from 1 to 4. In circles number 1,2 and 4 drainage paths end within the domain. This signalises that water is not carried to the boundary but accumulates on the pavement. In circle number 3, drainage paths reach the boundary but they happen to merge. This indicates that due to strongly varying topography channels form where the water accumulates and is transported to the domain boundary. Figure 6.21 presents the two dimensional water depth distribution calculated with the Pavement Surface Runoff Model on a cartesian grid with cells of size 0.2 m x 0.2 m. The four neuralgic points can easily be verified in the plot. Especially locations 1 and 2 can be clearly identified as an accumulation of water. In contrast to the analysis using drainage paths, the Pavement Surface Runoff Model yields the corresponding two dimensional water depth distribution and allows to analyse the water depth distribution quantitatively. Further on, it enables to anal-

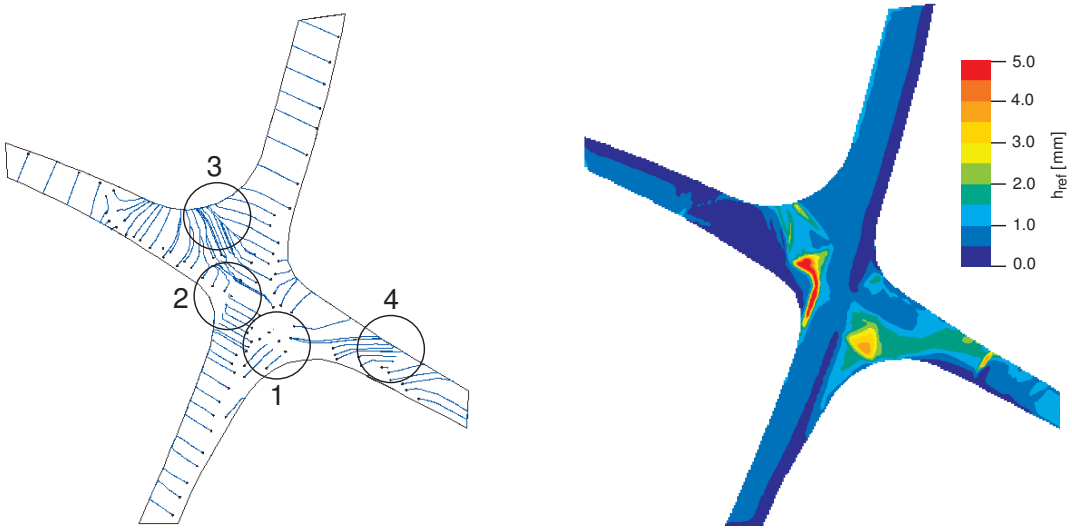

(a) CAD (b) Pavement Surface Runoff Model

Figure 6.21.: Drainage paths and water depth distribution for the example intersection.

yse the drainage capability of the intersection applying different rainfall intensities or surface covers. Additionally, the effect of drainage facilities could be simulated.

The examples presented in this chapter show the big spectrum of applications provided by the Pavement Surface Runoff Model. At the same time they demarcate it from existing models. The comparison with the empirical model Planus emphasises that a quasi one dimensional treatment of pavement surface runoff does not always yield appropriate results. Especially in presence of small bottom slopes, the two dimensional effects and the consideration of momentum and pressure gradient can not be ignored. Further on, the Pavement Surface Runoff Model enables an easy simulation of water depths on irregular topographies and varying surface covers. By the routines developed in this work, an import and processing of point clouds even with complex boundaries is achieved. At last, the model is also able to represent drainage facilities in the form of inlets or gutters. Summarising, it can be stated that the Pavement Surface Runoff Model is, so far, the first model which combines all features necessary for an integral simulation of pavement surface runoff.

7. Final Remarks

7.1. Summary

In this work, the Pavement Surface Runoff Model, a two dimensional and time-dependent model for the simulation of pavement surface runoff was developed. Unlike the various existing models, it should enable an integral simulation of pavement surface runoff. This includes features like the treatment of an irregular topography, the possibility to treat different surface textures and the consideration of drainage facilities. Generally, models can be empirically or physically motivated. The problem with empirical models is that they are closed-systems, which strongly depend on the boundary conditions of the underlying experiments. Therefore, the range of of application of empirical models is often restricted and their extension is difficult. For this reason, a physically motivated approach was chosen, namely on the basis of the depth-averaged Shallow Water Equations.

At first, pavement surface runoff was characterised. This included the hydraulic characterisation of the flow and the definition of the relevant factors influencing pavement surface runoff. Only the most relevant factors were considered in the model. These are: rainfall, bottom topography and flow resistance, which is mainly induced by the pavement's surface texture. Hydraulically, pavement surface runoff was characterised as a time-dependent and gradually varied free surface flow. Although experimental data showed that the flow covers the entire flow regime from laminar to turbulent, the laminar and transitional flow regime significantly prevail. Therefore, the explicit modelling of turbulence effects was abandoned. Another important characteristic of pavement surface runoff is its small flow depth in comparison to the horizontal scale. Consequently, the vertical change of the horizontal velocity components is very small. In addition, the bottom topography of a pavement is dominated by rather gentle slopes. For these reasons, vertical velocity components are neglible. These facts suggested the use of a depth-averaged, two dimensional model.

On the basis of the characterisation of the flow, in a second step, the mathematical model was set up. An equation describing depth-averaged free surface flows are the two dimensional or depth-averaged Shallow Water Equations. Starting from the most general conservation law, which was derived using the Reynolds Transport

Theorem, the derivation of the depth-averaged Shallow Water Equations was presented via the Navier-Stokes and Incompressible Euler Equations. Finally, the mathematical model could be defined as the depth-averaged Shallow Water Equations including source terms for rainfall, bottom topography and flow resistance. Subsequently, the model was characterised mathematically since this exerts great influence on the numerical method used. The Shallow Water Equations constitute a system of three partial differential equations. Special to the equations is their non-linear, hyperbolic behaviour which allows discontinuous solutions although the equations themselves are continuous. By the help of the Riemann problem, solution strategies for discontinuous initial value problems were presented.

In a third step, the numerical model to solve the Shallow Water Equations within a finite volume method was established. For reasons of simplicity, space discretisation was done with a cell centred scheme. The finite volume method was chosen because it is based on the integral form of the conservation law and therefore the discretisation itself is also conservative. Furthermore, the method allows discontinuous solutions. Two aspects were emphasised in the discretisation process: the approximation of the intercell fluxes and the discretisation of the source terms. For the calculation of the intercell fluxes the HLL approximate Riemann solver was chosen. Approximate Riemann solvers are developed for solving hyperbolic equations. They are based on an approximate solution of the Riemann problem mentioned in the previous paragraph. The HLL solver is the simplest of the approximate Riemann solvers but was considered to be sufficient. The source term discretisation focused on the flow resistance source term. Due to the small flow depths and high resistance coefficients, this term can easily evoke numerical instabilities. Therefore, the equations were splitted into an explicit and implicit part by the help of an operator-splitting technique, where the implicit part solely consists of the flow resistance source term. An implicit treatment of the flow resistance source term enables a stable solution process.

In a fourth step, the numerical model was adapted to the description of real pavement surface runoff problems. This includes the import of topographic point data to represent irregular pavement topographies, the development of a flow resistance model depending on available surface texture parameters and the modelling of drainage facilities:

- The import of topographic data is based on two algorithms, one to define the boundary polygon of the point cloud and one for the interpolation of the point data to the simulation grid. Computational geometry offers various methods to define the boundary polygon of a point cloud on the basis of the theory of convex hulls. However, point clouds representing roadway geometries do not fullfill the requirement of convexity. Therefore, a modified algorithm was developed based on the well-known graham scan algorithm. One drawback

of the algorithm is that it is limited to concave boundary angles larger than 120°. Consequently, boundaries of pronounced concave model domains are not detected. Instead, they have to be determined by the help of CAD tools and exported to the model. The interpolation of the point data to the simulation grid was implemented with the inverse distance weighting algorithm. It enables the model to reconstruct real pavement topographies recorded with lidar measurements or pavement topographies of complex road sections designed with CAD tools. The main advantage of inverse distance weighting is its computational speed. However, it presumes densely distributed input data. Lidar measurement data and point clouds exported from CAD tools meet this requirement. The import of point data reconstructed from elevation contour lines is not yet possible.

- Flow resistance is modelled with the Darcy-Weisbach equation. To model real pavement surfaces a model for the resistance coefficient had to be developed which considers the pavements mean texture depth as variable parameter. The calibration of the model was done with experimental data originating from [95]. Five surface covers were tested in the experiments. One advantage of the Darcy-Weisbach equation is that the resistance coefficient can be determined on a profound theoretical basis assuming logarithmic velocity profiles, which develop in fully turbulent flow. Analysis of the experiments showed, however, that a fully turbulent flow could not be assumed and an estimation of the resistance coefficient assuming a logarithmic velocity profile was rejected. Consequently, a potential equation was fitted directly to the experimental data. Parameters which were investigated according to their influence on flow resistance were inundation ratio, bottom slope and the texture related dimensionless Froude Number, which was derived from a dimensional analysis. Both, inundation ratio and texture related Froude Number depend on mean texture depth. It could be shown that an equation including the texture related Froude Number and bottom slope yields the best coefficients of determination for all tested surface covers. The equation was fitted with the entire data set containing all surface covers. Therefore, it is a general equation, which can also be approximately applied to surface covers which were not part of the experiments once their mean texture depth is known.

- Modelling of drainage facilities (inlets) is based on the theory of critical flow assuming that the flow into an inlet can be interpreted as a free overfall.

Finally, the Pavement Surface Runoff Model was applied to various real word flow problems: a road section with drainage facilities, an existing road section with irregular topography and an intersection with a complex boundary. The examples demonstrated the wide range of applications of the model and demarcated it from existing models. The model enables an easy simulation of water depths on irregular

topographies. Further, it can deal with varying surface covers. By the routines developed in this work, an import and processing of point clouds even with complex boundaries is achieved. At last, the model is also able to represent drainage facilities in the form of inlets or gutters. Another focus was on the comparison of the quasi one dimensional, empirical model developed in [95] and the Pavement Surface Runoff Model (PSRM). The comparison was possible because both models are based on the same experimental data base. This offered the chance to discuss similarities and differences of the model concepts. Based on the water depth distribution in a basic superelevation transition it could be shown that in general, both models yield similar results. However, especially in the presence of small bottom slopes, the Pavement Surface Runoff Model yields better results because it considers the full momentum equation. Here, momentum and horizontal pressure gradient are considered as additional driving forces besides bottom slope.

To the authors knowledge, the Pavement Surface Runoff Model is the first model which describes pavement surface runoff on the basis of the depth-averaged Shallow Water Equations including momentum and horizontal pressure gradient. In the literature, the use of the Shallow Water Equations was often rejected due to their high computational intensity and the occurrence of numerical instabilities induced by the small water depths. Further on, effects described by the full momentum equation were considered nonrelevant. However, computational power has been steadily increasing and the development of new and the refinement of existing numerical methods is still subject of intensive research. This work shows that the use of the Shallow Water Equations enable a stable and flexible simulation of Pavement Surface Runoff and that for sections with small bottom slopes the effects described by the full momentum equation have a significant influence on the results.

7.2. Topics of Future Research

Model development usually includes various assumptions and simplifications. Depending on the applications that have to be addressed these simplifications or assumptions can be reasonable or not sufficient. Thus, increasing the complexity of an existing model to widen the range of applications often provides interesting topics for future research activities. In the case of the Pavement Surface Runoff Model developed in this work possible future steps for model extension and refinement are listed in the following:

Topography Reconstruction The inverse distance weighting interpolation algorithm used in the model is only able to deal with densely distributed input data. Therefore, the reconstruction of point data from elevation contour lines is not yet

possible. To overcome this, an interpolation algorithm based on the delaunay triangulation could be used. It can deal with densely and sparsely distributed point data and it is not directional. The use of a delaunay triangulation also offers possibilities to improve the boundary tracing algorithm. By the use of alpha-shape methods, which are based on the delaunay triangulation, the reconstruction of concave boundaries could overcome the limiting boundary angle of 120°.

Modelling of Drainage Facilities So far, drainage facilities are modelled as free overfalls on the basis of the one dimensional critical flow theory. Flow into an inlet can be varied by a parameter introduced as drainage efficiency. Drainage efficiency varies with the inflow conditions and the type of the inlet. Currently, it is set to 100 % because there are no detailed data available. Experiments investigating different inlets with regard to their effect on drainage efficiency could yield a more detailed model.

Flow Resistance Model Shortcomings of the empirical flow resistance model are due to the scarcity of the experimental data available for its calibration. Additional, useful data should include velocity measurements as well as inflow and outflow measurements to check the assumption of the uniform flow conditions. Further on, the surface texture could be analysed by digital techniques to derive more accurate texture parameters. Therefore, the performance of a new set of experiments is suggested. In the long run, flow resistance could also be investigated numerically by resolving the processes at the surface on the micro scale. This would enable to include turbulence explicitly into the flow resistance model.

Porous Asphalt Surface Covers The simulation of the effect of porous asphalt surfaces on pavement surface runoff would constitute a valuable extension of the model. There is currently lots of research on porous asphalt surface covers. Due to their noise absorbing and draining properties, they gain in importance. Infiltration into the porous surface cover could be implemented in two ways. First, it could be realised as a volumetric sink in the continuity equation and second, it could be modelled by resolving the vertical flow processes. For the latter, a non-hydrostatic model should be applied, which also considers vertical velocity components.

Non-Hydrostatic Model Vertical velocity components are neglected in the depth-averaged Shallow Water Equations since a hydrostatic pressure distribution is assumed. To widen the range of applications, a non-hydrostatic model could be used. Then, the surface runoff model could also be coupled with a model describing infiltration processes into the porous pavement structure.

Bibliography

[1] Aberle, J.: *Untersuchung der Rauheitsstruktur zur Bestimmung des Fließwiderstandes in Gebirgsbächen unter Klarwasserabfluss*. Dissertation, Universität Karlsruhe, 2000.

[2] Abrahams, A.D. and Parsons, A.J.: *Hydraulics of interrill overland flow on stone-covered desert surfaces*. CATENA, 23(1-2):111–140, 1994.

[3] Akan, A.O.: *Open Channel Hydraulics*. Civil & Environmental. Butterworth-Heinemann, 2006.

[4] Alcrudo, F. and Garcia-Navarro, P.: *A high-resolution godunov-type scheme in finite volumes for the 2d shallow-water equations*. International Journal for Numerical Methods in Fluids, 16(6):489–505, 1993.

[5] American Meteorological Society: *Glossary of Meteorology*. http://amsglossary.allenpress.com/glossary.

[6] Aureli, F., Maranzoni, A., Mignosa, P., and Ziveri, C.: *A weighted surface-depth gradient method for the numerical integration of the 2d shallow water equations with topography*. Advances in Water Resources, 31(7):962–974, 2008.

[7] Banerjee, I. and Ierapetritou, M.G.: *Feasibility evaluation of nonconvex systems using shape reconstruction techniques*. Industrial & Engineering Chemistry Research, 44(10):3638–3647, 2005.

[8] Barros, A.P. and Colello, J.D.: *Surface roughness for shallow overland flow on crushed stone surfaces*. Journal of Hydraulic Engineering, 127(1):38–52, 2001.

[9] Bastian, P.: *Numerische Lösung partieller Differentialgleichungen*. Vorlesungsumdruck. Institut für Parallele Verteilte Systeme, Universität Stuttgart, 2008.

[10] Beffa, C.J. and Connell, R.J.: *Two-dimensional flood plain flow*. Journal of Hydrologic Engineering, 6(5):397–405, 2001.

[11] Bermudez, A. and Vazquez, M.E.: *Upwind methods for hyperbolic conservation laws with source terms*. Computers & Fluids, 23(8):1049–1071, 1994.

[12] Bradford, S.F. and Sanders, B.F.: *Finite-volume model for shallow-water flooding of arbitrary topography*. Journal of Hydraulic Engineering, 128(3):289–298, 2002.

[13] Brändli, M.: *Modelle und Algorithmen für die Extraktion geomorphologischer und hydrologischer Objekte aus digitalen Geländemodellen*. Dissertation, Geographisches Institut, Universität Zürich, 1998.

[14] Brown, G.O.: *The history of the darcy-weisbach equation for pipe flow resistance*. Environmental and Water Resources History, 38(7):34–43, 2002.

[15] Brufau, P., García-Navarro, P., and Vázquez-Cendón, M.E.: *Zero mass error using unsteady wetting-drying conditions in shallow flows over dry irregular topography*. International Journal for Numerical Methods in Fluids, 45(10):1047–1082, 2004.

[16] Brufau, P., Vázquez-Cendón, M.E., and García-Navarro, P.: *A numerical model for the flooding and drying of irregular domains*. International Journal for Numerical Methods in Fluids, 39(3):247–275, 2002.

[17] Bullinger, A.: *Vergleich von Interpolationsverfahren und digitalen Geländemodellen für Wattgebiete: GIS gestütze Untersuchungen am Beispiel der morphologischen Modellierung von Tide-Becken in Schleswig-Holstein*. Dissertation, Christian-Albrechts-Universität, Kiel, 2000.

[18] Burguete, J., García-Navarro, P., and Murillo, J.: *Friction term discretization and limitation to preserve stability and conservation in the 1d shallow-water model: Application to unsteady irrigation and river flow*. International Journal for Numerical Methods in Fluids, 58(4):403–425, 2008.

[19] Burrough, P.A. and McDonnell, R.A.: *Principles of geographical information systems*. Oxford University Press, Oxford, 1st ed., 1998.

[20] Caleffi, V., Valiani, A., and Zanni, A.: *Finite volume method for simulating extreme flood events in natural channels*. Journal of Hydraulic Research, 41(2):167–177, 2003.

[21] Castro, M.J., Gallardo, J.E.M., and Pares, C.: *High order finite volume schemes based on reconstruction of states for solving hyperbolic systems with nonconservative products: Applications to shallow-water systems*. Mathematics of Computation, 75(255):1103–1134, 2006.

[22] Castro-Orgaz, C. and Chanson, H.: *Bernoulli theorem, minimum specific energy and water wave celerity in open-channel flow*. Journal of Irrigation and Drainage Engineering, 135(6), 2009.

[23] Castro-Orgaz, C. and Hager, W.H.: *Critical flow: A historical perspective*. Journal of Hydraulic Engineering, 136(1):3–11, 2010.

[24] Chanson, H.: *Minimum specific energy and critical flow conditions in open channels*. Journal of Irrigation and Drainage Engineering, 132(5):498–502, 2006.

[25] Charbeneau, R.J., Jeong, J., and Barrett, M.E.: *Highway drainage at superelevation transitions*. Center for Transportation Research, University of Texas, Austin, (4875-1), 2008.

[26] Chaudhry, M.H.: *Open channel flow*. Prentice Hall, Englewood Cliffs, NJ, 1993.

[27] Chow, V.T.: *Open-channel hydraulics: International student edition*. McGraw-Hill Civil Engineering Series. McGraw-Hill, Auckland, 21st print. ed., 1985.

[28] Cormen, T.H.: *Introduction to algorithms*. MIT Press, Cambridge, Massachusetts, 3rd ed., 2009.

[29] Dafermos, C.M.: *Hyperbolic conservation laws in continuum physics*, vol. 325 of *Grundlehren der mathematischen Wissenschaften*. Springer, Berlin, 2nd ed., 2005.

[30] de Berg, M., Cheong, O., van Kreveld, M., and Overmars, M.: *Computational geometry: Algorithms and applications*. Springer, Berlin, 3rd ed., 2008.

[31] Deutscher Wetterdienst (DWD): *KOSTRA-DWD-2000: Starkniederschlagshöhen für Deutschland (1951-2000) - Grundlagenbericht*, 2005.

[32] Deutsches Zentrum für Luft- und Raumfahrt e.V., Zentrales Archiv: *Strömungssichtbarmachung am Göttinger Flügelprofil*.

[33] DIN 13473-1: *Charakterisierung der Textur von Fahrbahnbelägen unter Verwendung von Oberflächenprofilen -Teil 1: Bestimmung der mittleren Profiltiefe*. Deutsches Institut für Normung, 2004.

[34] Dittrich, A.: *Wechselwirkung Morphologie/Strömung naturnaher Fließgewaesser*. Dissertation, Karlsruhe, 1998.

[35] Edelsbrunner, H. and Muecke, E.P.: *Three-dimensional alpha shapes*. In *Proceedings of the 1992 Workshop on Volume visualization*, pp. 75–82, Boston, Massachusetts, United States, 1992. ACM.

[36] Einfeldt, B.: *On godunov-type methods for gas dynamics*. SIAM Journal on Numerical Analysis, 25(2):294–318, 1988.

[37] Esteves, M., Faucher, X., Galle, S., and Vauclin, M.: *Overland flow and infiltration modelling for small plots during unsteady rain: numerical results versus observed values*. Journal of Hydrology, 228(3-4):265–282, 2000.

[38] Fenton, J.D.: *Calculating resistance to flow in open-channels*. Alternative Hydraulics Paper, (2), 2010.

[39] FGSV (Hrsg.): *Richtlinien für die Anlage von Straßen: Teil: Entwässerung (RAS-Ew)*. FGSV-Verlag, 1987.

[40] FGSV (Hrsg.): *Richtlinien für die Anlage von Straßen: Teil: Entwässerung (RAS-Ew)*. Nr. 539. FGSV-Verlag, 2005.

[41] FGSV (Hrsg.): *Richtlinien für die Anlage von Autobahnen (RAA)*. Nr. 202. FGSV-Verlag, 2008.

[42] FGSV (Hrsg.): *Merkblatt für die Herstellung von Oberflächentexturen auf Verkehrsflächen aus Beton*. Nr. 829. FGSV, 2009.

[43] Flemisch, B., Darcis, M., Erbertseder, K., Faigle, B., Lauser, A., Mosthaf, K., Müthing, S., Nuske, P., Tatomir, A., Wolff, M., and Helmig, R.: *Dumux: Dune for multi-{phase, component, scale, physics, ...} flow and transport in porous media*. Advances in Water Resources, 34(9):1102–1112, 2011.

[44] Franke, R. and Nielson, G.: *Smooth interpolation of large sets of scattered data*. Journal of Numerical Methods in Engineering, 15, 1980.

[45] Gallardo, J.M., Pares, C., and Castro, M.: *On a well-balanced high-order finite volume scheme for shallow water equations with topography and dry areas*. Journal of Computational Physics, 227(1):574–601, 2007.

[46] Gallaway, B.M., Rose, J.G., and Schiller, J.R.: *The relative effects of several factors affecting rainwater depths on pavement surfaces*. Highway Research Record No. 396. Highway Research Board (HRB), Washington D. C., USA, 1972.

[47] Godlewski, E. and Raviart, P.A.: *Numerical approximation of hyperbolic systems of conservation laws*. Springer, New York, 1996.

[48] Gottardi, G. and Venutelli, M.: *A control-volume finite-element model for two-dimensional overland flow*. Advances in Water Resources, 16(5):277–284, 1993.

[49] Graf, W.H.: *Fluvial hydraulics : flow and transport processes in channels of simple geometry*. Wiley, Chichester, 1998.

[50] Graham, R.L.: *An efficient algorithm for determining the convex hull of a finite planar set*. Information Processing Letters, 1(4):132–133, 1972.

[51] Guinot, V. and Soares-Frazão, S.: *Flux and source term discretization in two-dimensional shallow water models with porosity on unstructured grids*. International Journal for Numerical Methods in Fluids, 50(3):309–345, 2006.

[52] Hanson, D. and Prowell, B.: *Evaluation of Circular Texture Meter for Measuring Surface Texture of Pavements*. National Center for Asphalt Technology, Auburn, Alabama, 2004.

[53] Harten, A., Lax, P.D., and Leer, B. van: *On upstream differencing and godunov-type schemes for hyperbolic conservation laws*. SIAM Rev., 25(1):35–61, 1983.

[54] He, Z., Wu, W., and Wang, S.S.Y.: *Coupled finite-volume model for 2d surface and 3d subsurface flows*. Journal of Hydrologic Engineering, 13(9):835–845, 2008.

[55] Helmig, R.: *Grundlagen der Hydromechanik*. Shaker, Aachen, 2005.

[56] Herrmann, S. R.: *Simulationsmodell zum Wasserabfluss- und Aquaplaning-Verhalten auf Fahrbahnoberflaechen*. Dissertation, Universität Stuttgart, 2008.

[57] Hilden, M.: *Extension of Shallow Water Equations*. PhD thesis, Universität Kaiserslautern, 2003.

[58] Hirsch, C.: *Numerical computation of internal and external flows: Fundamentals of computational fluid dynamics*. Elsevier,Butterworth-Heinemann, Amsterdam, 2nd ed., 2007.

[59] Höcker, A.: *Die Oberflächenentwässerung von Fahrbahnen und ihre Bedeutung für den Strassenentwurf*. Nr. 118 in *Forschung Strassenbau und Strassenverkehrstechnik*. Wirtschaftsverlag NW, Verlag für Neue Wissenschaft, Bonn, 1971.

[60] Jankowski, J.A.: *A non-hydrostatic model for free surface flows*. PhD thesis, Universität Hannover, 1999.

[61] Jeong, J.: *A Hydrodynamic Diffusion Wave Model for Stormwater Runoff on Highway Surfaces at Superelevation Transitions*. PhD thesis, University of Texas, Austin, 2008.

[62] Jirka, G. und Lang, C.: *Einführung in die Gerinnehydraulik*. Universitätsverlag Karlsruhe, 2009.

[63] Julien, P.: *River Mechanics*. Cambridge University Press, Cambridge, 2005.

[64] Kalender, U.: *Abfluss des Regenwassers von ideal-ebenen Fahrbahnoberflächen*. Dissertation, Technische Universität Berlin, 1974.

[65] Kim, D.H., Cho, Y.S., and Kim, H.J.: *Well-balanced scheme between flux and source terms for computation of shallow-water equations over irregular bathymetry*. Journal of Engineering Mechanics, 134(4):277–290, 2008.

[66] Kirby, J.T., Rocky Durrans, S., Pitt, R., and Johnson, P.D.: *Hydraulic resistance in grass swales designed for small flow conveyance*. Journal of Hydraulic Engineering, 131(1):65–68, 2005.

[67] Klein, R.: *Algorithmische Geometrie: Grundlagen, Methoden, Anwendungen*. Springer, Berlin, 2. Aufl., 2005.

[68] Klein, R., Lehnert, D. und Holderbaum, A.: *Modellversuche zum Abfluss von Niederschlagswasser auf Verwindungsstrecken*. Nr. 250 in *Forschung Straßenbau und Straßenverkehrstechnik*. Wirtschaftsverl. NW, Verlag fuer Neue Wissenschaft, Bonn-Bad Godesberg, 1978.

[69] Koppe, P. und Stozek, A.: *Kommunales Abwasser: seine Inhaltsstoffe nach Herkunft, Zusammensetzung und Reaktionen im Reinigungsprozeß einschließlich Klärschlämme*. Vulkan-Verl, Essen, 4. Aufl., 1999.

[70] Kuiry, S.N., Pramanik, K., and Sen, D.: *Finite volume model for shallow water equations with improved treatment of source terms*. Journal of Hydraulic Engineering, 134(2):231–242, 2008.

[71] Landesamt für Geoinformation und Landentwicklung, Baden-Württemberg.

[72] Lawrence, D.S.L.: *Macroscale surface roughness and frictional resistance in overland flow*. Earth Surface Processes and Landforms, 22(4):365–382, 1997.

[73] LeVeque, R.J.: *Numerical Methods for Conservation Laws*. Lectures in mathematics. Birkhäuser, Basel, 1990.

[74] LeVeque, R.J.: *Finite volume methods for hyperbolic problems*, vol. 31 of *Cambridge texts in applied mathematics*. Cambridge Univ. Press, Cambridge, 2002.

[75] Li, J. and Heap, A.D.: *A review of spatial interpolation methods for environmental scientists*, vol. 23 of *Geoscience Australia*. Geoscience Australia, Canberra, 2008.

[76] Li, Z.: *Digital terrain modeling : principles and methodology*. CRC, Boca Raton, 2005.

[77] Liang, Q. and Borthwick, A.G.L.: *Adaptive quadtree simulation of shallow flows with wet-dry fronts over complex topography*. Computers & Fluids, 38(2):221–234, 2009.

[78] Liang, Q. and Marche, F.: *Numerical resolution of well-balanced shallow water equations with complex source terms*. Advances in Water Resources, 32(6):873–884, 2009.

[79] Lucas, J.: *Messung der geometrischn Rauheit und Wasserabfluss von der Fahrbahn*. Nr. 2 in *Berichte des Instituts für Straßen- und Verkehrswesen der Technischen Universität Berlin*. Wilhelm Ernst & Sohn, 1968.

[80] Mack, A., Müller, K. und Siekmann, T.: *Klimanpassungsstrategien für Entwässerungssysteme*. Forschungsinstitut für Wasser- und Abfallwirtschaft, RWTH Aachen, 2011.

[81] Malcherek, A.: *Hydromechanik der Oberflächengewaesser*. Bundesanstalt für Wasserbau, Außenstelle Küste, Hamburg, 2003.

[82] Melkemi, M. and Djebali, M.: *Computing the shape of a planar points set*. Pattern Recognition, 33(9):1423–1436, 2000.

[83] Miller, H.J.: *ToblerÂ´s first law and spatial analysis*. Annals of the Association of american Geographers, pp. 284–289, 2004.

[84] Moody, L.F.: *Friction factors for pipe flow*. Transactions of the American Society of Mechanical Engineers, (66):671–684, 1944.

[85] Munz, C. D. und Westermann, T.: *Numerische Behandlung gewöhnlicher und partieller Differenzialgleichungen: Ein interaktives Lehrbuch für Ingenieure*. Springer, Berlin, 2006.

[86] Murillo, J., García-Navarro, P., and Burguete, J.: *Time step restrictions for well-balanced shallow water solutions in non-zero velocity steady states*. International Journal for Numerical Methods in Fluids, 60(12):1351–1377, 2009.

[87] Musleh, F.A. and Cruise, J.F.: *Functional relationships of resistance in wide flood plains with rigid unsubmerged vegetation*. Journal of Hydraulic Engineering, 132(2):163–171, 2006.

[88] Naef, D. R.: *Numerische Simulation von Stosswellen in Freispiegelströmungen*, Bd. 148 d. Reihe *Mitteilungen der Versuchsanstalt für Wasserbau, Hydrologie und Glaziologie an der Eidgenoessischen Technischen Hochschule Zuerich*. VAW, Zürich, 1997.

[89] Nikuradse, J.: *Strömungsgesetze in rauhen Rohren*. Nr. 361 in *Forschungsheft*. VDI-Verl, Berlin, 1933.

[90] Petraczek, O.: *Experimentelle Ermittlung der Wasserfilmdicken auf Fahrbahnen unter natürlichen Bedingungen*. Nr. 195 in *Forschung Straßenbau und Straßenverkehrstechnik*. Bundesminister für Verkehr, Abt. Strassenbau, Bonn- Bad Godesberg, 1975.

[91] Pieper, K.: *Regenabfluss von Straßenflächen*. Dissertation, Technische Hochschule Dresden, Dresden, 1938.

[92] Pnueli, D. and Gutfinger, C.: *Fluid mechanics*. Cambridge University Press, Cambridge, 1997.

[93] Preparata, F.P. and Shamos, M.I.: *Computational geometry : an introduction*. Springer, New York, 5th ed., 1993.

[94] Reinhold, F.: *Regenspenden in Deutschland : (Grundwerte für die Entwässerungstechnik, GE 1940)*, vol. 56 of *Archiv für Wasserwirtschaft des Reichsverbandes der Deutschen Wasserwirtschaft e.V.* Reichsverb. der Dt. Wasserwirtschaft, Berlin, 1940.

[95] Ressel, W. und Herrmann, S. R.: *Aquaplaning und Verkehrssicherheit in Verwindungsbereichen dreistreifiger Richtungsfahrbahnen : Berechnung der Wasserfilmdicke*. Nr. 997 in *Forschung Straßenbau und Straßenverkehrstechnik*. Wirtschaftsverl. NW, Verlag fuer Neue Wissenschaft, Bremerhaven, 2008.

[96] Roe, P.L.: *Approximate riemann solvers, parameter vectors, and difference schemes*. Journal of Computational Physics, 43(2):357–372, 1981.

[97] Ross, N.F. and Russam, K.: *The depth of rain water on road surfaces*. RRL Report LR 236, 1968.

[98] Sabrowski, M.: *Eine Analyse zum Strömungswiderstand natürlicher Fließgewässer mit ausgeprägter Sohlstrukturierung*. Dissertation, Bauhaus-Universität, Weimar, 2008.

[99] Sampath, A. and Shan, J.: *Building boundary tracing and regularization from airborne lidar point clouds*. Photogrammetric Engineering & Remote Sensing, 73(7):805–812, 2007.

[100] Schlichting, H.: *Grenzschicht-Theorie*. Springer-Verlag, Berlin, Heidelberg, 10. Aufl., 2006.

[101] Shepard, D.: *A two-dimensional interpolation function for irregularly-spaced data*. In *Proceedings of the 1968 23rd ACM national conference*, ACM '68, pp. 517–524, New York, NY, USA, 1968. ACM.

[102] Smith, M.W., Cox, N.J., and Bracken, L.J.: *Applying flow resistance equations to overland flows*. Progress in Physical Geography, 31(4):363–387, 2007.

[103] Tan, W.Y.: *Shallow water hydrodynamics: Mathematical theory and numerical solution for a two-dimensional system of shallow water equations /*, vol. 55 of *Elsevier oceanography series*. Water & Power Press [u.a.], Beijing, China, 1992.

[104] The DUNE website.: *Url http://www.dune-project.org/*.

[105] Toro, E.F.: *Riemann solvers and numerical methods for fluid dynamics: A practical introduction*. Springer, Berlin, 2nd ed., 1999.

[106] Toro, E.F. (ed.): *Godunov methods: Theory and applications*. Kluwer Academic/Plenum Publishers, New York, 2001.

[107] Toro, E.F., Spruce, M., and Speares, W.: *Restoration of the contact surface in the hll-riemann solver*. Shock Waves, 4(1):25–34, 1994.

[108] Valiani, A. and Begnudelli, L.: *Divergence form for bed slope source term in shallow water equations*. Journal of Hydraulic Engineering, 132(7):652–665, 2006.

[109] Valiani, A., Caleffi, V., and Zanni, A.: *Case study: Malpasset dam-break simulation using a two-dimensional finite volume method*. Journal of Hydraulic Engineering, 128(5):460–472, 2002.

[110] Vreugdenhil, C.B.: *Numerical methods for shallow-water flow*. Kluwer Academic Publishers, Dordrecht, Boston, London, 2nd ed., 1998.

[111] White, F.M.: *Fluid Mechanics*. McGraw-Hill, New York, 5th ed., 2003.

[112] Yen, B.C.: *Open channel flow resistance*. Journal of Hydraulic Engineering, 128(1):20–39, 2002.

[113] Yoon, T.H. and Kang, S.K.: *Finite volume model for two-dimensional shallow water flows on unstructured grids*. Journal of Hydraulic Engineering, 130(7):678–688, 2004.

[114] Zhao, D.H., Shen, H.W., Tabios, G.Q., Lai, J.S., and Tan. W. Y.: *Finite-volume two-dimensional unsteady-flow model for river basins*. Journal of Hydraulic Engineering, 120(7):863–883, 1994.

[115] Zhou, J.G., Causon, D.M., Mingham, C.G., and Ingram, D.M.: *The surface gradient method for the treatment of source terms in the shallow-water equations*. Journal of Computational Physics, 168(1):1–25, 2001.

[116] Zior, F.: *Regenwasserabfluss auf Fahrbahnoberflächen : experimentelle u. theoretische Untersuchungen*. Nr. 38 in *Technische Berichte über Ingenieurhydrologie und Hydraulik*. IHH, Institut für Wasserbau, Technische Hochschule Darmstadt, Darmstadt, 1987.

A. Appendix

A.1. Jacobian Matrix of the Two Parameter Resistance Model

$$
\begin{aligned}
\frac{\partial S_{f1}}{\partial h} &= \frac{\partial S_{f1}}{\partial q} = \frac{\partial S_{f1}}{\partial r} = 0 \\
\frac{\partial S_{f2}}{\partial h} &= (-c-2)\ \frac{1}{h^{c+3}}\ (q^2+r^2)^{0.5c+0.5}\ q \\
\frac{\partial S_{f2}}{\partial q} &= \frac{1}{h^{c+2}}\ [(c+1)\ (q^2+r^2)^{0.5c-0.5}\ q^2 + (q^2+r^2)^{0.5c+0.5}] \\
\frac{\partial S_{f2}}{\partial r} &= \frac{1}{h^{c+2}}\ [(c+1\ )(q^2+r^2)^{0.5c-0.5}\ qr] \\
\frac{\partial S_{f3}}{\partial h} &= (-c-2)\ \frac{1}{h^{c+3}}\ (q^2+r^2)^{0.5c+0.5}\ q \\
\frac{\partial S_{f3}}{\partial q} &= \frac{1}{h^{c+2}}\ [(c+1\ )(q^2+r^2)^{0.5c-0.5}\ qr] \\
\frac{\partial S_{f3}}{\partial r} &= \frac{1}{h^{c+2}}\ [(c+1)\ (q^2+r^2)^{0.5c-0.5}\ r^2 + (q^2+r^2)^{0.5c+0.5}].
\end{aligned}
\tag{A.1}
$$

A.2. Histograms

Histograms for the referenced water depth h_{ref} calculated for a basic superelevation transition with Planus and the PSRM:

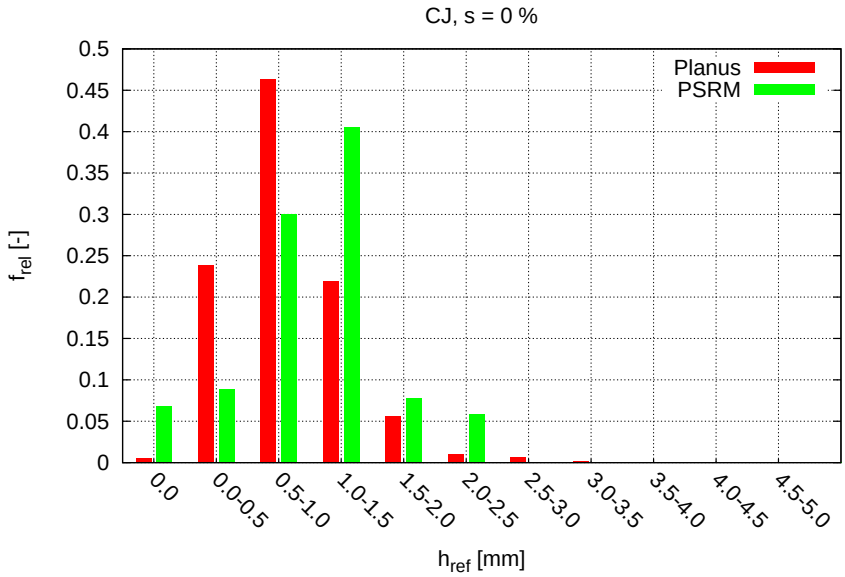

Figure A.1.: Histogram of water depths in the example superelevation transition for CJ and s = 0 %)

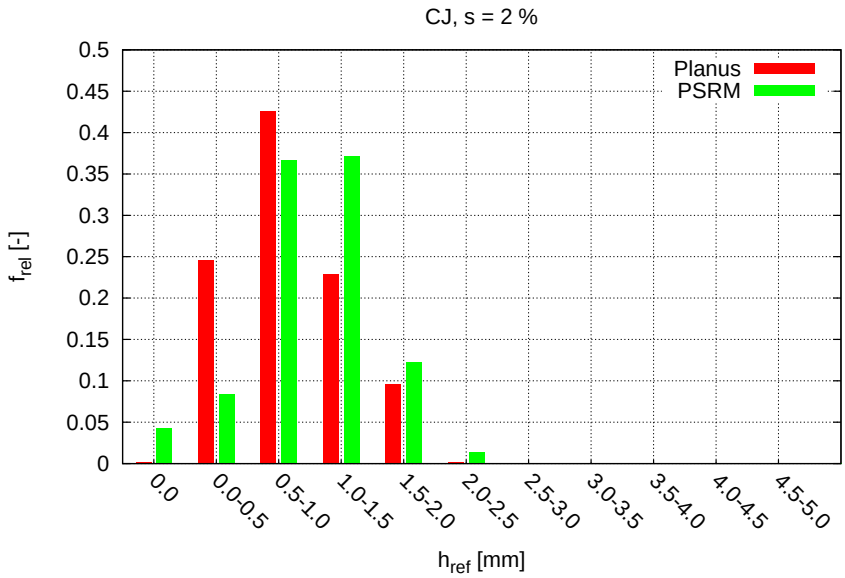

Figure A.2.: Histogram of water depths in the example superelevation transition for CJ and s = 2 %)

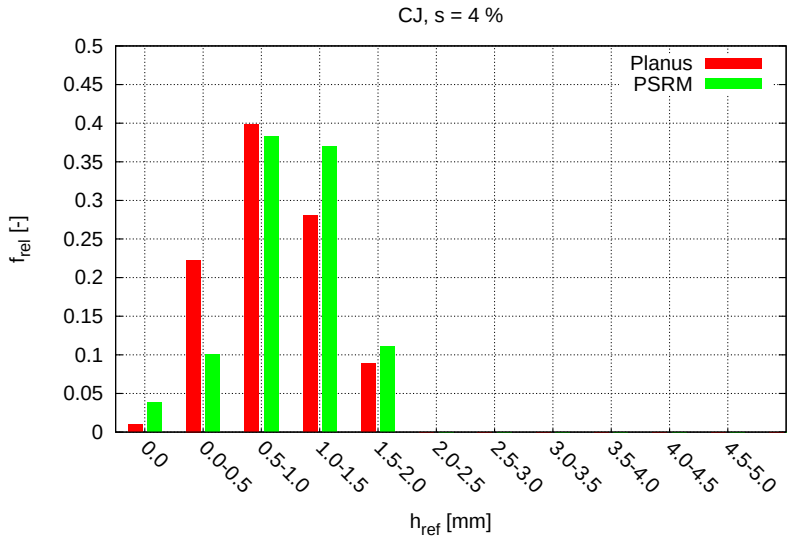

Figure A.3.: Histogram of water depths in the example superelevation transition for CJ and s = 4 %)

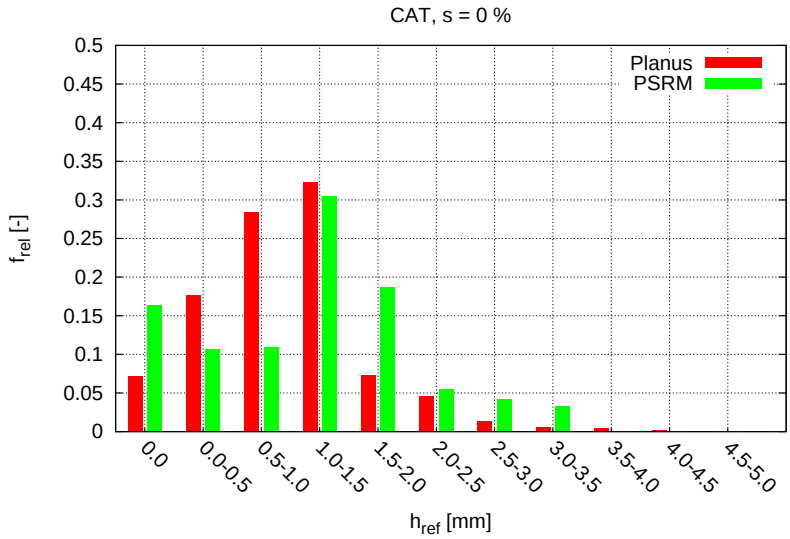

Figure A.4.: Histogram of water depths in the example superelevation transition for CAT and s = 0 %)

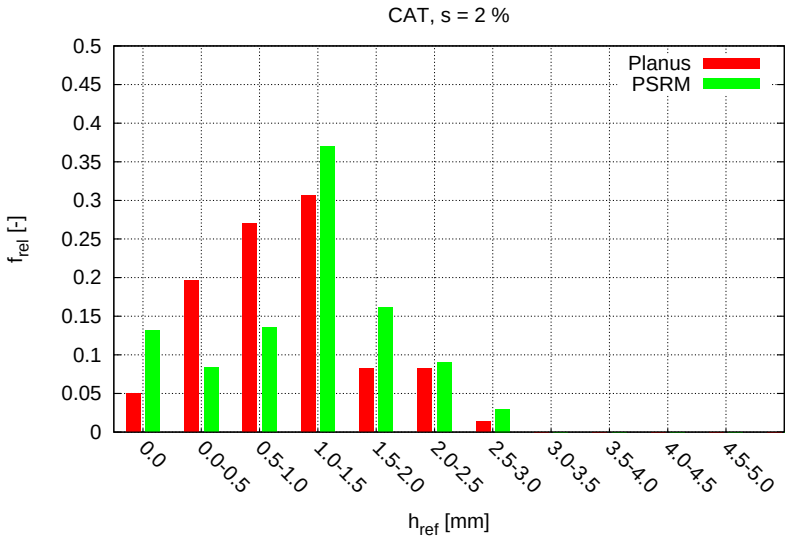

Figure A.5.: Histogram of water depths in the example superelevation transition for CAT and s = 2 %)

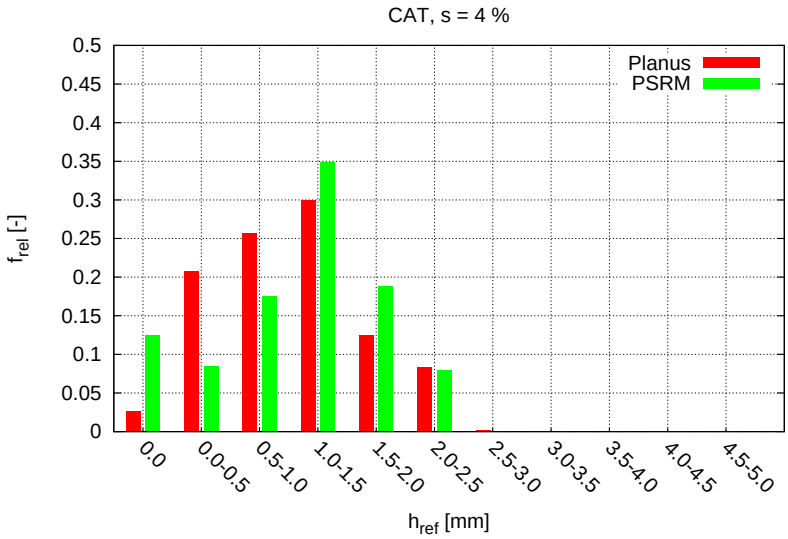

Figure A.6.: Histogram of water depths in the example superelevation transition for CAT and s = 4 %)

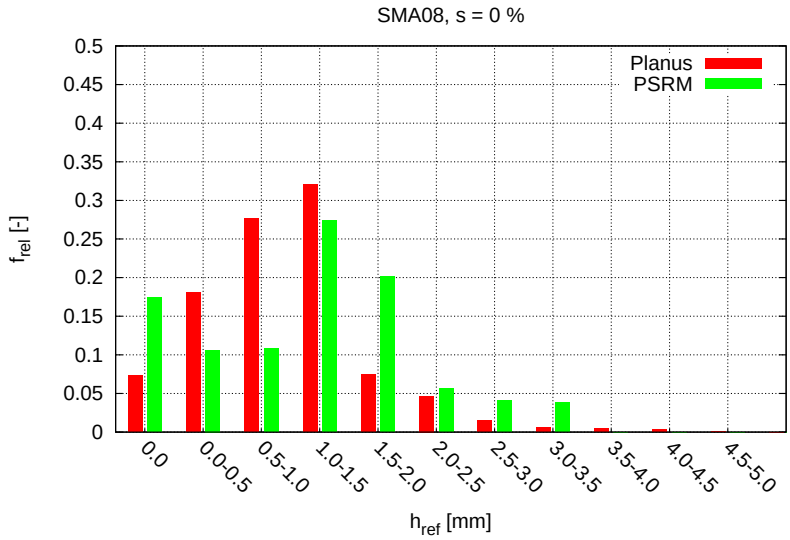

Figure A.7.: Histogram of water depths in the example superelevation transition for SMA08 and s = 0 %)

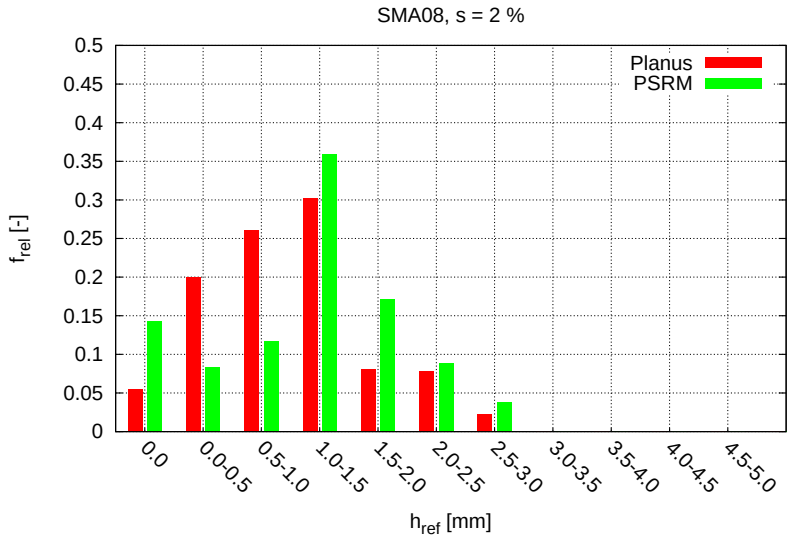

Figure A.8.: Histogram of water depths in the example superelevation transition for SMA08 and s = 2 %)

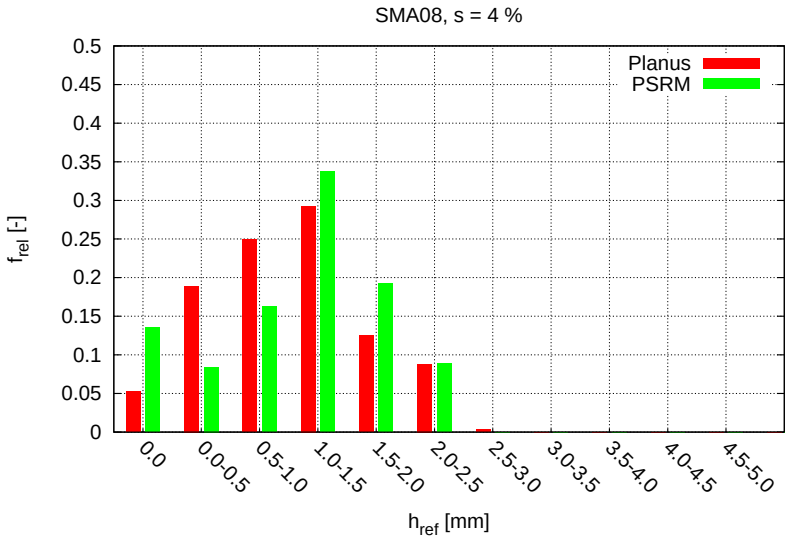

Figure A.9.: Histogram of water depths in the example superelevation transition for SMA08 and s = 4 %)

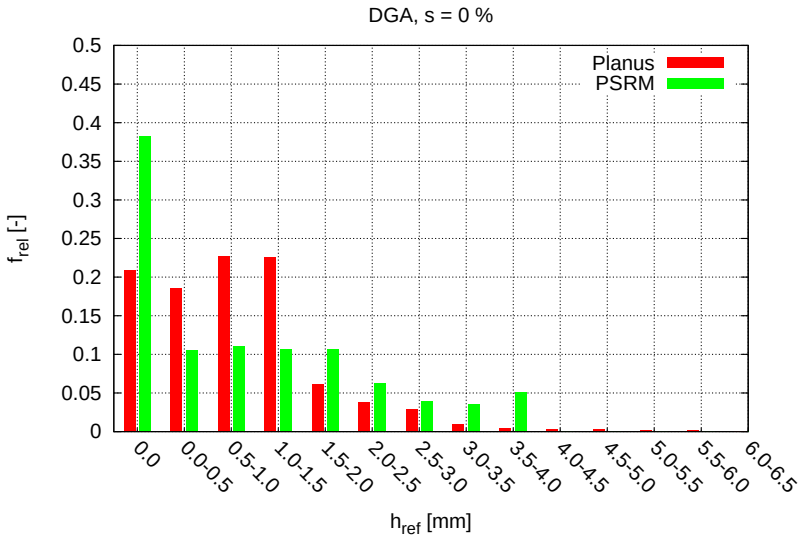

Figure A.10.: Histogram of water depths in the example superelevation transition for DGA and s = 0 %)

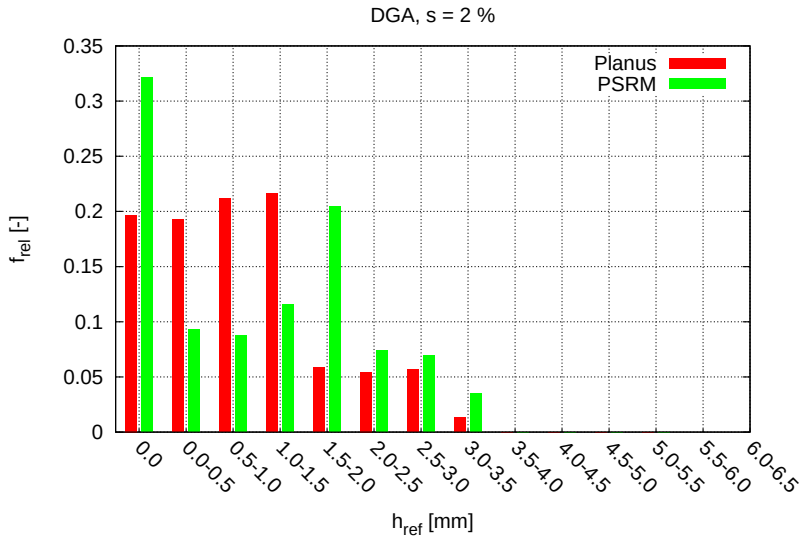

Figure A.11.: Histogram of water depths in the example superelevation transition for DGA and s = 2 %)

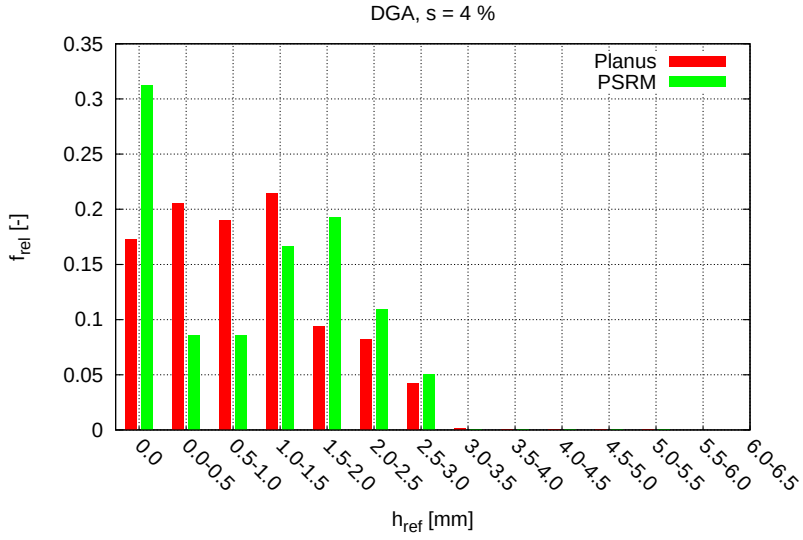

Figure A.12.: Histogram of water depths in the example superelevation transition for DGA and s = 4 %)

Schriftenreihe des Instituts für Straßen- und Verkehrswesen

Heft 1	1. Fachkolloquium Straße und Verkehr - Stuttgart 1986	9/1987
Heft 2	2. Fachkolloquium Straße und Verkehr - Stuttgart 1988	4/1989
Heft 3	Arbeiten aus dem Institut für Straßen-und Verkehrswesen	7/1989
Heft 4	Beiträge zum Ruhenden Verkehr	8/1989
Heft 5	Festkolloquium anlässlich der Vollendung des 60.Lebensjahres von Prof. Dr.-Ing. Gerd Steierwald	5/1990
Heft 6	3. Fachkolloquium Straße und Verkehr - Stuttgart 1990	4/1991
Heft 7	Wolfgang Hertkorn Veränderungen des Kraftstoffverbrauchs und der Abgasbelastungen durch Geschwindigkeitsreduktion in untergeordneten städtischen Straßennetzen	2/1992
Heft 8	City Stuttgart - attraktive Innenstadt im Zentrum einer Agglomeration (Autofreie Innenstadt = Attraktive City?)	3/1992
Heft 9	Arbeiten aus dem Institut für Straßen-und Verkehrswesen	4/1992
Heft 10	Reinhard Unkhoff Der Einfluß des Schwerverkehrs auf Geschwindigkeitsverhalten und Pulkbildung auf Autobahnen	6/1992
Heft 11	Stefanos Bazis Interaktiver Straßenentwurf mit Hilfe der EDV	7/1992
Heft 12	Jiann-Sheng Wu Stochastische Simulation des Überholverhaltens auf zweistreifigen Landstraßen	7/1992

Heft 13	4. Fachkolloquium Straße und Verkehr - Stuttgart 1992	5/1993
Heft 14	Stephan Herkt Abstimmung der Leistungsfähigkeit von Knotenpunkten mit Lichtsignalanlage und knotenpunktfreien Strecken an innerörtlichen Hauptverkehrsstraßen	4/1994
Heft 15	Von den Anfängen bis zur Gegenwart -Straßen- und Verkehrswesen an der Universität Stuttgart	9/1994
Heft 16	Ashraf Hamed Abwicklung des Lieferverkehrs innerörtlichen Hauptstraßen	10/1994
Heft 17	5. Fachkolloquium Straße und Verkehr - Stuttgart 1994	3/1995
Heft 18	Chronik und Retrospektive - Gerd Steierwald und das Institut für Straßen- und Verkehrswesen	10/1995
Heft 19	Heiko Tempel Zusammenhänge zwischen Verkehrsablauf, Kraftstoffverbrauch und Schadstoffemissionen im städtischen Busverkehr	11/1995
Heft 20	Volker Mörgenthaler Strategien zur Verminderung der Emissionen von Ozonvorläufersubstanzen des Nutzfahrzeugverkehrs in Ballungsgebieten	2/1996
Heft 21	Martin Schmid Auswirkungen der Kraftstoffbesteuerung auf die Pkw-Fahrleistungen im Freizeitverkehr	11/1996
Heft 22	Burkhard Flasche Fahrraumbewirtschaftung mit Sonderfahrstreifen für ausgewählte Stadtverkehre	2/1998
Heft 23	Szabolcs Törgyekes Ableitung spezifischer Abgas-Emissionsfaktoren für Kraftfahrzeugkollektive anhand von Konzentrationsmessungen in einem städtischen Straßentunnel	3/1998

Heft 24	Konrad von Kirchbach Zur Entwicklung der Straßen in Württemberg zwischen 1700 bis 1918	3/2000
Heft 25	6. Fachkolloquium Straße und Verkehr - Stuttgart 1999	3/2009
Heft 26	Symposium Stadt und Verkehr – Mobile Konferenz	11/1999
Heft 27	„Institut 21“ Aufbruch in Forschung und Lehre (nicht erschienen)	
Heft 28	Arbeiten aus dem Institut für Straßen-und Verkehrswesen	7/2001
Heft 29	Stefan Denzinger Auswirkungen alternierender Telearbeit auf das Verkehrsverhalten	4/2001
Heft 30	7. Fachkolloquium Straße und Verkehr - Stuttgart 2001	3/2009
Heft 31	Prof. Elisabeth Deakin Changing Importance of Central Cities	8/2002
Heft 32	Walter Vogt, Matthias Lenz, Henrik Schwarz, Wilhelm Glaser, Margrit Glaser, Thomas Kuder Verkehrliche Auswirkungen von Teleshopping und Telecommerce auf die Mobilität privater Haushalte	6/2002
Heft 33	Christoph Hecht Modellierung des Zeitwahlverhaltens im Personenverkehr	2/2005
Heft 34	Henrik Schwarz Vergleich von SchallImmissionsmessungen bei Straßenverkehrslärm mit Standardisierten und Binauralen Geräten	11/2002
Heft 35	Peter Schick Einfluss von Streckenbeeinflussungsanlagen auf die Kapazität von Autobahnabschnitten sowie die Stabilität des Verkehrsflusses	6/2003

Heft 36	Volker Schmid Reaktivierte Nebenbahnen und alternative Buskonzepte Vergleich von ökologischen Wirkungen	7/2003
Heft 37	8. Fachkolloquium Straße und Verkehr - Stuttgart 2003	3/2009
Heft 38	Matthias Lenz Auswirkungen des Ausbaus der verkehrlichen Infrastruktur auf das regionale Fernpendleraufkommen	2/2005
Heft 39	Steffen R. Herrmann Simulationsmodell zum Wasserabfluss- und Aquaplaningverhalten auf Fahrbahnoberflächen	2/2008
Heft 40	Manuel Galster Modellierung von Anbindungen in Verkehrsplanungsmodellen	8/2009
Heft 41	10. Fachkolloquium Straße und Verkehr - Stuttgart 2008	8/2009
Heft 42	Johannes Schlaich Nutzung von Mobilfunkdaten für die Analyse der Routenwahl	6/2010
Heft 43	Florian Bitzer Mikroskopische Modellierung und Simulation des Fußgängerverkehrs	9/2010
Heft 44	Eileen Mandir Potential of Traffic Information to optimize Route and Departure Time Choice	7/2012
Heft 45	Anne Wolff Simulation of Pavement Surface Runoff using the Depth-Averaged Shallow Water Equations	3/2013
Heft 46	Stefan Alber Veränderung des Schallabsorptionsverhaltens von offenporigen Asphalten durch Verschmutzung	3/2013